

**Theory of Injection Locking and Rapid Start-Up of Magnetrons, and Effects of  
Manufacturing Errors in Terahertz Traveling Wave Tubes**

**by**

**Phongphaeth Pengvanich**

A dissertation submitted in partial fulfillment  
of the requirements for the degree of  
Doctor of Philosophy  
(Nuclear Engineering and Radiological Sciences)  
in The University of Michigan  
2007

Doctoral Committee:

Professor Yue Ying Lau, Chair  
Professor Ronald M. Gilgenbach  
Associate Professor Mahta Moghaddam  
John W. Luginsland, NumerEx

© Phongphaeth Pengvanich

---

All rights reserved  
2007

For Mom and Dad

## ACKNOWLEDGEMENTS

I would like to express my deep gratitude to my advisor, Professor Y. Y. Lau, who has never ceased to inspire and motivate me throughout my graduate student career. Professor Lau not only taught me Plasma Physics, but also showed me how to be a good theoretician and how to be passionate about my work. I can never thank him enough for his continuous guidance and support in the past five years, and I have always considered myself very fortunate to have him as my mentor.

Professor Ronald Gilgenbach was the first person who captured my interest in Plasma Physics when I was still an undergraduate. Since then, he has given me many advices and ideas for my work, and has provided me with an opportunity to teach a Plasma laboratory class. I would like to thank him for his tremendous help.

I wish to thank Professor Mahta Moghaddam for serving on my dissertation committee, and for her thoughtful comments.

I thank Dr. John Luginsland of NumerEx for his continuous advices and updates on the injection locking and the manufacturing error projects. Many improvements to my work have been contributed by his suggestions. It has been a pleasure to have him on my dissertation committee.

It has been my greatest pleasure getting to work and to coauthor with Dr. Bogdan Neculaes. He has been a friend and a mentor since I started graduate school. Working with him on the parametric instability and the injection locking projects was very

enjoyable, and I owe him a big “thank you” for allowing me to use his experimental data in this thesis. I also would like to thank him for the time he took to answer my questions and explain to me a great deal about his experiments.

I thank Dr. David Chernin from SAIC for providing research ideas and agreeing to work with me on the manufacturing error project. It is the first time that I get to work with people outside the university, and it has been a great experience.

Dr. Mike Lopez, Dr. William White, and Brad Hoff have been a great help when I have questions about relativistic magnetron. Getting to be in MELBA screen room while they ran experiments was very exciting and a great experience. I thank them for providing me such opportunities.

Dr. Trevor Strickler, Dr. Richard Kowalczyk, and Dr. Michael Jones were other fellow graduate students whom I went to for numerical code and simulation help. I thank them for the time they took to answer my questions and helped me figure out algorithms.

I thank Dr. Yoshiteru Hidaka for his help in the parametric instability project. His finding prompted further search that eventually led to our discovery.

While I did not get a chance to work with Dr. Herman Bosman, Dr. Allen Garner, Wilkin Tang, and Nick Jordan, we often had many good and stimulated discussions on Plasma Physics and other things, and I would like to thank them for that.

To all my previous and current colleagues, most of whom have been mentioned, I owe each of you a big “thank you” not only for the work we have done together, but also for the good talks and friendship. My graduate school experience has been great because of you all.

I would like to give special thanks to Pantip Ampornrat and Niravun Pavenayotin, who are the other Thai students in the department. Their concerns to my well-being and their help are deeply appreciated.

Pam Derry and Peggy Gramer have always been very helpful to me throughout the years. They are the two nicest student advisors whom I have ever met.

Emotional support from my family, both in Thailand and in the States, has always been the largest motivation for my study. I could never have gone through graduate school without them continuously cheering for me. Thank you, mom and dad, for always believe in me and taught me to stand up on my own. Thank you, everyone.

# TABLE OF CONTENTS

<b>DEDICATION .....</b>	<b>ii</b>
<b>ACKNOWLEDGEMENTS .....</b>	<b>iii</b>
<b>LIST OF FIGURES .....</b>	<b>viii</b>
<b>LIST OF APPENDICES .....</b>	<b>xii</b>
<b>ABSTRACT.....</b>	<b>xiii</b>
<b>CHAPTER 1. INTRODUCTION .....</b>	<b>1</b>
1.1 MAGNETRON.....	2
1.2 TRAVELING WAVE TUBE.....	11
1.3 THESIS ORGANIZATION .....	14
<b>CHAPTER 2. PARAMETRIC INSTABILITY IN ELECTRON ORBITS IN A CROSSED-FIELD GAP WITH A PERIODIC MAGNETIC FIELD .....</b>	<b>15</b>
2.1 INTRODUCTION .....	15
2.2 THE MODEL .....	17
2.3 THE RESULTS .....	20
2.4 REMARKS.....	27
<b>CHAPTER 3. MODELING AND COMPARISON WITH EXPERIMENTS OF MAGNETRON INJECTION LOCKING .....</b>	<b>32</b>
3.1 INTRODUCTION.....	32
3.2 PHASE-LOCKING THEORY FOR MAGNETRON.....	33
3.3 NUMERICAL RESULTS OF PHASE LOCKING ANALYSES .....	40
3.4 INJECTION LOCKING EXPERIMENTAL SETUP [NEC05B] .....	42
3.5 EXPERIMENTAL RESULTS [NEC05B] .....	44
3.6 COMPARISON BETWEEN NUMERICAL CALCULATIONS AND EXPERIMENTAL RESULTS .....	48
3.7 LOCKING TIME .....	51
<b>CHAPTER 4. EFFECTS OF FREQUENCY CHIRPING ON MAGNETRON INJECTION LOCKING .....</b>	<b>54</b>
4.1 INTRODUCTION.....	54

4.2 INJECTION LOCKING FORMULATIONS IN THE PRESENCE OF FREQUENCY CHIRP .....	55
4.3 EFFECTS OF SMALL RANDOM FLUCTUATION IN FREQUENCY ON INJECTION LOCKING.....	63
<b>CHAPTER 5. EFFECT OF RANDOM CIRCUIT FABRICATION ERRORS ON SMALL SIGNAL GAIN AND PHASE IN TRAVELING WAVE AMPLIFIERS .....</b>	<b>65</b>
5.1 INTRODUCTION.....	65
5.2 LINEAR THEORY OF A BEAM INTERACTING WITH A SLOW WAVE CIRCUIT WITH RANDOM ERRORS .....	67
5.3 EFFECTS OF RANDOM PERTURBATIONS OF THE PIERCE PARAMETERS ON SMALL SIGNAL GAIN AND PHASE .....	70
5.4 REMARKS.....	83
<b>CHAPTER 6. SUMMARY AND CONCLUSIONS .....</b>	<b>86</b>
6.1 ON THE DISCOVERY OF PARAMETRIC INSTABILITY IN A MAGNETICALLY PRIMED MAGNETRON.....	86
6.2 ON THE INJECTION LOCKING OF MAGNETRONS.....	87
6.3 ON THE EFFECTS OF RANDOM MANUFACTURING ERRORS ON TWT PERFORMANCE .....	89
<b>APPENDICES .....</b>	<b>91</b>
<b>BIBLIOGRAPHY.....</b>	<b>96</b>

## LIST OF FIGURES

<b>Figure 1.1</b>	Conventional and relativistic magnetrons. The left-hand-side is a cut-through of a kW conventional magnetron used in microwave oven [Nec05b]. The right-hand-side is a picture from the University of Michigan's relativistic magnetron [Whi05].....	4
<b>Figure 1.2</b>	Illustration of (a) the cylindrical model [Lau87] and (b) the planar model which are typically used in magnetron study.....	6
<b>Figure 1.3</b>	RF electric field inside the A-K gap for a planar magnetron [Lau87]. .....	9
<b>Figure 1.4</b>	Basic model of helix TWT showing 1) electron gun, 2) RF input, 3) magnets, 4) attenuator, 5) helix coil, 6) RF output, 7) vacuum tube, and 8) collector [Pie04].....	11
<b>Figure 1.5</b>	Field pattern on the helix TWT [Gil94]. .....	13
<b>Figure 2.1</b>	The normalized magnetic field distribution, $B/B_0 = 1 - \alpha p(y)$ , as a function of $y$ , the normalized distance in the $E \times B$ drift direction. ....	18
<b>Figure 2.2</b>	A single electron orbit that is emitted with the initial coordinates $(x, y) = (0, y_0)$ with $y_0 = -1.903\pi$ , $p(y)$ has a periodicity of $\lambda = 90$ units in $y$ . ....	20
<b>Figure 2.3</b>	Maximum excursion as a function of the electron's initial coordinates $(x, y) = (0, y_0)$ , $p(y)$ has a periodicity of $\lambda = 90$ units in $y$ . ....	21
<b>Figure 2.4</b>	A single electron orbit that is emitted with the initial coordinates $(x, y) = (0, y_0)$ with $y_0 = -0.9936\pi$ . In this figure, $p(y)$ has a periodicity of $\lambda = 90.2$ units in $y$ [Nec05c].....	22
<b>Figure 2.5</b>	Electron maximum excursion as a function of $\alpha$ , when $\lambda = 90$ . The electron maximum excursion peaks in certain bands of $\alpha$ .....	23
<b>Figure 2.6</b>	A zoom-in single electron orbit that is emitted with the initial coordinates $(x, y) = (0, y_0)$ with $y_0 = -0.9936\pi$ , $p(y)$ has a periodicity of $\lambda = 90.2$ units in $y$ . ....	24
<b>Figure 2.7</b>	The 5 electron bunches at (a) $t = 4$ (about half cycloidal orbit after emission), (b) $t = 73$ , (c) $t = 454$ (after one re-circulation around the cathode), and (d) $t = 1314$ (after 3 revolutions around the cathode). ....	26

<b>Figure 3.1</b>	The circuit model representing a magnetron that operates at a specific mode. ....	34
<b>Figure 3.2</b>	Magnetron electronic admittance $g$ and electronic susceptance $b$ as a function of $V_{rf}$ . ....	35
<b>Figure 3.3</b>	Spectra of the free-running oscillator and the external driving signals. ....	39
<b>Figure 3.4</b>	Locking signal at $i_1/Q_{ext} = 0.0008$ and $0.0012$ . Locking occurs when $i_1/Q_{ext} = 0.002$ according to the Adler's condition. ....	41
<b>Figure 3.5</b>	Locking signal at $i_1/Q_{ext} = 0.0019$ and $0.0026$ . Locking occurs when $i_1/Q_{ext} = 0.002$ according to the Adler's condition. ....	42
<b>Figure 3.6</b>	The reflection amplifier setup for injection lock experiment [Nec05b]. ....	44
<b>Figure 3.7</b>	Peak frequency dependence on the output power of the free running oscillator (zero drive power). With an external drive power at 16W, the oscillator frequency remains constant (locked) [Nec05b]. ....	45
<b>Figure 3.8</b>	Spectra of the oscillator and the driver in free running mode for the experiments performed to study the mechanism of injection locking (varied $P_{drive}$ ). $P_0 = 825$ W [Nec05b]. ....	46
<b>Figure 3.9</b>	Reflection amplifier microwave spectra when $P_{drive}$ is set to 5 and 15 W. Locking occurs when $P_{drive} > 58$ W according to Adler's Condition. [Nec05b] ....	47
<b>Figure 3.10</b>	Reflection amplifier microwave spectra when $P_{drive}$ is set to 55 and 100 W. Locking occurs when $P_{drive} > 58$ W according to Adler's Condition. [Nec05b] ....	47
<b>Figure 3.11</b>	(a) Amplitude and (b) phase solutions of the output signal in time domain. The frequency difference between the injected signal and the oscillator signal is 0.001 so that Adler's condition is satisfied when $i_1/Q_{ext} \geq 0.002$ . ....	52
<b>Figure 3.12</b>	The amount of time that the phase difference between the injected and the oscillator signal takes to reach 99% of its saturation value after the injected signal is applied, i.e., locking time. ....	53
<b>Figure 4.1</b>	Example of the injected frequency profile. Here, $d\omega_1/dt = 2 \times 10^{-7}$ . The dotted lines show the boundaries of the locking range according to Adler's condition. ....	55
<b>Figure 4.2</b>	Differential phase shift of the output signal. The injected signal is not applied until $t = 2000$ . The dotted lines show the boundaries of the locking range according to Adler's condition. ....	57

<b>Figure 4.3</b>	Output frequency (dotted) in comparison to the injected frequency (solid). The dotted lines show the boundaries of the locking range according to Adler's condition.....	58
<b>Figure 4.4</b>	Calculated (solid) vs. estimated (dotted) $d\theta/dt$ , during the time interval in which the chirp frequency satisfies the Adler's condition. ....	59
<b>Figure 4.5</b>	Free-running oscillator frequency profile. Here, $d\omega_0/dt = 2 \times 10^{-7}$ . The dotted lines show the boundaries of the locking range according to Adler's condition.....	60
<b>Figure 4.6</b>	Output (dotted) vs. injected (solid) frequency. The dotted lines show the boundaries of the locking range according to Adler's condition. ....	61
<b>Figure 4.7</b>	Differential phase shift of the output signal. The injected signal is applied after $t = 2000$ . The dotted lines show the locking range according to Adler's condition.....	62
<b>Figure 4.8</b>	Calculated (solid) vs. estimated (solid) $d\theta/dt$ . ....	62
<b>Figure 5.1</b>	Piecewise continuous Gaussian random function $p(x)$ , $q(x)$ and $r(x)$ , with HWHM $\Delta p$ , $\Delta q$ , and $\Delta r$ , respectively. Here, $\Delta p = \Delta q = \Delta r = 0.3$ . ....	71
<b>Figure 5.2</b>	Power gain along $x$ assuming lossless circuit, perfect beam-circuit synchronization, and no perturbation. $C = 0.05$ . The maximum power gain at $x = 100$ is 647.19, or 28.11 dB.....	72
<b>Figure 5.3</b>	Power gain and output phase variation at $x = 100$ when the circuit phase velocity is perturbed. $b_0 = 0$ , $C = 0.05$ , and $\Delta q = 0.1$ (HWHM of 10% in circuit phase velocity). Without perturbation, power gain and output phase variation at $x = 100$ are respectively 647.19 and 0. ....	73
<b>Figure 5.4</b>	Power gain and output phase variation at $x = 100$ when the circuit phase velocity is perturbed. $b_0 = 0$ , $C = 0.05$ , and $\Delta q = 0.2$ (HWHM of 20% in circuit phase velocity). Without perturbation, power gain and output phase variation at $x = 100$ are respectively 647.19 and 0. ....	74
<b>Figure 5.5</b>	Mean value of power variation at $x = 100$ for different value of $\Delta q$ . $C = 0.05$ , $b_0 = 0$ .....	75
<b>Figure 5.6</b>	Mean value of the phase variation for different degrees of perturbations. Each data point represents 500 samples. The output phase is calculated at $x = 190$ , and $C = 0.021$ so the output power gain is 20dB when there is no perturbation. $b_0 = 0$ . ....	75
<b>Figure 5.7</b>	Standard deviation of the output phase variation for different degrees of perturbations in $v_p$ . ....	76
<b>Figure 5.8</b>	Power gain and output phase variation at $x = 100$ when the coupling parameter $C$ is perturbed. $C_0 = 0.05$ , and $\Delta p = 0.3$ (HWHM of 10% in	

	C). Without perturbation, power gain and output phase variation at $x = 100$ are respectively 647.19 and 0.....	78
<b>Figure 5.9</b>	Mean value of the phase variation for different degrees of perturbations in $C$ . Each data point represents 500 samples. The output phase is calculated at $x = 100$ , $C_0 = 0.05$ , and $b_0 = 0$ .....	79
<b>Figure 5.10</b>	Standard deviation of the output phase variation for different degrees of perturbations in $C$ .....	79
<b>Figure 5.11</b>	Power gain and output phase variation at $x = 100$ when the circuit loss $d$ is perturbed. $C_0 = 0.05$ , and $\Delta r = 0.4$ (HWHM of 40% in $d$ ). Without perturbation, power gain and output phase variation at $x = 100$ are respectively 16.87 and 0. ....	81
<b>Figure 5.12</b>	Mean value of the phase variation for different degrees of perturbations in $d$ . Each data point represents 500 samples. The output phase is calculated at $x = 100$ , $C_0 = 0.05$ , $b_0 = 0$ , and $d_0 = 1$ . ....	82
<b>Figure 5.13</b>	Standard deviation of the output phase variation for different degrees of perturbations in $d$ .....	82

## LIST OF APPENDICES

<b>Appendix A</b>	Electron orbits in sinusoidal and smooth-boundary magnetic field profiles.....	92
<b>Appendix B</b>	Generation of the random functions as an input to manufacturing error study. ....	95

# **ABSTRACT**

## **Theory of Injection Locking and Rapid Start-Up of Magnetrons, and Effects of Manufacturing Errors in Terahertz Traveling Wave Tubes**

by

**Phongphaeth Pengvanich**

Chair: Yue Ying Lau

In this thesis, several contemporary issues on coherent radiation sources are examined. They include the fast startup and the injection locking of microwave magnetrons, and the effects of random manufacturing errors on phase and small signal gain of terahertz traveling wave amplifiers.

In response to the rapid startup and low noise magnetron experiments performed at the University of Michigan that employed periodic azimuthal perturbations in the axial magnetic field, a systematic study of single particle orbits is performed for a crossed electric and periodic magnetic field. A parametric instability in the orbits, which brings a fraction of the electrons from the cathode toward the anode, is discovered. This offers an explanation of the rapid startup observed in the experiments.

A phase-locking model has been constructed from circuit theory to qualitatively explain various regimes observed in kilowatt magnetron injection-locking experiments, which were performed at the University of Michigan. These experiments utilize two

continuous-wave magnetrons; one functions as an oscillator and the other as a driver. Time and frequency domain solutions are developed from the model, allowing investigations into growth, saturation, and frequency response of the output. The model qualitatively recovers many of the phase-locking frequency characteristics observed in the experiments. Effects of frequency chirp and frequency perturbation on the phase and lockability have also been quantified.

Development of traveling wave amplifier operating at terahertz is a subject of current interest. The small circuit size has prompted a statistical analysis of the effects of random fabrication errors on phase and small signal gain of these amplifiers. The small signal theory is treated with a continuum model in which the electron beam is monoenergetic. Circuit perturbations that vary randomly along the beam axis are introduced through the dimensionless Pierce parameters describing the beam-wave velocity mismatch ( $b$ ), the gain parameter ( $C$ ), and the cold tube circuit loss ( $d$ ). Our study shows that perturbation in  $b$  dominates the other two in terms of power gain and phase shift. Extensive data show that standard deviation of the output phase is linearly proportional to standard deviation of the individual perturbations in  $b$ ,  $C$ , and  $d$ .

# CHAPTER 1

## INTRODUCTION

High power microwave and millimeter wave sources have been used for radars, communications, heating, spectroscopy, sensing, etc. [Bar01, Bar05]. Current developments have two main thrusts [Boo07]: a push toward high power at gigawatts (GW), and a push toward high frequencies at terahertz (THz). In the first case, high power refers to GW range, and in the latter case, high power refers to order of 1 W. There are many common physics and engineering issues that need to be solved in both areas, such as bright electron sources, beam optics, acceleration, transport, mode stability, arc protection, circuit optimization, energetic electron interactions with surfaces, output window, etc. In this thesis, we will examine several issues specific to each of these sources, namely, magnetron and traveling wave tube (TWT). These issues are motivated by ongoing experiments, and by future experiments being planned.

The magnetron is a promising device for the generation of GW microwaves at GHz. The traveling wave tube is a promising device for the generation of millimeter to submillimeter (THz) waves.

For the magnetron, this thesis uncovers a novel fast startup process that is inherent in the recent invention of magnetic priming at the University of Michigan [Nec03a, Nec05d], by which the magnetron noise was substantially reduced [Nec03a], and the

startup process noticeably hastened [Nec04]. This work generated significant interest [Jon04a, Jon05a, Lug04, Nec04, Nec05a, Nec05b, Nec05c]. It stimulated subsequent works in cathode priming [Nec03b, Jon04c, Jon05b, Jon05c, Fuk05, Fle06], and anode priming [Kim05, Kim06]. Also studied in this thesis is the injection locking of magnetrons, where the theory developed agrees well with the experiments which were also performed at the University of Michigan [Nec05b, Nec05c]. Effects of frequency perturbations on the locking process are also assessed.

For THz TWT, the experiments are far less advanced. Because of the high frequencies involved, the circuit size is minuscule [Boo05, Sch05]. This thesis analyzes an issue that is anticipated for future developments, namely, the effects of random manufacturing errors on the performance on such sources. A statistical analysis on the effects of the small signal gain and output phase variations as a result of random manufacturing errors has been performed.

As this thesis involves the magnetron and the traveling wave tube, the background of both devices is described in Sections 1.1 and 1.2 below. Novel results of this thesis are briefly summarized toward the end of these two sections.

## **1.1 MAGNETRON**

Magnetron is a microwave device which operates with a crossed electric and magnetic field. It is unique in its high-efficiency, robustness, and relative simplicity. The earliest magnetron development dates back to 1913 by Arthur Hull, and although the early devices only operated in the UHF region, Posthumous demonstrated in 1935 that magnetron efficiency as high as 50% could be realized [Ben87]. It was not until the

introduction of a cavity magnetron by Boot and Randall in 1939 [Boo76] that the first magnetron application in radar was implemented. During World War II, much effort was pushed toward magnetron development for radar applications, and by 1946 magnetron was able to generate an output power of 2 MW. Advanced magnetron geometries including the rising-sun and the strapping, which are widely used today for mode stability, were also developed during that time. Extensive theoretical studies of magnetron came during and after the war with contributions from Buneman, Hartree, Stoner, Slater, and others [Ben87]. While significant knowledge of magnetron operation has been gained, a complete magnetron theory still does not exist today. For example, there is still no first-principle theory to calculate even the DC voltage-current characteristics of a magnetron. Collins's and Slater's classic books [Col48, Sla51] remain valuable references for magnetron.

**Table 1.1** Typical parameters for conventional and relativistic magnetrons [Ben87].

<b>Parameter</b>	<b>Conventional</b>	<b>Relativistic</b>
Voltage	$\leq 100$ kV	$\sim 1$ MV
Cathode	Thermionic and secondary emission	Field emission
Current	$\sim 100$ A	$\sim 10$ kA
Pulse duration	$\geq 1$ $\mu$ s	$\leq 100$ ns
Risetime	$\leq 200$ kV/ $\mu$ s	$\sim 100$ kV/ns
Power	$\leq 10$ MW	$\geq 1$ GW
Efficiency	50% - 90%	$\leq 30\%$

Most of the magnetron development prior to 1975 was mainly for the *conventional* magnetrons, i.e. non-relativistic with applied voltage less than 500 kV, where the maximum microwave power was limited to MW range. With the increasing

interest in GW-range microwave source [Bar01, Bar05, Ben92], another type of magnetron, namely, *relativistic* magnetron, has gained significant interest after the MIT team led by Bekefi, together with his students, Orzechowski and Palevsky, first reported a measured microwave output power of 900 MW from the experimental relativistic magnetron in 1975 [Bek76, Ben87, Pal79, Pal80]. Typical operating and output parameters for conventional and relativistic magnetrons are given in Table 1.1. Although there are many subtle differences between the conventional and the relativistic magnetrons, it turns out that many of the concepts developed for the conventional magnetron can also be applied to the relativistic magnetron. Among them are the Buneman-Hartree and the Hull cutoff conditions, which are used to determine necessary magnetron operating conditions. Before getting into the details of these conditions, however, it is necessary to introduce a simplified model of magnetron as the starting point of the study.

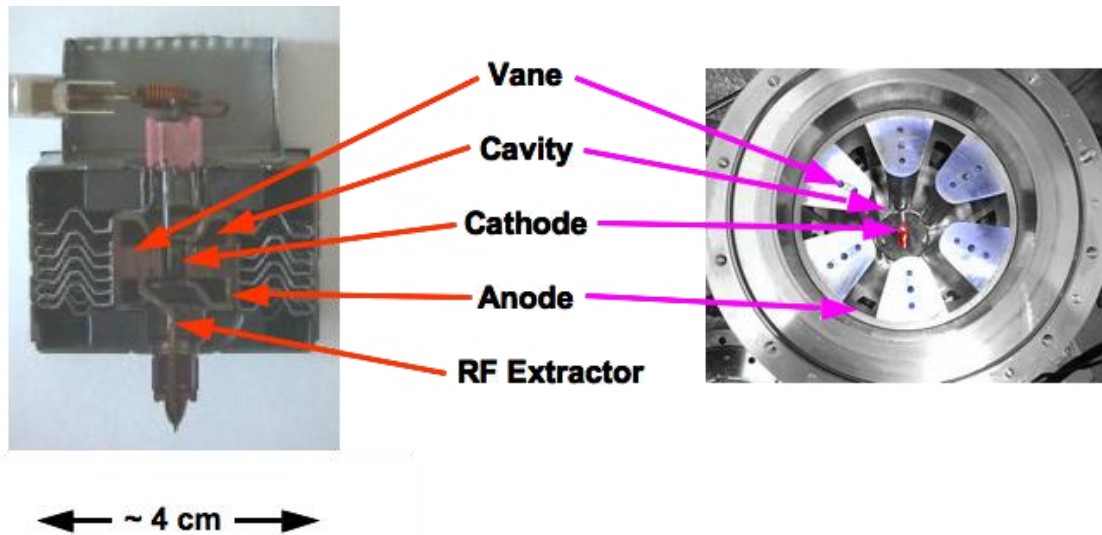


**Figure 1.1** Conventional and relativistic magnetrons. The left-hand-side is a cut-through of a kW conventional magnetron used in microwave oven [Nec05b]. The right-hand-side is a picture from the University of Michigan’s relativistic magnetron [Whi05].

A conventional magnetron and a relativistic magnetron are shown side-by-side in Figure 1.1. An external voltage source is used to supply the potential difference between the cathode and the anode. Typically, the cathode is charged negatively while the anode is grounded. Electrons are emitted from the cathode either by thermionic and secondary emission as in a conventional magnetron, or by field emission as in a relativistic magnetron. A constant axial magnetic field is applied, and if the magnetic field is sufficiently strong, the emitted electrons would be constrained within the interaction space between the anode and the cathode. The presence of the corrugated wall on the anode supports various modes of the RF field, some of which would be strongly excited by electron-wave interaction within the interaction space. Each of these modes corresponds to different resonance frequency and electronic efficiency. Competition between different operating modes of magnetron remains one of the most important problems in magnetron study, especially in the relativistic magnetron which has much lower efficiency than the conventional magnetron as shown in Table 1.1. The rising-sun and the strapping techniques for magnetrons have been developed for good mode selection [Col48, Sla51]. These techniques, however, are not applicable to relativistic magnetrons because of the high field stress that would lead to arcing and field emission. The output RF power is extracted from the cavity through the RF extractor. Although not shown in Figure 1.1, RF extractor in the relativistic magnetron is normally connected to several of the resonators on the anode wall. A recent review of magnetrons and crossed-field amplifiers is given in [Gil05].

A simplified model of magnetron is shown in Figure 1.2(a). Although it is possible to study magnetron in cylindrical coordinates, many magnetron mechanisms also

present themselves in the planar model shown in Figure 1.2(b). Several magnetron studies, especially those that focus on mechanisms during the start-up phase when the RF is still infinitesimally small, typically utilize this planar model as a basis. Since the corrugated wall comes into play only in the presence of the RF, a smooth anode is often considered as a replacement. Chapter 2 of this thesis will also use the smooth planar model in the analysis of the start-up phase.

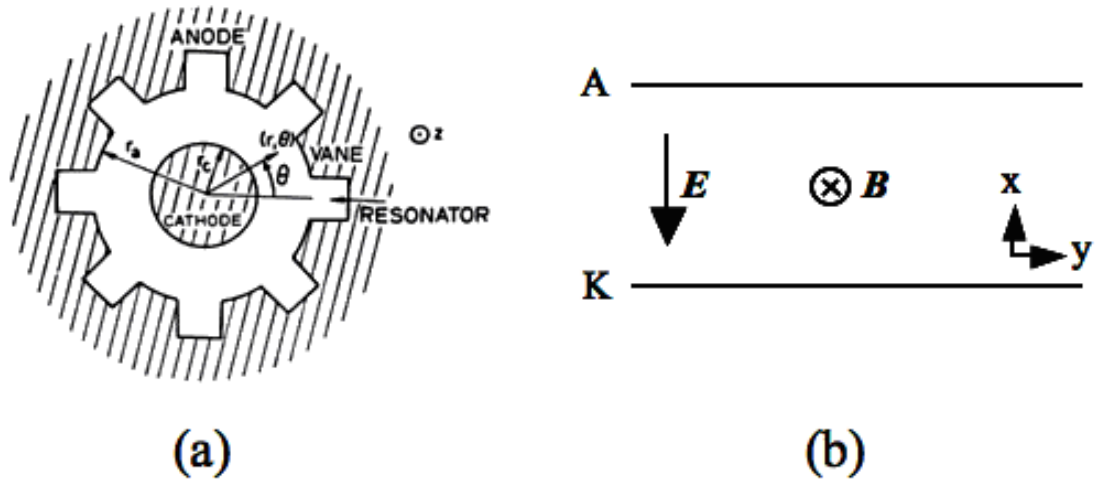


**Figure 1.2** Illustration of (a) the cylindrical model [Lau87] and (b) the planar model which are typically used in magnetron study.

In the planar magnetron model shown in Figure 1.2(b), electrons are first assumed to enter from the cathode with zero velocity. The presence of the electric and the magnetic fields cause the electrons to move in the  $y$ -direction with the  $E \times B$  drift. The electrons would reside in a region near the cathode called the Brillouin hub in such a way that the electron velocity at the cathode is zero, and increases linearly to the top of the hub height [Lau87, Sla51]. This type of flow is called Brillouin flow, and has been confirmed in computer simulations [Chr96, Pal80]. Brillouin flow requires that  $\omega_p = \omega_c$ , where  $\omega_p$  and  $\omega_c$  are respectively the plasma and the cyclotron frequencies.

For magnetron to operate, the Brillouin hub height should never reach the anode. The relationship between the magnetic field and the voltage when the hub height becomes the same as the A-K gap separation is called the Hull cutoff condition. For a non-relativistic planar magnetron, the Hull cutoff condition reads

$$V_c = \frac{1}{2} \frac{|e|}{m_0} B_0^2 D^2 \quad (1.1)$$

where  $V_c$  is the Hull cutoff voltage,  $B_0$  is the magnetic field, and  $D$  is the A-K gap separation. For a given magnetic field,  $V_c$  gives the upper limit of the magnetron operating voltage.

Another operating condition, as mentioned earlier, is the Buneman-Hartree condition [Ben87, Lau87, Sla51, Ben07]. In order for the electrons to interact with the RF, the electron drift velocity and the RF wave phase velocity ( $v_{ph}$ ), both in the  $y$ -direction as shown in Figure 1.2b, need to be in synchronism. The voltage at which this condition occurs is called the Buneman-Hartree threshold voltage ( $V_{BH}$ ), and is given by, for a non-relativistic planar magnetron,

$$V_{BH} = B_0 D v_{ph} - \frac{m_0}{2|e|} v_{ph}^2. \quad (1.2)$$

The RF wave phase velocity depends on mode. For a given magnetic field, the Buneman-Hartree condition gives the lower limit of the magnetron operating voltage.

The detailed derivations, as well as the relativistic and the cylindrical forms, of both the Buneman-Hartree and the Hull cutoff conditions can be found in general high-power microwave text (see, e.g., [Ben07, Lau87]).

Synchronism between the electrons and the RF field in the magnetron cavity leads to particle-wave interactions that result in mechanisms like phase focusing and spoke

formation, which further strengthens the RF generation as discussed below. The RF field inside the magnetron, in addition to the DC electric field which points from the anode to the cathode, can be assumed to take the form as shown in Figure 1.3. At synchronism, the RF field moves in the  $y$ -direction (or  $\theta$ -direction for cylindrical model) at the phase velocity  $V_{ph}$ , which is approximately equal to the unperturbed  $E \times B$  drift velocity of the electrons. Consider electrons A and B in Figure 1.3. Without the RF field, both electrons would move in the positive  $y$ -direction as a result of the unperturbed  $E \times B$  drift. The presence of the RF field causes electron A to drift toward the cathode and gain its potential energy from the RF field, while electron B loses its energy to the RF field and drifts toward the anode. Since the RF field is stronger near the anode, the energy converted from electron B to the RF field is higher than the energy converted from the RF field to electron A, resulting in net gain of energy to the RF field. The situation is, in reality, far more complicated due to the presence of space-charge. Further explanation on the subject can be found in [Sla51]. In any case, this conversion of the potential energy to RF field energy is the major gain mechanism of a magnetron.

Another unique mechanism responsible for magnetron's high efficiency is phase-focusing. The presence of the RF field creates favorable phase where electrons give energy to the RF field, e.g., electron B in Figure 1.3, and unfavorable phase where electrons take away energy from the RF field, e.g., electron A. Electrons in the favorable phase tend to remain in synchronism with the RF by the self-focusing effect. To see this, when the drift velocity of electron B in the favorable phase becomes larger, electron B would enter the region where the RF field is in the opposite direction of the DC field, causing it to slow down. If the drift velocity of electron B decreases, however, electron B

would enter the region where the RF field is in the same direction as the DC field, causing it to speed up. Thus, electrons which are similar to electron B will remain in the favorable phase. On the contrary, electron A in the unfavorable phase tends to fall out of synchronism with the RF. When electron A speeds up in the unfavorable phase, it would enter the region where the RF field is in the same direction as the DC field, causing it to speed up further. When electron A slows down in the unfavorable phase, it would enter the region where the RF field is in the opposite direction of the DC field, causing it to slow down further. Electrons which are similar to electron A will eventually enter the favorable region, resulting in bunching. This phase-focusing mechanism is the reason for electron spokes to be formed, and they are in the favorable phase.

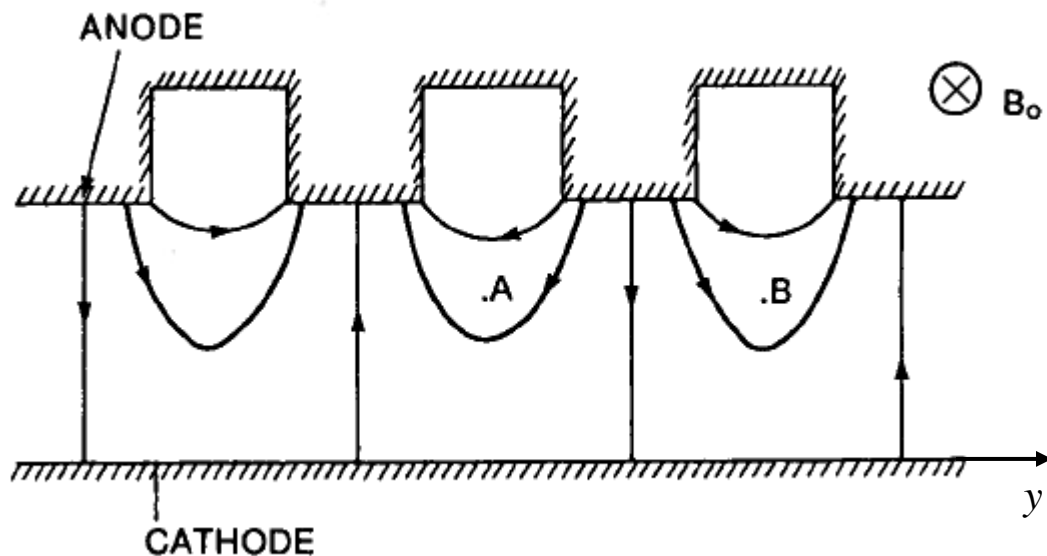


**Figure 1.3** RF electric field inside the A-K gap for a planar magnetron [Lau87].

Theoretical studies of magnetron performance in the presence of the RF field were conducted by, notably among others, Slater [Sl51] and Vaughan [Vau73]. Slater examined interactions and energy transfer between electrons and RF field, and considered

resonance circuit modes of magnetron. Vaughan focused on the lumped-spoke analysis, which treated the electron spoke as a single element of charge in order to find the induced current in a magnetron. The lumped-circuit analysis of general oscillator with an inclusion of the magnetron-specific model suggested by Slater has also been used successfully in magnetron injection locking research [Che90a, Che90b, Pen05]. The latter becomes the basis of the study in Chapters 3 and 4 of this thesis.

Chapter 2 describes an alternative mechanism due to magnetic priming which also leads to electron bunching and spoke formation. Magnetic priming [Nec03a, Nec05d] is achieved when periodic variations of the magnetic field are introduced along the  $E \times B$  drift direction, the  $y$ -direction in Figure 1.2b. A model is shown in Figure 2.1 below. Single particle orbit considerations show that the cycloidal orbits of electrons in a gap with a crossed electric and magnetic field lead to rapid spoke formation if the external magnetic field has such periodic variation. This rapid spoke formation with magnetic priming is primarily the result of kinematic bunching before the RF electric field and the space-charge field are set up. A parametric instability in the orbits, which brings a fraction of the electrons from the cathode to the anode region, is discovered. These results are examined in light of the rapid startup, low noise magnetron experiments and simulations that employed periodic, azimuthal perturbations in the axial magnetic field [Lug04, Nec04].

In Chapter 3, an injection locking model is developed from circuit theory to qualitatively explain the various regimes observed in magnetron injection-locking experiments [Nec05b, Pen05]. The experiments utilized two continuous-wave oven magnetrons: one functioned as an oscillator and the other as a driver. The model includes

both magnetron-specific electronic conductance and frequency-pulling parameter. Both time and frequency domain solutions are developed from the model, allowing investigations into the growth and saturation as well as the frequency response of the output signal. This simplified model recovers qualitatively many of the phase-locking frequency characteristics. Chapter 4 extends the numerical findings of Chapter 3 to allow frequency perturbation during the injection locking process.

## 1.2 TRAVELING WAVE TUBE

Traveling wave tube (TWT), or traveling wave amplifier, is a linear-beam device. It can deliver MW-level of microwave power in the GHz range [Gil86, Gil94]. Early work on TWT was conducted in 1940s by Lindenblad and Kompfner [Kom47] during World War II. Extensive theoretical studies on TWT came after the war, and were led by Pierce from Bell Telephone Laboratories [Pie47, Pie50]. Pierce's theory has since become the basis of virtually all TWT studies, including the work in this thesis.

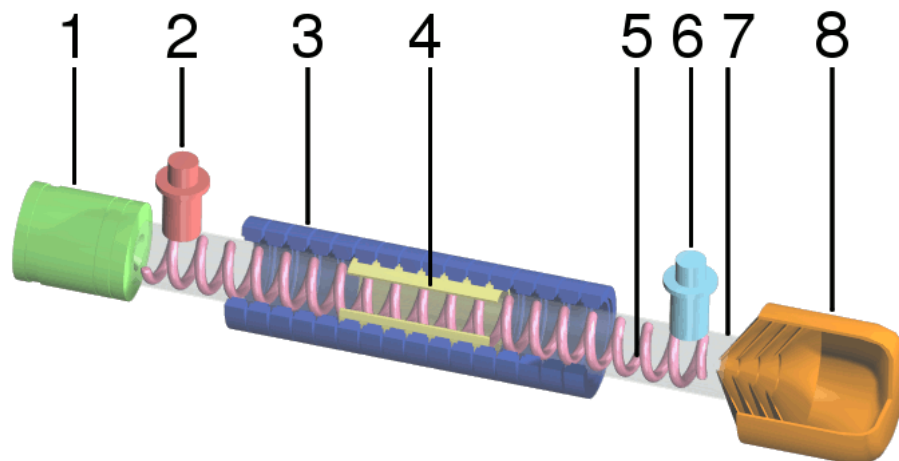


**Figure 1.4** Basic model of helix TWT showing 1) electron gun, 2) RF input, 3) magnets, 4) attenuator, 5) helix coil, 6) RF output, 7) vacuum tube, and 8) collector [Pie04].

There are several types of TWT: the helix type, which is normally used for broadband applications, the coupled cavity type, which is used for high-power applications, and the folded waveguide [Ha98], which is currently being considered for THz amplification. We shall discuss the helix type TWT, for illustration purposes, as Pierce's theory has been used for all types.

A basic model of helix TWT is shown in Figure 1.4 [Pie04]. Electron beam is injected from the electron gun (1) toward the collector (8). A low-amplitude RF input signal (2) is injected into the TWT, and the amplified signal is collected at the RF output (6) located at downstream. The RF, having to travel a longer path length along the helix (5), will then have the projected axial velocity the same as the electrons' axial velocity, which is lower than the speed of light. Principal operation of TWT relies on continuous interactions between the electron beam and the traveling RF. For interactions to occur, the projected axial velocity of the RF needs to be approximately the same as the beam velocity. This synchronism can be controlled by the beam voltage, once the pitch angle of the helix (i.e., circuit phase velocity) is fixed. At synchronism, the RF electric field pattern in the electron beam's frame of reference would appear as shown in Figure 1.5 [Gil94]. The RF electric field causes electrons in the beam to propagate away from the negatively charged region (region B in Figure 1.5) toward the positively charged region (region A), resulting in electron bunching. Region A on the helix is positively charged, as it is the image charge of the electron bunch. Assuming that the beam travels to the right, electrons to the left of region A would be accelerated toward region A, while electrons to the right of region A would be decelerated back to region A. This tendency toward electron bunching enhances the RF electric field, which in turn reinforces the

beam bunching. When the electron bunch falls into the decelerating phase, the beam kinetic energy is converted to the RF energy, causing the RF to grow. The decelerated electrons spend a longer time interacting with the wave than the accelerated electrons when the beam velocity slightly exceeds the wave phase velocity, resulting in net gain of energy to the wave.

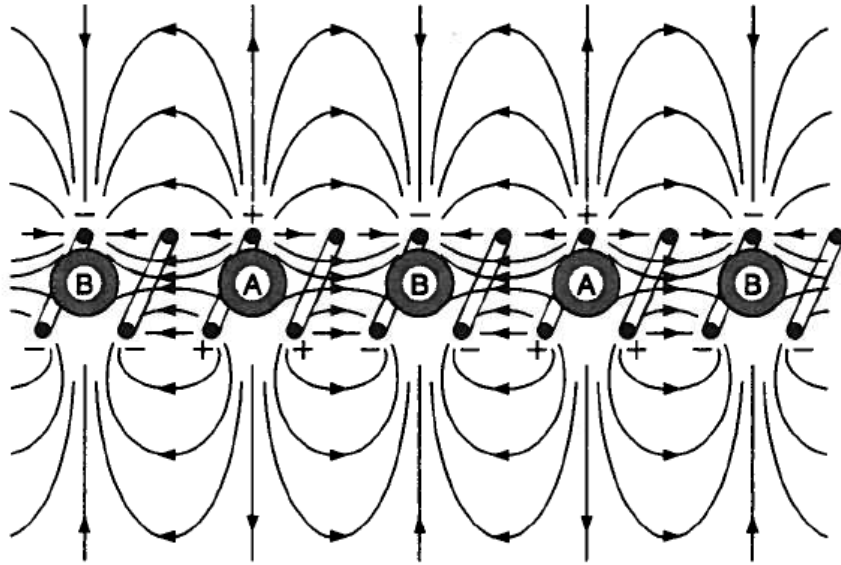


**Figure 1.5** Field pattern on the helix TWT [Gil94].

The electron beam in TWT, unlike magnetron, is well defined. This is why the beam-wave interaction theory, as developed by Pierce [Pie50], can be distinctly divided into the beam analysis part and the RF circuit analysis part. Detailed analysis of Pierce's dispersion relation and comprehensive knowledge on TWT operation can be found in [Gew65, Gil94].

In Chapter 5, evaluation of the statistical effects of random fabrication errors on a traveling wave tube amplifier's small signal characteristics is presented. The study is motivated by the current interest in mm-wave and THz sources [Boo07], which use

miniature, difficult-to-fabricate TWT [Boo05, Sch05]. The small signal theory is treated in a continuum model in which the electron beam is assumed to be monoenergetic. Perturbations in circuit dimensions that vary randomly along the beam axis are introduced in the dimensionless Pierce parameters  $b$ , the beam-wave velocity mismatch,  $C$ , the gain parameter, and  $d$ , the cold tube circuit loss. The study shows that perturbation in the circuit phase velocity dominates the other two, and numerical data suggest that the standard deviation of the output phase is linearly proportional to the standard deviation of the individual perturbations in  $b$ ,  $C$ , and  $d$ .

### **1.3 THESIS ORGANIZATION**

Following the above summaries, Chapter 2 explores rapid kinematic bunching and parametric instability in a crossed-field gap with a periodic magnetic field. Chapter 3 presents the model and its comparison with experiments of magnetron injection locking. Chapter 4 investigates effect of frequency chirp on magnetron injection locking. Chapter 5 studies effect of random circuit fabrication errors on small signal gain and phase in helix traveling wave tubes. The conclusions and suggestions for future work are given in Chapter 6.

## CHAPTER 2

# PARAMETRIC INSTABILITY IN ELECTRON ORBITS IN A CROSSED-FIELD GAP WITH A PERIODIC MAGNETIC FIELD

### 2.1 INTRODUCTION

Previous experiments at the University of Michigan have shown that the sidebands and the close-in noise in a microwave oven magnetron may be reduced by more than 30 dB by the addition of an azimuthally varying axial magnetic field [Nec03a, Nec04, Nec05a, Nec05b, Gil05]. Noise reduction for 2.45-GHz microwave oven magnetrons is an important issue, as there exists an increasing concern about signal interference for cordless phones and wireless communication systems which also operate in this unlicensed frequency band [Ose95a, Ose95b]. Not only low noise behavior was observed, but also the startup was found to substantially hasten, i.e., startup current was significantly reduced, when the number of the perturbing magnets equals the number of electron spokes in the operating mode of the magnetron (usually the pi-mode, in which the radio frequency (RF) electric field differs by  $\pi$  between neighboring cavities [Lau03, Jon04a, Nec04, Nec05d]). This technique was termed “magnetic priming” and for an  $N$ -cavity magnetron operating in the pi-mode; it consists of imposition of  $N/2$  azimuthal magnetic field perturbations [Jon04a]. The fast startup and the tendency toward low-

noise operation in a magnetically primed oven magnetron were corroborated in a recent three-dimensional particle-in-cell simulation [Lug04].

The low noise operation resulting from magnetic priming could also have important implications to crossed-field amplifiers [Bro95a, Che96, Dom95, Gil05, Hil95, Mac94]. The instantaneous locking onto the pi-mode, from the very low to high current throughout that was demonstrated for the oven magnetron [Nec05a, Nec05b], offers interesting possibilities on significant improvements of mode stability in gigawatt class relativistic magnetrons [Lem99, Lem00, Lop02, Hof07]. Detailed discussion regarding magnetron noise can be found in [Nec05b].

Despite the attractive features revealed by magnetic priming, crossed-field electron devices in general, and the noise generated in them in particular, are notoriously difficult to understand and to analyze [Gil05, Gra87, Lau87, Ose95b, Sa195]. They have few counterparts in the much better understood electron beam-driven devices such as the klystron, traveling wave tube, gyrotron, and free electron laser [Gra87]. Thus, the additional embodiments associated with the azimuthal perturbations in the axial magnetic field in the low-noise magnetron [Jon04a, Lug04, Nec03a, Nec04, Nec05a, Nec05b, Nec05d] prompted an analysis beginning with single particle orbits, which is the subject of this chapter. First, electron spokes are immediately formed, in less than one cycloidal orbit, due to the periodic magnetic field variation [Nec05c]. This remarkably short bunching length is in sharp contrast to the bunching in a klystron or in a traveling wave tube which require some 85% of the tube length to significantly bunch the beam before the RF power is extracted from the remaining 15% of the tube length [Nec05c]. Second, the present author discovers a parametric instability in the electron orbit which is due

solely to the periodic perturbing magnetic field, also reported in [Nec05c]. This parametric instability brings a fraction of electrons toward the anode. This is interesting since removal of “excess electrons” from the cathode region has often been speculated as crucial to the previously observed low noise states in magnetron and crossed-field amplifiers [Bro95a, Bro95b, Gil05, Hil95, Mcd04]. Third, our calculations are based on a nonresonant structure, so the important role played by the RF electric field is absent. Thus, the calculations presented here provide deeper insight into the startup phase. The low noise behavior is considerably more difficult to explain, and will be discussed in the last section of this chapter.

## 2.2 THE MODEL

For simplicity, we use a planar model to mimic the circular geometry of a magnetron as shown in Figure 1.2(b). Electrons are emitted from the cathode, located at  $x = 0$ , with zero initial velocity. The electrons are subjected to a uniform DC electric field,  $\mathbf{E} = -\mathbf{x}E_0$ . A periodic magnetic field,  $\mathbf{B} = \mathbf{z}B(y)$ , is imposed

$$B(y) = B_0 + \delta B(y) \equiv B_0[1 - \alpha p(y)], \quad (2.1)$$

where  $B_0$  is the uniform magnetic field,  $\alpha$  measures the fractional magnetic field variation, i.e., the strength of magnetic priming, and  $p(y)$  is a periodic function of  $y$  with period  $\lambda$ , and is bounded by 0 and 1. Thus, the external magnetic field has values between  $B_0$  and  $B_0(1 - \alpha)$ . We focus mainly on  $\alpha = 0.267$ , roughly corresponding to the maximum magnetic field variations in [Jon04a]. The effect of  $\alpha$  on electron dynamics that shows the key signature of the presence of a parametric instability will be discussed in Section 2.3. For simplicity of illustration, we set  $p(y)$  to be a square-wave function as

shown in Figure 2.1. We shall calculate the electron orbits subject to the static electric field and the periodically perturbed magnetic field. All effects from space charge, RF fields, and RF circuit geometries are ignored, and the calculations are nonrelativistic. Thus, all bunching and spoke formation, if occur, are essentially kinematic in nature.

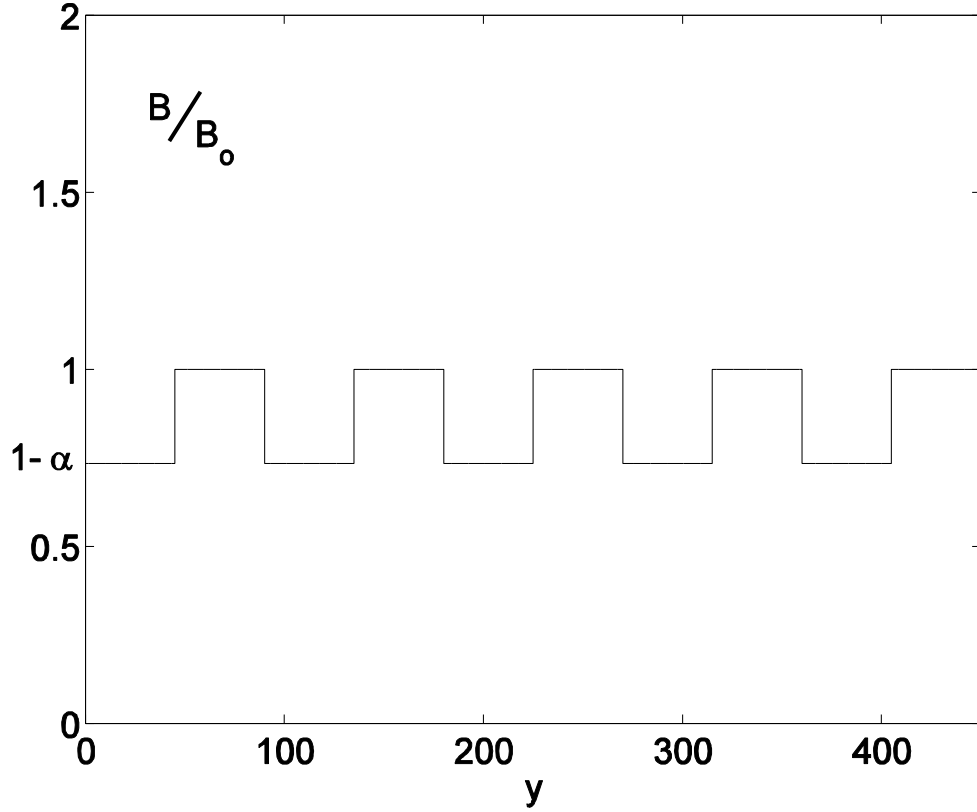


**Figure 2.1** The normalized magnetic field distribution,  $B/B_0 = 1 - \alpha p(y)$ , as a function of  $y$ , the normalized distance in the  $E \times B$  drift direction.

Hereafter, we normalize the magnetic field by  $B_0$ , time by  $1/\Omega$ , the inverse of cyclotron frequency  $\Omega = eB_0/m$ , and distance by the length scale  $L = eE_0/m\Omega^2$ . With these normalized variables, the familiar cycloidal orbital equations for the case of uniform magnetic field ( $\alpha = 0$ ) read

$$x(t) = 1 - \cos(t), \quad y(t) = t - \sin(t). \quad (2.2)$$

Equation (2.2) represents the base case when magnetic priming is absent, i.e. when  $\alpha = 0$  in Figure 2.1. In one cycloid, the hopping time  $T$  is  $2\pi$ , the hopping distance in  $y$  is also  $2\pi$ , and the maximum excursion in  $x$  is 2 for the base case. This maximum excursion in  $x$  is roughly (but slightly larger than) the Brillouin hub height [Lau87], which is typically about one third of the anode-cathode separation in a magnetron. Since the maximum cycloidal orbit height is at  $x = 2$ , we shall estimate that the maximum Brillouin hub height is at  $x = 1$  for the base case. Then, if the perturbing magnetic field brings an electron to  $x$ -coordinate of order 5 and beyond, we consider the electron's journey well toward the (imaginary) anode. Except otherwise specified,  $p(y)$  has a periodicity  $\lambda = 90$  units in  $y$ , as shown in Figure 2.1.

The orbital equations for an electron emitted at  $t = 0$  with initial coordinates  $(x, y) = (0, y_0)$  follow. Upon integrating the  $x$ -component of the force law, one obtains in the normalized variables

$$\dot{x} = t - A(y) + A(y_0), \quad (2.3)$$

where the dot denotes a time derivative and the normalized vector potential  $A(y)$  is defined by  $B(y) = dA(y)/dy = 1 - \alpha p(y)$ . Upon using (2.3) in the  $y$ -component of the force law, one obtains

$$\ddot{y} = [t - A(y) + A(y_0)][1 - \alpha p(y)]. \quad (2.4)$$

The initial conditions to (2.3) and (2.4) at  $t = 0$  are  $x = 0$ ,  $y = y_0$ ,  $dy/dt = 0$ . For completeness, we record the energy conservation relation

$$\dot{x}^2 + \dot{y}^2 = 2x. \quad (2.5)$$

Any two of the three equations, (2.3), (2.4), and (2.5), imply the third. Equation (2.4) is a nonlinear second order ordinary differential equation which contains three intrinsic

periodicities: the cyclotron frequencies associated with the two levels of the magnetic fields, and the periodicity associated with the magnetic perturbation period, all shown in Figure 2.1. It is therefore hardly surprising that certain orbits would exhibit some form of parametric instability with an exponential growth at some stage, according to (2.4) [Che84].

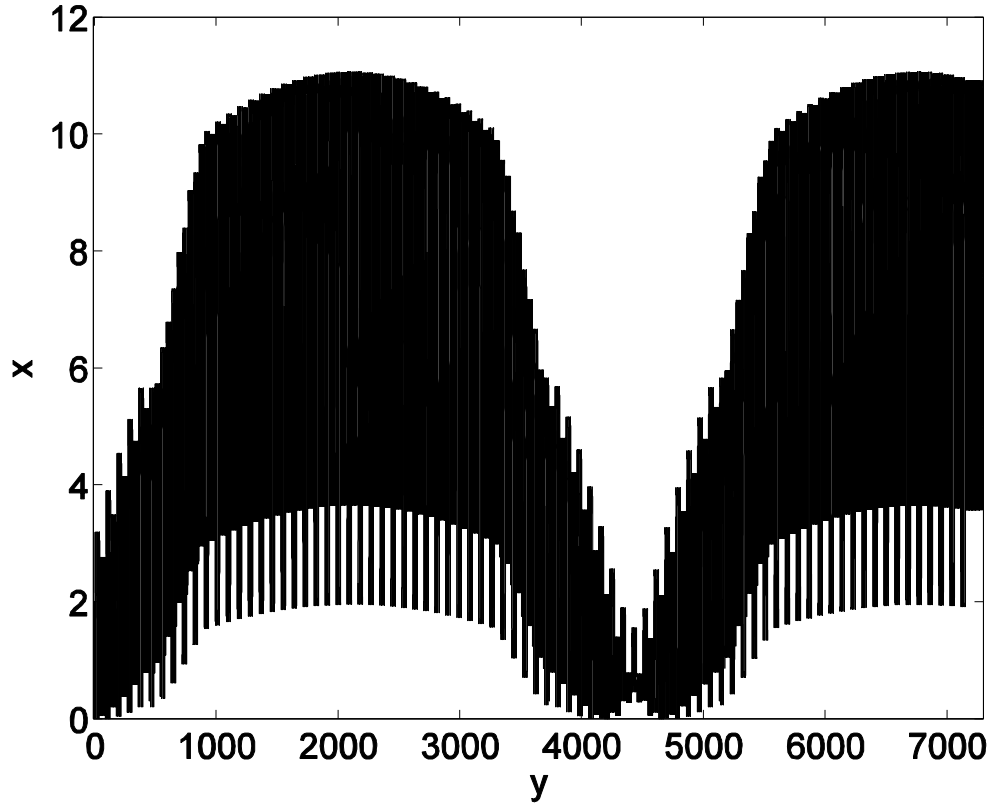


**Figure 2.2** A single electron orbit that is emitted with the initial coordinates  $(x, y) = (0, y_0)$  with  $y_0 = -1.903\pi$ ,  $p(y)$  has a periodicity of  $\lambda = 90$  units in  $y$ .

### 2.3 THE RESULTS

Figure 2.2 shows the orbit of a single electron that is emitted with the initial coordinates  $(x, y) = (0, y_0)$  with  $y_0 = -1.903\pi$ , and continues its trajectory over 80 magnetic field perturbation periods. Note that there is an exponential growth of the

displacement, at least initially, before settling into a large-amplitude periodic oscillation. The maximum excursion in  $x$  for this electron is about 11, which is well beyond the anode region. Figure 2.3 shows the maximum excursion in  $x$ , as a function of the initial position at  $(0, y_0)$ . Some orbits do not display an exponential growth, but still expand significantly in the  $x$ -direction, and this expansion solely depends on the presence of the magnetic field variation in  $y$ . Maximum excursion in  $x$  for different types of magnetic field profiles has been studied and the results can be found in Appendix A.

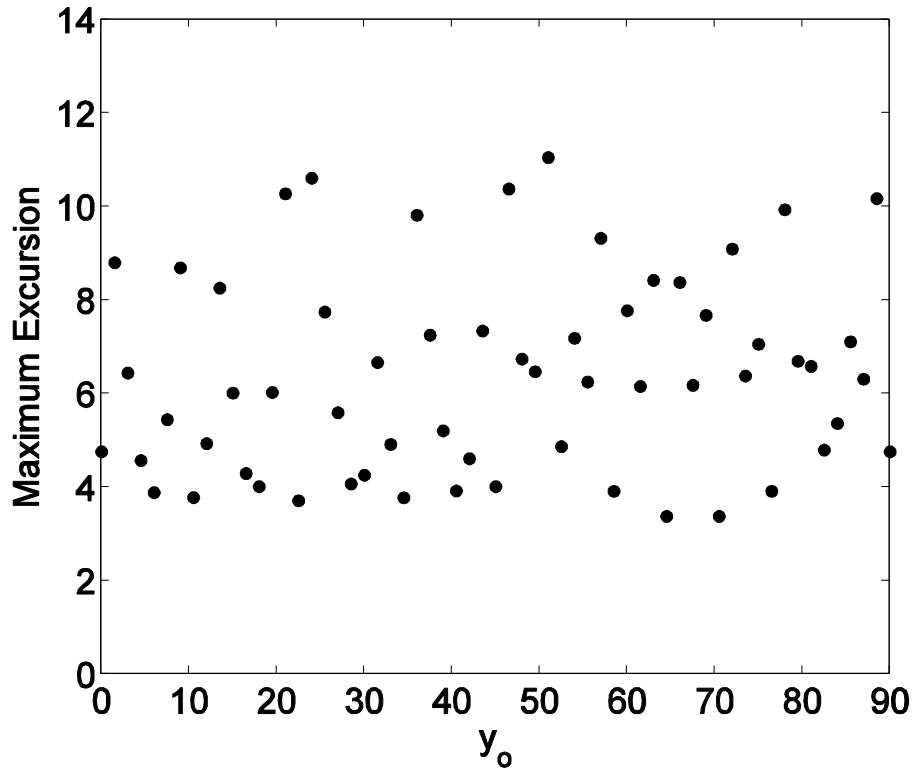


**Figure 2.3** Maximum excursion as a function of the electron's initial coordinates  $(x, y) = (0, y_0)$ ,  $p(y)$  has a periodicity of  $\lambda = 90$  units in  $y$ .

The exponential growth in the orbital displacement is clearly seen in Figure 2.4, obtained by Y. Hidaka [Nec05c] with  $\alpha = 0.267$ , but with only a slight modification in the periodicity in  $p(y)$ , from  $\lambda = 90$  to  $\lambda = 90.2$  units, for the initial condition  $(0, y_0) = (0, -$

$0.9936\pi$ ). (If  $\alpha = 0$ , the orbits in the compressed scales of Figures 2.2 and 2.4 would look like a series of vertical bars extending from  $x = 0$  and  $x = 2$ .)

The existence of a parametric instability can be further supported and generalized by considering the three characteristic frequencies identified towards the end of Section 2.2:  $\Omega_1$  and  $\Omega_2$ , respectively the electron cyclotron frequencies associated with the maximum and minimum magnetic fields, and  $\Omega_3$ , which is due to the electron movement at a constant average parallel velocity,  $v_{avg}$ , through a periodic structure and can be written as,

$$\Omega_3 = k \cdot v_{avg} . \tag{2.6}$$

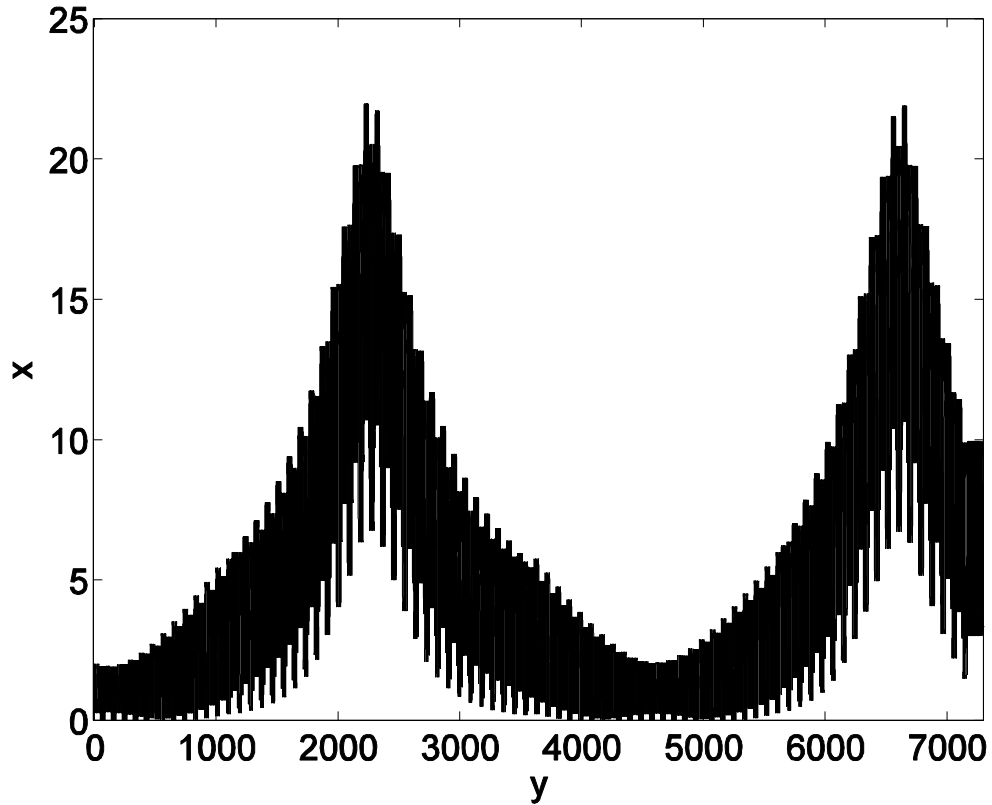


**Figure 2.4** A single electron orbit that is emitted with the initial coordinates  $(x, y) = (0, y_0)$  with  $y_0 = -0.9936\pi$ . In this figure,  $p(y)$  has a periodicity of  $\lambda = 90.2$  units in  $y$  [Nec05c].

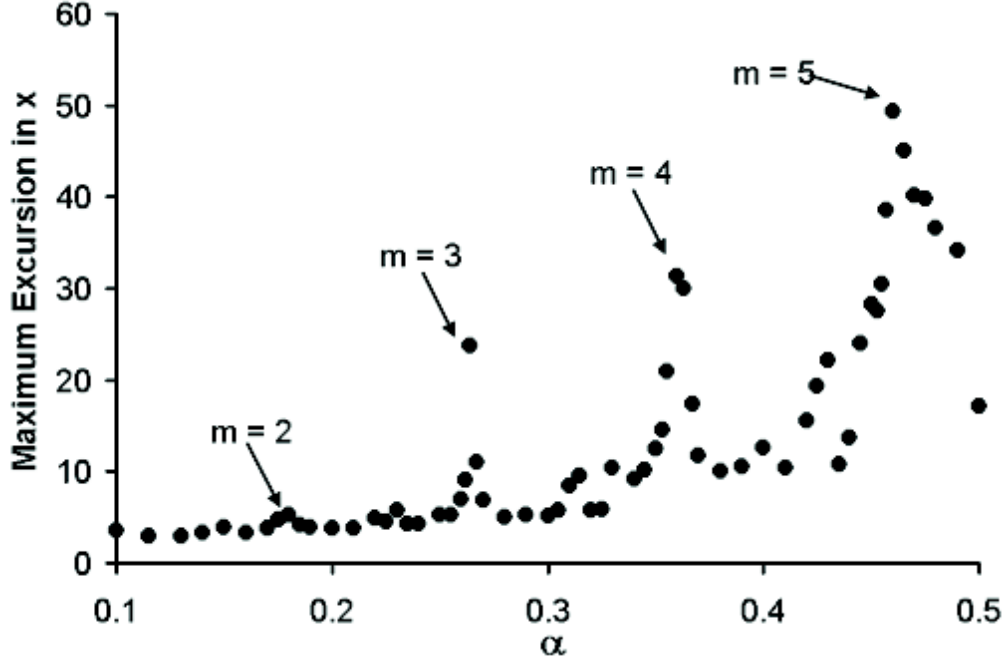


**Figure 2.5** Electron maximum excursion as a function of  $\alpha$ , when  $\lambda = 90$ . The electron maximum excursion peaks in certain bands of  $\alpha$ .

In (2.6),  $k = 2\pi/\lambda$  is the wave number corresponding to the period of magnetic priming (in our model the magnetic priming has a spatial periodicity of  $\lambda = 90$  as in Figure 2.1) and  $v_{avg}$  is the average  $E \times B$  drift through the static electric and the magnetic fields.

The maximum excursion of electrons peaks at some values of  $\alpha$ . The following relationship is observed at each of these peaks

$$\Omega_1 - \Omega_2 = m\Omega_3, \quad (2.7)$$

where  $m = 2, 3, 4, 5$  as seen in Figure 2.5. Note that in our normalization,  $\Omega_1 = 1$ , and  $\Omega_2 = 1 - \alpha$ . The compact formula (2.7) captures the essential information from the physical model developed, as it includes the parameters that *completely* control the electron dynamics (e.g., the amplitude and periodicity of the magnetic field variation). Equation

(2.7) is a well-known relationship for parametric instability [Che84], as it represents the beating of two natural frequencies ( $\Omega_1, \Omega_2$ ) with the harmonics of the third natural frequency ( $\Omega_3$ ). Note that the  $m = 1$  case does not show a parametric instability probably because the “pump” (measured by the degree of magnetic priming parameter  $\alpha$ ) is not sufficiently strong to overcome the velocity spread associated with  $v_{avg}$ . The maximum excursion is in general reduced for smoother variations of the magnetic field profile  $p(y)$ .

A close examination of the phase space diagram in the orbit such as that shown in Figure 2.4 shows that the orbit is not chaotic in nature, despite the presence of the parametric instability. As shown in Figure 2.6, the orbit is not chaotic despite significant growth in the x-excursion due to orbital parametric instability.

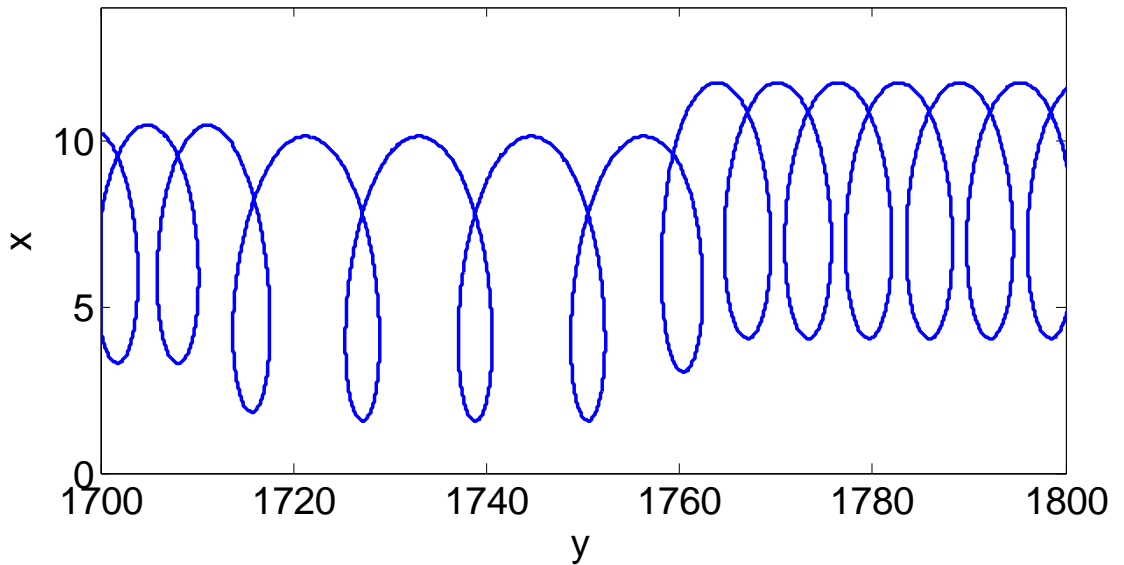


**Figure 2.6** A zoom-in single electron orbit that is emitted with the initial coordinates  $(x, y) = (0, y_0)$  with  $y_0 = -0.9936\pi$ ,  $p(y)$  has a periodicity of  $\lambda = 90.2$  units in  $y$ .

In the ten-cavity microwave oven magnetron, the optimal operation for low noise and fast startup involves five axial magnetic field variations along the azimuth in the circular format [Lau03, Jon04a, Lug04, Nec04, Nec05b, Nec05d]. To model electron

recirculation, we shall assume that an electron leaving the fifth magnetic perturbation in Figure 2.1 reenters the first magnetic perturbation with the acquired velocity and displacement as the initial condition for the next round of recirculation. This is equivalent to a periodic boundary condition for the particles at  $y = 0$  and  $y = 450$ . In this optimal configuration, which is to be modeled here, there are about 14.3 hopping distances in  $y$  (14.3 cycloids) over one magnetic perturbation period. Thus, an electron hops about 71.5 times going once around the “cathode” which has a total of 5 magnetic perturbations, and the cathode circumference is roughly  $71.5 \times 2\pi = 450$  units [cf. Equation (2.2)]. The recirculation time, i.e. the time required for the electron to go once around the (circular) cathode, is also roughly 450 units.

It is natural to expect that kinematic bunching occur within one cycloidal period as a result of the magnetic perturbations. Shown in Figure 2.7(a) are the five electron bunches that are immediately formed, after about only half the cycloidal orbit after emission ( $t = 4$ ). Figure 2.7(b) shows the five bunches at  $t = 73$ . Figure 2.7(c) shows the electron bunches after the electrons travel once around the (circular) cathode, at  $t = 454$ . Note that at this time, the electrons form a spoke-like structure that extends significantly to the anode region. Recall that these spokes are *not* due to the RF mode, as there is none; nor to any vane structure. They are purely due to magnetic priming, i.e. to the periodic magnetic perturbations in  $y$ , which in turn lead to a large  $x$ -excursion due to a parametric process. After 3 revolutions around the cathode ( $t = 1314$ ), the spokes are well into the anode region, as shown in Figure 2.7(d).

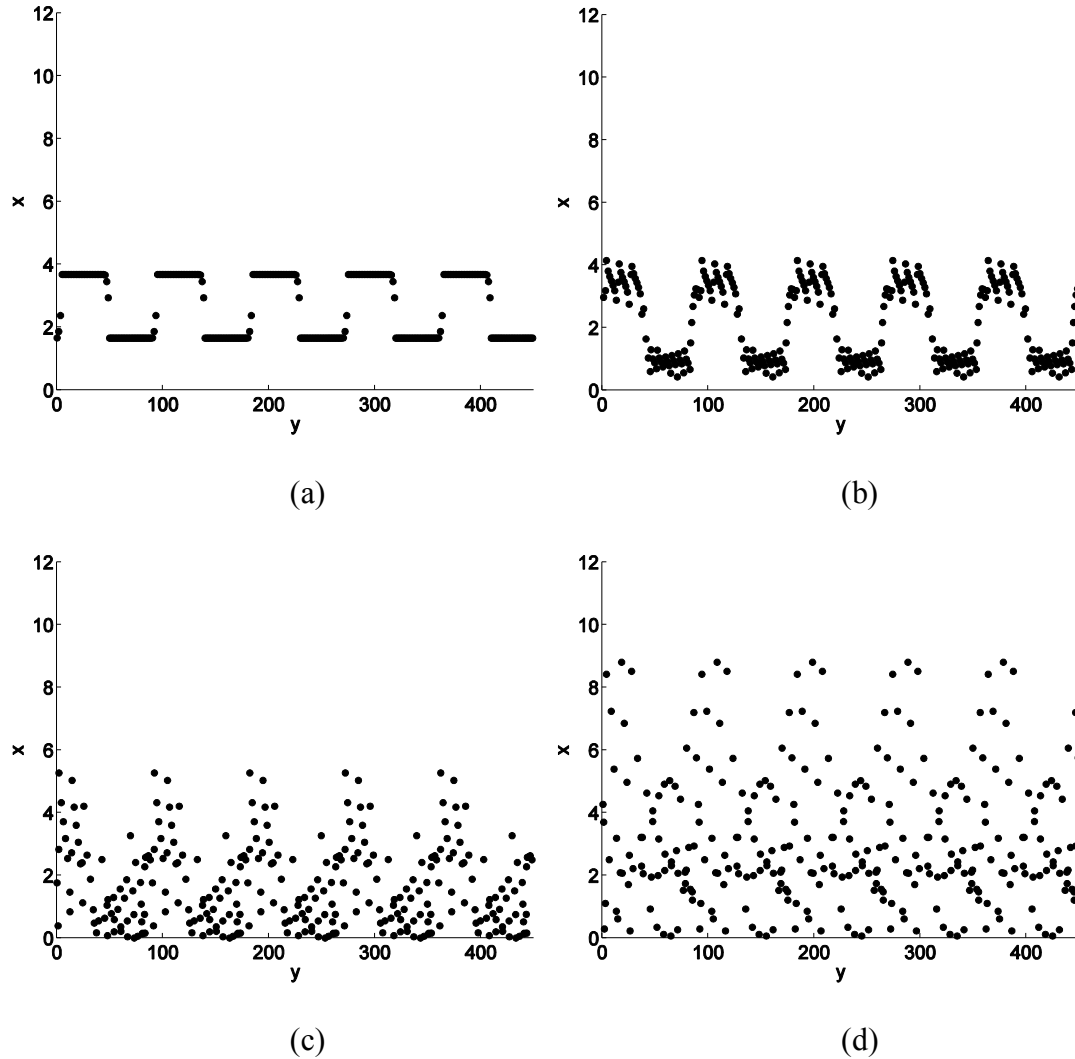


**Figure 2.7** The 5 electron bunches at (a)  $t = 4$  (about half cycloidal orbit after emission), (b)  $t = 73$ , (c)  $t = 454$  (after one re-circulation around the cathode), and (d)  $t = 1314$  (after 3 revolutions around the cathode).

The rapid startup with the periodic magnetic perturbation in a magnetron is hardly surprising, because the periodic magnetic field amounts to prebunching of the “beam”, and such prebunching is almost instantaneous ( $\sim$  half cycloidal period as in Figure 2.7(a)). The particle-in-cell simulations, done by Michael Jones [Jon04a] and by John Luginsland [Lug04], of magnetically primed magnetrons confirmed this effect. In addition to beam prebunching, it should be stressed that electron spokes are formed

*naturally* as a result of the radial migration, aided by a parametric instability that results from the periodic magnetic field. While the well-known RF self-focusing effect of the pi-mode is the reason for the spoke formation for the unprimed magnetron (see, e.g., [Lau87]), here, the spokes are a natural product of the static periodic magnetic field that are formed *kinematically* within a couple electron recirculation times. The initial five spokes, the rapid radial migration, and the intrinsic five-fold symmetry (in magnetic priming) in the electron dynamics speed up the excitation of the pi-mode (that needs five electron spokes), whose presence then reinforces the spoke formation through the usual phase-focusing mechanism that is unique to the magnetron geometry [Lau87]. The features were qualitatively revealed in the oven magnetron simulation reported in [Lug04]. One might also wonder if the additional migration of the electrons toward the anode, as a result of the periodic magnetic perturbations, is related to the impedance reduction that is observed in the low noise magnetron [Nec05b]. The single-particle phenomena studied here are central to the migration of the charge, as significant radial motion in simulations is shown both with 3-D realistic magnetic fields [Lug04] (with azimuthal magnetic perturbations that include radial components in the magnetic field), and with the two-dimensional (2-D) idealized perturbation fields (without a radial component of the magnetic field [Jon04a]), even in smooth bore geometry.

## 2.4 REMARKS

In summary, for magnetic priming strength  $\alpha$  between 0.1 and 0.5, the fast prebunching on the order of the Larmor period, as illustrated in Figure 2.7(a), and the five-fold symmetry in electron dynamics have been observed, as expected, when five

magnetic field periods are imposed. For  $\alpha$  between 0.1 and 0.5, as seen in Figure 2.5, electron maximum excursion into the crossed-field gap was greater than 3 (when the magnetic field is constant, the maximum excursion of electron is 2). Therefore, according to our model, not only fast prebunching and a five fold symmetry in electron dynamics, but also at least 50% expansion in electron maximum excursion has been achieved by imposing the azimuthally varying axial magnetic field, for every  $\alpha$  studied here.

For certain bands of values of  $\alpha$ , the electron maximum excursion increases dramatically, which is a key signature of a parametric instability. Equation (2.7) is the well-known relation for the occurrence of parametric instability. We emphasize that this parametric instability is orbital in nature, and does not involve collective effects. It connects the three characteristic frequencies of our model: the electron cyclotron frequencies corresponding to the maximum and the minimum magnetic fields, and the frequency associated with the spatial periodicity in the periodic magnetic field. A small variation in the periodicity of our model (e.g. through a small variation in the DC electric field) does not essentially change the effects of parametric instability, in spite of the sensitivity in certain orbits, as shown in the  $\lambda = 90.2$  case in Figure 2.4 in comparison with the  $\lambda = 90$  case in Figure 2.2. Calculations have been performed for more drastic changes. For the  $\lambda = 45$  case, the parametric instability relationship (2.7) that characterizes the peaks for maximum electron excursion is again recovered. Our calculations show (see Equation (2.7)) that a change in parameters would simply bring a change in the positions of peaks in electron maximum excursion.

It is more difficult to assess to what extent the modified orbits by the periodic magnetic field, in particular the radial ( $x$ ) migration of the electrons, contribute to the

experimentally observed low noise behavior [Nec03a, Nec04, Nec05a, Nec05b]. In previous experiments [Bro95a, Bro95b, Gil05] it has been suggested that if “excess electrons” are removed from the cathode region (demonstrated by turning off the heater after the oven magnetron is running), noise is considerably reduced [Jon04a, Sal95]. It would then be tempting to speculate that the radial ( $x$ ) migration studied here could be responsible for sending the “excess electrons” towards the anode. There are a few caveats, however [Nec05c].

- 1) After the rf mode is excited, the significant RF electric field ( $E_{RF}$ , which we ignored) produces an  $E_{RF} \times B$  drift which could speed up or take over the radial migration initiated by the periodic magnetic field.
- 2) An azimuthally varying axial magnetic field necessarily produces a radial component along the field line. This radial component of the magnetic field (which we have also ignored) may also effectively remove the electrons from the cathode to the anode.
- 3) The periodic magnetic field modeled by (2.1) yields a gradient B drift velocity in the  $x$ -direction. Of course, in our *numerical* calculation of the orbit such as those shown in Figure 2.2 – Figure 2.4, this gradient drift has been fully accounted for. This gradient drift does not seem to be an important factor, however.
- 4) After a few recirculation times, the gap is filled with the maximum amount of charge that it can hold (of order  $CV$  where  $C$  is the capacitance and  $V$  is the gap voltage [Ums05]). In this case, the most natural state of electron flows in a crossed-field gap is no longer the cycloidal flow that is studied here.

Instead, the flow will almost invariably be the Brillouin flow superimposed upon some turbulent background and electron spokes [Chr96, Pal80]. The orbital pictures will be drastically different. We should also stress that the Brillouin flow is consistent with space-charge limited emission in that the electric field is driven to zero on the cathode surface. Hence, the role of space charge and emission physics in the parametric instability is an area that requires further study.

Identifying the physical reasons for the low noise behavior observed in magnetron experiments has always been a difficult problem [Bro95a, Bro95b, Gil05, Lau95, Ose95a, Ose95b, Sal95]. Even to this day, particle codes remain poorly equipped to simulate noise in any realistic crossed-field device. Noise at 90 dB below the carrier, and within a fraction of a percent from the center frequency, are easily masked by numerical noise. This intrinsic difficulty is compounded by the incompleteness in the simulation models performed to date, such as the neglect of the ions [Yam87] and of the heater conditions [Bro95a, Bro95b] both are known to significantly affect magnetron noise. Some of these difficulties were addressed in [Lau95].

In spite of these difficulties, from a single particle orbit theory developed in a nonresonant structure, radial migration, parametric instability, and rapid formation of electron spokes due to kinematic bunching, all caused by the periodic magnetic field, conclusively point to the rapid startup observed in oven magnetrons with magnetic priming. These effects also give some indication to noise reduction, but this latter aspect is far from being settled.

Finally, we remark that, for rapid startup in a  $N$ -cavity magnetron operating in the pi-mode, not only a  $N/2$  azimuthal symmetry in magnetic field (magnetic priming), but also the use of a cathode with  $N/2$  azimuthal emitting regions gives excellent results. The technique is known as cathode priming [Jon04c, Nec03b]. The cathode priming technique was implemented at University of Michigan [Jon04b] for rapid startup and rapid mode locking of relativistic magnetrons. To cathode-prime a six-cavity relativistic magnetron, three azimuthally periodic, emitting regions are introduced around the cathode. Thus, a three-fold symmetry in the electron bunches, which is a prerequisite of the pi-mode, is immediately formed from the beginning. Such a cathode has been fabricated by ablating a pattern on the cathode by a KrF laser [Jon04b]; simulations [Jon04c] have shown that cathode priming results give about the same degree of fast startup as magnetic priming. Again the role of emission physics is an area of active study here as the cathode priming has been performed with explosive emission cold cathodes in relativistic magnetrons. Another form of cathode priming is to use  $N/2$  isolated discrete cathodes in an  $N$ -cavity magnetron [Jon05b, Fuk05, Nec03b]. Investigation of thermionic cathodes based on the same concept of geometric emission control, and impact on noise reduction are also interesting topics of study.

## CHAPTER 3

# MODELING AND COMPARISON WITH EXPERIMENTS OF MAGNETRON INJECTION LOCKING

### 3.1 INTRODUCTION

Phase-locking is utilized today in many important applications, ranging from small scale devices such as cardiac pacemakers [Pik01] to large scale devices such as radar [Yor98, Ace07]. In the development of high power microwave sources, phase-locking of relativistic magnetrons has been extensively studied [Ben89, Che90a, Che90b, Che91, Joh90, Lev90, Lev91, Nec03c, Sze92, Whi06, Woo89]. Some of these experiments were designed to combine the power of several relativistic magnetrons in a phase-locked array [Lev90, Lev91]. A more recent experiment used a lower power but more stable magnetron to control a high power relativistic magnetron that exhibits mode-competition [Whi06]. Performance of the pulsed relativistic magnetrons could improve if priming by an external signal exclusively excites the desired mode, usually the pi-mode. Recently, interest in phase-locking of non-relativistic magnetrons was renewed due to its possible application in the Solar Power Satellite (SPS) [Ose02], among others. The availability, efficiency, low-cost, size, ruggedness, and reliability of the oven magnetrons make them very attractive as a frequency injection-locked amplifier for the SPS [Bro88]. There are other recent applications.

Here, we present the theory and experiments on frequency locking using two continuous wave (CW) oven magnetrons [Pen05]. The analytical model closely follows Chen [Che90a] who made use of the Adler's condition [Adl73] and the Van der Pol equation [Pol34], but included magnetron-specific growth-saturation characteristic [Sla51] and nonlinear frequency pulling effect [Wal89]. The latter is believed to be especially important for both high-power conventional and relativistic magnetrons. While Chen constructed the model for relativistic magnetrons, we adopt it for the CW kW oven magnetron experiments [Nec05b].

In Section 3.2, a general phase-locking theory for magnetron is presented [Pen05]. Both magnetron-specific effects mentioned above are included in the derivation. Numerical results with discussions on a low-power injection-locking application are presented in Section 3.3. Experimental injection-locking with CW oven magnetrons [Nec05b] are presented in Section 3.4 and Section 3.5. In Section 3.6, we compare the numerical and experimental results.

## **3.2 PHASE-LOCKING THEORY FOR MAGNETRON**

What sets magnetron apart from other types of oscillators is that the electrons are born and interact with both the DC and the RF electric fields inside a common resonant cavity. The single-mode equivalent-circuit model for magnetron shown in Figure 3.1 consists of: a) the resonant RLC circuit which represents the magnetron operating at a specific mode, b) the electronic conductance  $g$  and the electronic susceptance  $b$  which account for the DC-electron and RF-electron interactions inside the cavity, and c) the

load conductance  $G$  and the load susceptance  $B$  which represent the admittance looking into an external load [Che90a, Sla51].

Current conservation of the circuit in Figure 3.1 can be written as

$$-(g + jb)\tilde{V}_{rf} = \frac{\tilde{V}_{rf}}{R} + \frac{\tilde{V}_{rf}}{j\omega L} + j\omega C\tilde{V}_{rf} + C\omega_{0u} \frac{(G + jB)}{Q_{ext}}\tilde{V}_{rf}, \quad (3.1)$$

where  $\omega_{0u} = (LC)^{-1/2}$  is the resonant mode frequency of the unloaded magnetron,  $Q_{ext}$  is the quality factor including the external load, and  $\tilde{V}_{rf}$  is the output RF voltage containing both fast and slow temporal components. The fast temporal component of  $\tilde{V}_{rf}$  has  $e^{j\omega t}$  dependence so that  $\tilde{V}_{rf} = V_{rf}(t)\cos(\omega t)$ , where  $V_{rf}(t)$  is slowly varying with a time-rate much smaller than  $\omega$ . For magnetrons,  $g$  and  $b$  have been suggested [Che90a, Sla51] to obey the relations  $g = -(1/R)(V_{dc}/V_{rf} - 1)$  and  $b = b_0 + g \tan \alpha$ , where  $V_{dc}$  is the DC voltage across the A-K gap,  $b_0$  is a constant, and  $\alpha$  is known as the frequency pushing parameter which is typically on the order of unity. Figure 3.2 qualitatively shows  $-g$  and  $-b$  as a function of  $V_{rf}$  [Sla51]. In this model, the negative slope of  $-g$  is responsible for the magnetron growth and saturation characteristics.

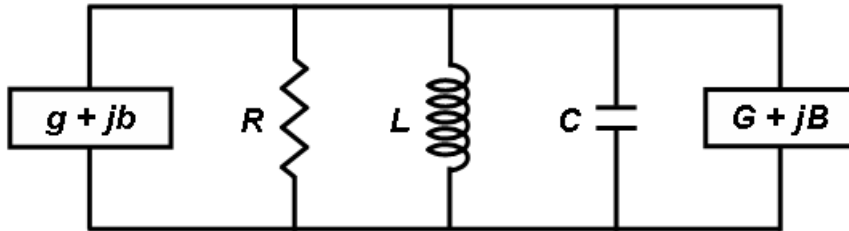


**Figure 3.1** The circuit model representing a magnetron that operates at a specific mode.

Steady-state analytic solutions of (3.1) can be obtained by assuming that  $V_{rf}$  is a constant in time, separating the equation into real and imaginary parts, and solving for  $V_{rf}$  and  $\omega$ , which is real. The normalized results then are [Che90a]

$$V_{rf, sat} = \frac{Q_L}{Q_L + Q_0} \quad (3.2a)$$

$$\omega_{sat} \equiv \omega' = \sqrt{1 - \frac{b_0}{Q_0} - \frac{B}{Q_{ext}} - \frac{\tan \alpha}{Q_L}} \quad (3.2b)$$

where  $1/Q_L = 1/Q_0 + G/Q_{ext}$  and  $Q_0 = \omega_{0u} RC$ . In deriving (3.2a) and (3.2b), the voltage is normalized by  $V_{dc}$ , time by  $1/\omega_{0u}$ , frequency by  $\omega_{0u}$ , and admittance by  $1/R$ .

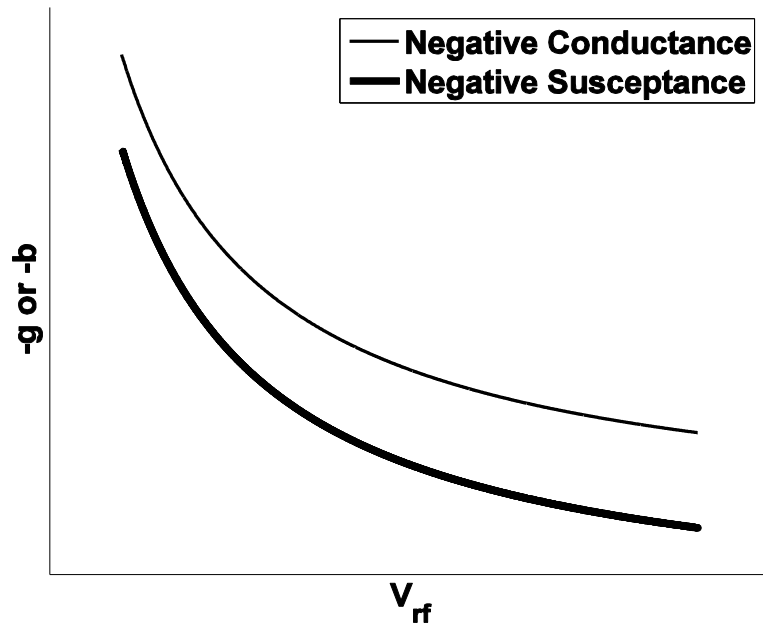


**Figure 3.2** Magnetron electronic admittance  $g$  and electronic susceptance  $b$  as a function of  $V_{rf}$ .

These normalizations will be used hereafter unless otherwise specified. For simplicity,  $\omega/\omega_{0u}$  is also assumed to be roughly unity. The details of the derivation along with the approximate temporal solution of  $V_{rf}$  can be found in Chen [Che90a].

When an external source of current  $\tilde{i}_1$  and voltage  $\tilde{V}_1$  is applied to drive the magnetron, the load admittance  $Y_{load}$  is modified accordingly [Sla51]:

$$Y_{load} = \frac{\tilde{i}_{rf} + \tilde{i}_1}{\tilde{V}_{rf} + \tilde{V}_1}, \quad (3.3)$$

where  $\tilde{i}_{rf}$  and  $\tilde{V}_{rf}$  are respectively the complex amplitudes of the RF current and the RF voltage delivered to the magnetron at its plane of reference. For convenience of notation, we will assume that the magnetron is driven by an external current source, and let  $\tilde{V}_1 = 0$ .

(The last expression on the right side of (3.4a) below will still be valid even when  $\tilde{V}_1$  has a non-zero value. Equation (3.4b) needs to be modified accordingly [Sla51], in which case  $\rho$  still measures the amplitude of the external signal relative to the RF signals.)

Equation (3.3) then reads

$$Y_{load} = \frac{\tilde{i}_{rf}}{\tilde{V}_{rf}} + \frac{\tilde{i}_1}{\tilde{V}_{rf}} = (G + iB) + \rho e^{j\theta}, \quad (3.4a)$$

where

$$\rho = i_1 / V_{rf}, \quad (3.4b)$$

and  $\theta$  is the relative phase difference between the phase of the external driving signal and the phase of the RF output. Specifically, if the phase of the external driving signal is  $\Phi_1 = \omega_1 t$ , the phase of the output signal would be  $\Phi_0 = \omega_1 t - \theta$ . Current conservation in the presence of the external driving signal then yields

$$-(g + jb)\tilde{V}_{rf} = \frac{\tilde{V}_{rf}}{R} + \frac{\tilde{V}_{rf}}{j\omega L} + j\omega C\tilde{V}_{rf} + C\omega_0 \frac{(G + jB) + \rho e^{j\theta}}{Q_{ext}} \tilde{V}_{rf}, \quad (3.5)$$

where  $\tilde{V}_{rf}$  is now of the form  $\tilde{V}_{rf} = V_{rf}(t)\cos(\omega_1 t - \theta(t))$ .

By allowing both  $V_{rf}$  and  $\theta$  to slowly vary in time, Equation (3.5) can be decoupled into two normalized first-order slowly time-varying equations [Che90a]:

$$\frac{d\theta}{dt} + \omega_0 - \omega_1 = \frac{\rho}{2Q_{ext}} \sin \theta \quad (3.6a)$$

$$\frac{1}{V_{rf}} \frac{dV_{rf}}{dt} + \frac{1}{Q_0} \left(1 - \frac{1}{V_{rf}}\right) = -\frac{\rho}{2Q_{ext}} \cos \theta, \quad (3.6b)$$

where the free-running magnetron oscillates at its normalized hot resonance frequency of  $\omega_0 = 1$ . The RF voltage,  $V_{rf}$ , in (3.6a) and (3.6b) has been rescaled so that the undriven value at saturation is unity. Time  $t$  has also been rescaled with respect to  $\omega_0 = 1$ . Since  $\rho$  depends on  $V_{rf}$  as suggested by (3.4b), these coupled equations govern the amplitude and phase evolution during the lock-in process. The locking condition can be analytically solved from (3.6a) by setting  $d\theta/dt = 0$ . This gives

$$1 - \omega_1 = \frac{\rho}{2Q_{ext}} \sin \theta \quad (3.7)$$

from which we obtain, as  $|\sin \theta| \leq 1$ ,

$$2Q_{ext}|1 - \omega_1| \leq \rho, \quad (3.8)$$

which is the well-known Adler's condition [Adl73]. The phase shift near locking can be obtained by pretending that  $\rho = \text{constant}$ , which is a good approximation, and rewriting (3.6a) as

$$\frac{d\theta}{dt} = \frac{\rho}{2Q_{ext}} \sin \theta + (\omega_1 - 1), \quad (3.9)$$

whose explicit solution is [Sla51]

$$\tan\left(\frac{\theta}{2}\right) = \frac{A}{B} - F \sqrt{\left(\frac{A}{B}\right)^2 - 1}, \quad (3.10)$$

where

$$A = \frac{\rho}{2Q_{ext}}, \quad (3.11a)$$

$$B = 1 - \omega_1, \quad (3.11b)$$

$$D = \sqrt{A^2 - B^2}, \quad (3.11c)$$

and

$$F = \frac{1 + e^{D(t-t_0)}}{1 - e^{D(t-t_0)}}. \quad (3.11d)$$

There are three regions of interest:

- (i)  $D$  is real. In this case, Adler's condition (3.8) is satisfied and the magnetron is phase-locked to the external source. As time increases,  $F$  approaches  $-1$ , and  $\theta$  has a constant value which can be easily determined by solving (3.10). It can be shown that when (3.8) is marginally satisfied, the phase shift between the magnetron and the external source is  $n\pi + \pi/2$ , where  $n$  is an integer.
- (ii)  $D$  is small and imaginary. In this case, the magnetron is not phase-locked to the external source. We can write  $F = i \cot(|D|(t-t_0)/2)$  such that the right hand side of (3.10) becomes periodic with period  $2\pi/|D|$ .  $\theta$  is no longer a constant, but is a superposition between a linear function of time

and a function with periodicity  $2\pi/|D|$ . Therefore, sideband frequencies at integral multiples of  $|D|/2\pi$  can be expected in this case. As  $\rho$  increases, the periodicity becomes smaller, and the sidebands are expected to move closer to  $\omega_1$ .

- (iii)  $D$  is large and imaginary. In this case,  $B \gg A$ , and the right hand side of (3.10) becomes  $\cot(|D|(t-t_0)/2)$ . Thus,  $\theta$  becomes a linear function of time. The oscillating frequency of magnetron is therefore unaffected by the source frequency.

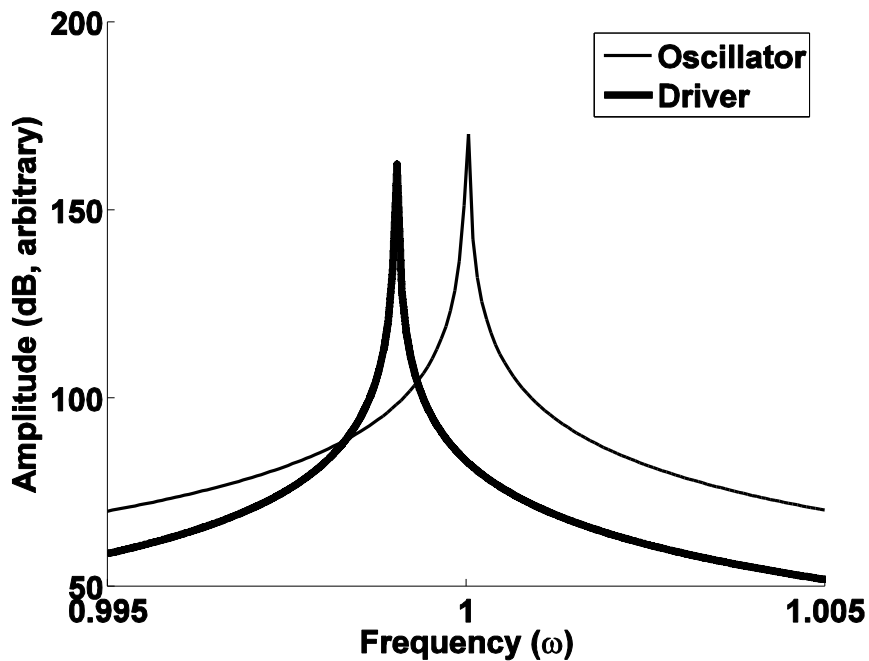


**Figure 3.3** Spectra of the free-running oscillator and the external driving signals.

### 3.3 NUMERICAL RESULTS OF PHASE LOCKING ANALYSES

Equations (3.6a) and (3.6b) can be numerically solved for  $V_{rf}$  and  $\theta$  using the Runge-Kutta method [Bog89, Dor80]. A MATLAB<sup>®</sup> algorithm [Mat94] was written to numerically solve (3.6a) and (3.6b) for  $V_{rf}$  and  $\theta$ . The external driving signal  $\rho$  is applied after a specific time, e.g., after the free-running signal saturates, to mimic the CW “injection locking” experiment. The time-domain output signal  $\tilde{V}_{rf}$  including both amplitude and phase dependence can then be reconstructed, and its power spectrum is analyzed using fast Fourier transform.

Figure 3.3 shows the power spectra of the free-running signal constructed by setting  $\rho = 0$  and  $Q_0 = 100$ , and using the initial conditions:  $V_{rf}(0) = 0.001$ ,  $dV_{rf}(0)/dt = 0$ ,  $\theta(0) = 0$ , and  $d\theta(0)/dt = 0$ . Also shown in Figure 3.3 is the spectrum of the drive signal that is to be applied after the free running signal reaches its steady state. The center frequency of the free-running signal is at  $\omega_0 = 1$ , and it is to be locked to the external driving signal at  $\omega_1 = 0.999$ . According to (3.8) and (3.4b), with the free-running  $V_{rf}$  normalized to unity, locking with these frequencies occurs when  $i_1/Q_{ext} \geq 0.002$ . Figures 3.4 and 3.5 show the power spectra of  $\tilde{V}_{rf}$  at various  $i_1/Q_{ext}$ . When  $i_1/Q_{ext}$  is much lower than 0.002 [Figure 3.4,  $i_1/Q_{ext} = 0.0008$  case], the magnetron frequency is unaffected by the driving frequency, and the power spectrum has a dominant peak at  $\omega_0 = 1$  as in the free-running case. Sidebands can be observed at multiple integers of 0.001, which is equivalent to the difference between  $\omega_0$  and  $\omega_1$ , away from the  $\omega_0 = 1$  peak. This is similar to the aforementioned case (ii) when  $D$  is

small and imaginary. As  $i_1/Q_{ext}$  approaches the locking criterion [Figure 3.5,  $i_1/Q_{ext} = 0.0019$  case], the sidebands become stronger while the dominant peak becomes smaller. The frequency separation between adjacent sidebands also becomes smaller. When locking occurs [Figure 3.5,  $i_1/Q_{ext} = 0.0026$  case], the sidebands disappear and the oscillator oscillates at the frequency centered around  $\omega_1$  as predicted by case (i) when  $D$  becomes real.

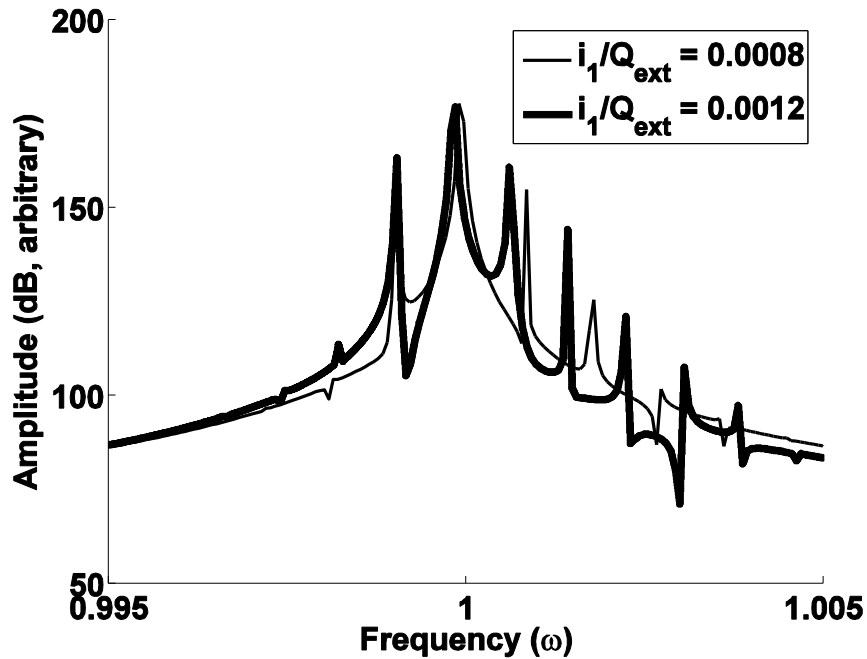


**Figure 3.4** Locking signal at  $i_1/Q_{ext} = 0.0008$  and  $0.0012$ . Locking occurs when  $i_1/Q_{ext} = 0.002$  according to the Adler's condition.

We have observed that phase-locking may occur even when the Adler's condition, Equation (3.8), is not met. In such cases, a closer examination of  $V_{rf}$  in time domain shows that  $V_{rf}$  violently fluctuates when the external driving signal is initially applied, before it settles into a new saturation level that is lower than the saturation level in the

free-running case. We suspect that the initial fluctuation allows phase-locking to occur at a drive level below the Adler's criterion. This interesting topic is, however, beyond the scope of this thesis.

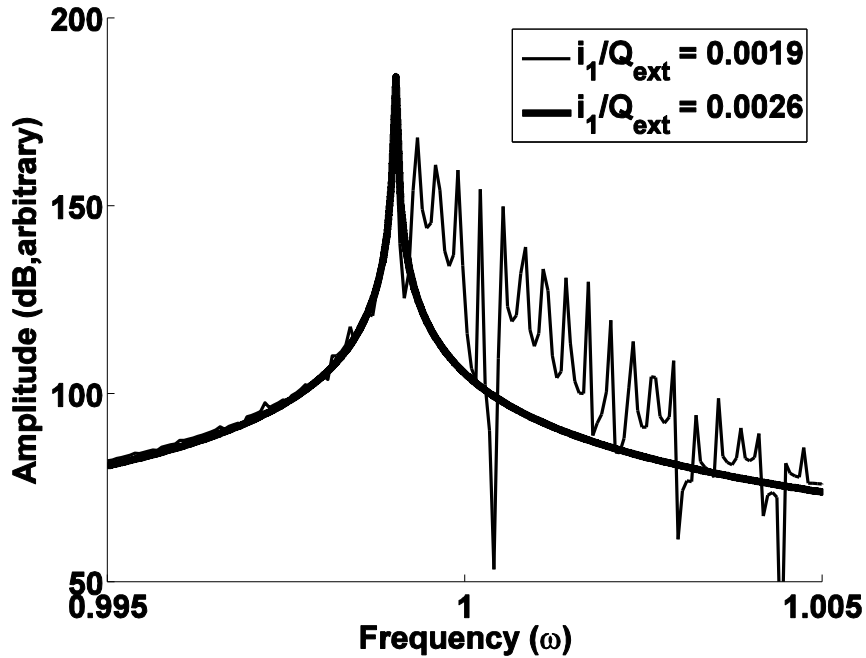


**Figure 3.5** Locking signal at  $i_1 / Q_{ext} = 0.0019$  and  $0.0026$ . Locking occurs when  $i_1 / Q_{ext} = 0.002$  according to the Adler's condition.

### 3.4 INJECTION LOCKING EXPERIMENTAL SETUP [Nec05b]

The experiments were performed by Neculaes [Nec05b]. For completeness and for ready comparison with the theoretical model, this section and the next include summary of his work. Two CW 2.45-GHz 800-W magnetrons are used by the microwave research group at the University of Michigan [Nec05b] to demonstrate phase-locking in reflection amplifier experiments. One magnetron functions as a driver and the other as a driven oscillator. The experimental configuration is shown in Figure 3.6. The

driver magnetron is manufactured by National Electronics, model SXRH (with ASTEX power supply, model S-1000i). The oscillator magnetron is manufactured by National Electronics, model HS (with ASTEX power supply, model S-1000). These ASTEX power supplies are very stable, and can deliver a well filtered DC voltage. Three waveguide circulators are used to separate the direct and the reflected power so that the two magnetrons are not mutually coupled. The majority of the microwave power produced by the driver magnetron is dissipated into a water load, while a controlled fraction is injected into the oscillator magnetron. A three-stub tuner is employed for the purpose of varying the amount of power injected into the oscillator without changing the injected frequency. Several 30 dB directional couplers are implemented in order to sample microwave signals for power measurement (with Agilent E4418B digital power meters) and spectrum measurements (with an Agilent 8564 EC spectrum analyzer). WR-284 waveguides (2.84 inches wide) have been used in experiments.

It should be mentioned that the ASTEX power supplies yield stable (in time) oven magnetron microwave spectra. The central peak in the microwave spectra (corresponding to the 2.45-GHz pi-mode oscillation) does not exhibit time jitter or amplitude modulation. This stability allows relatively accurate frequency and phase noise measurements. A 100-kHz resolution bandwidth was utilized in spectrum analyzer measurements.

Magnetron filament power is controlled automatically within the power supply for optimum operation at every power level. The only control offered by the ASTEX power supplies is the microwave power level. Peak frequency is directly proportional to the output power for both magnetrons. Previously, Brown [Bro88] used a frequency pulling

section to change the driver frequency; in our experiments the driver frequency change has been achieved by varying the output power of the driver magnetron.

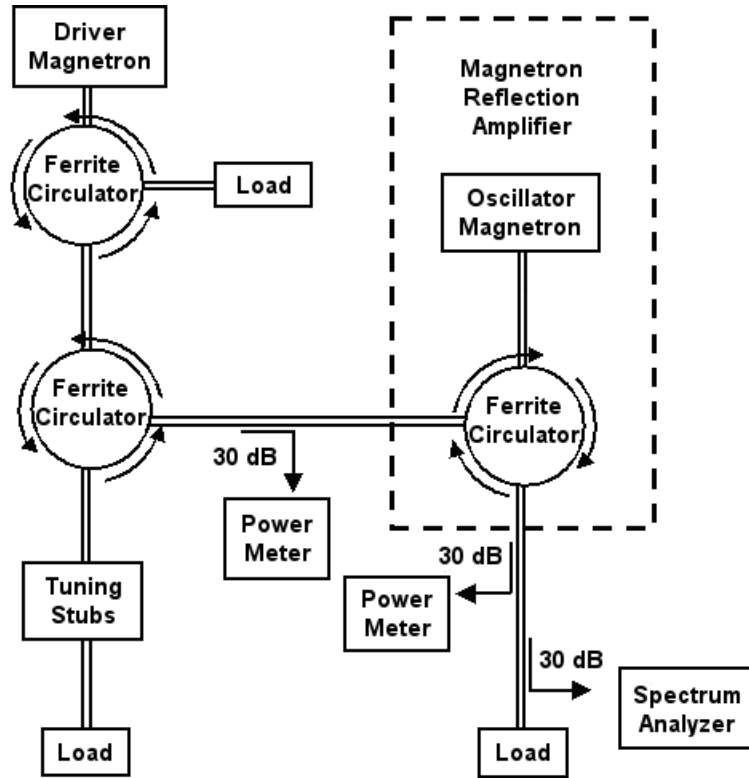


**Figure 3.6** The reflection amplifier setup for injection lock experiment [Nec05b].

### 3.5 EXPERIMENTAL RESULTS [Nec05b]

Initial experiments by Neculaes [Nec05b] show that the oscillator magnetron's peak frequency increases when the output power (current) increases as illustrated in Figure 3.7. It is found that this magnetron behavior can be altered by injecting an external signal to force the output frequency to remain relatively constant. At zero drive, as the free running oscillator output power increases from 200 W to 350 W, its peak frequency changes by 0.07%. When 16-W power from the driver is injected into the

oscillator, the peak frequency remains comparatively constant and locked to the driver frequency at 2.4478 GHz.

Further detailed experiments are performed to understand the physics of injection-locking. By fixing the driver output power, the driver frequency is maintained constant at 2.4482 GHz. The free-running oscillator produces 825 W of the microwave power ( $P_0$ ) with the frequency centered around  $\omega_0/2\pi = 2.4511$  GHz. Power spectra of the oscillator and the driver in free-running state are shown in Figure 3.8. For  $Q_{ext} \approx 250$ , Adler's condition gives the required injected (drive) power  $P_{drive}$  for phase-locking [Adl73]:

$$P_{drive} \geq P_0 \times Q_{ext}^2 \times \left( \frac{f_0 - f_1}{f_0} \right)^2 = 825 \times 250^2 \times \left( \frac{2.4511 - 2.4482}{2.4511} \right)^2 \approx 58 \text{ W.} \quad (3.12)$$

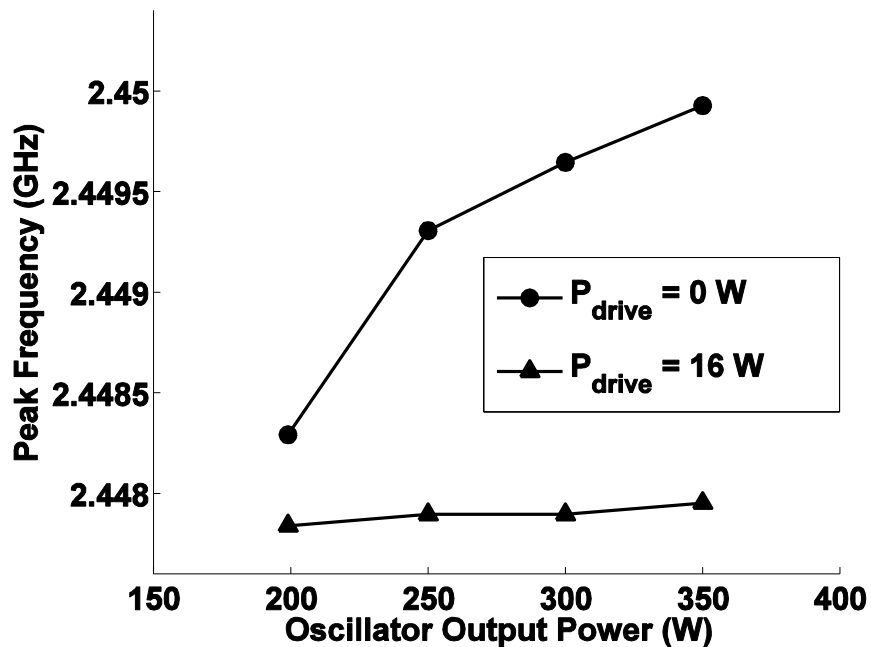


**Figure 3.7** Peak frequency dependence on the output power of the free running oscillator (zero drive power). With an external drive power at 16W, the oscillator frequency remains constant (locked) [Nec05b].

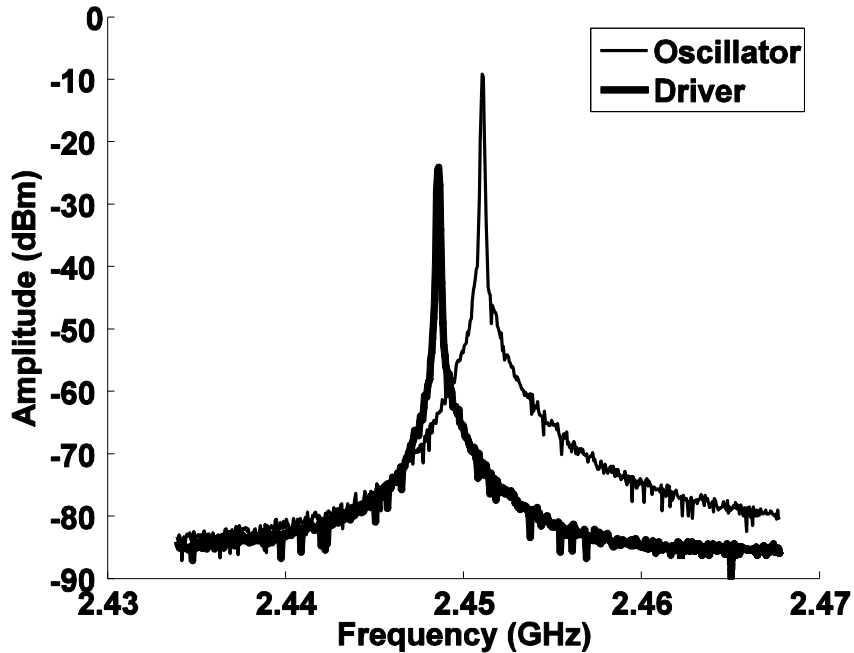


**Figure 3.8** Spectra of the oscillator and the driver in free running mode for the experiments performed to study the mechanism of injection locking (varied  $P_{drive}$ ).  $P_0 = 825$  W [Nec05b].

The injected power can be varied without changing the driver frequency by adjusting the (reflecting) three-stub tuner. Figures 3.9 and 3.10 present various stages of injection locking as the injected power is increased. For the injected power of 5 W, the spectrum already shows dramatic changes from the free-running state. While the main peak of the reflection amplifier spectrum has roughly the same frequency as the free-running oscillator magnetron, there are sidebands situated at multiples of 3 MHz, (6 MHz, 9 MHz, etc.) away from the carrier. These numbers correspond to the integer multiple of the frequency difference between the driver and the free-running oscillator. Therefore, even with 5-W injected power, the reflection amplifier shows the potential for injection locking.

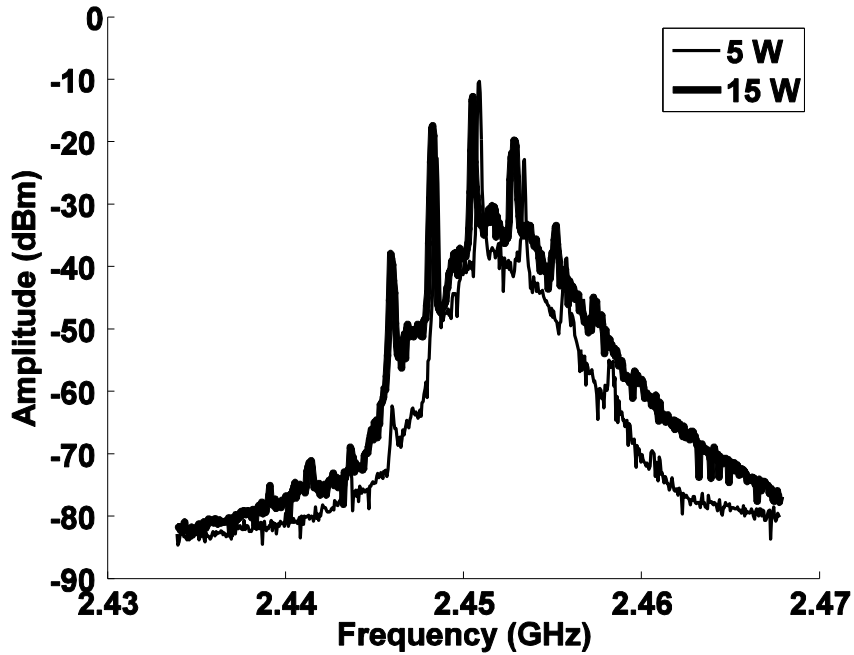


**Figure 3.9** Reflection amplifier microwave spectra when  $P_{drive}$  is set to 5 and 15 W. Locking occurs when  $P_{drive} > 58$  W according to Adler's Condition. [Nec05b]

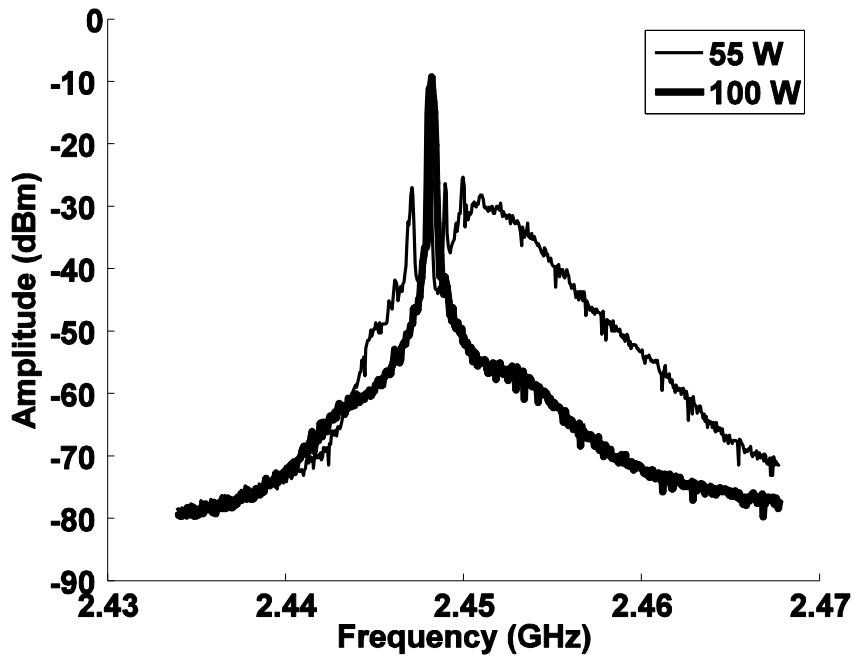


**Figure 3.10** Reflection amplifier microwave spectra when  $P_{drive}$  is set to 55 and 100 W. Locking occurs when  $P_{drive} > 58$  W according to Adler's Condition. [Nec05b]

As the injected power is increased to 15 W, the height of the main peak decreases while the secondary peaks, each 3 MHz from the carrier, gain their strength. This effect is significant, and one could predict from Figure 3.9 that the more power is injected in the oscillator, the stronger the peak at 2.4482 GHz would be. One can also observe that at 55-W injected power, slightly lower than the required locking power of 58 W predicted in (3.12), the highest peak in the reflection amplifier microwave spectrum is emitted near 2.4482 GHz, i.e., the frequency of the driver. The oscillator frequency is therefore partially locked to the driver frequency. Despite the fact that the emitted frequency has the desired value in this case, there exist some secondary peaks. There is also a large “bump”, at roughly 17 dB below the carrier, at frequencies above the carrier. These secondary peaks have been described and predicted by the aforementioned analytical model, specifically in case (ii) when  $D$  is small and imaginary. At 100-W injected power, however, all the secondary peaks disappear and the reflection amplifier frequency is completely locked at the driver frequency as shown in Figure 3.10, following the prediction in case (i) when  $D$  is real. Nevertheless, there still exist small plateaus on both sides of the main peak, which have not been predicted by the theory.

### **3.6 COMPARISON BETWEEN NUMERICAL CALCULATIONS AND EXPERIMENTAL RESULTS**

In both the numerical calculation (Figures 3.3, 3.4, and 3.5) and the experiment (Figures 3.8, 3.9, and 3.10), the frequency of the externally injected signal differs from the oscillator frequency by 0.1%. That is, the fractional frequency change was maintained a constant,

$$\left( \frac{f_0 - f_1}{f_0} \right) = 0.1\%$$

Frequency analyses of the oscillator output signals allow qualitative comparisons between the experimental data and the theoretical model in three regimes of phase-locking: no-locking, partial-locking, and full-locking. No-locking indicates that the oscillator frequency is slightly affected or unaffected by the driver frequency, and therefore continues to oscillate mainly at its free-running frequency. Partial-locking indicates that the oscillator tends to oscillate at the driver frequency while also still oscillating at its free-running frequency. Full-locking indicates that the oscillator fully oscillates at the driver frequency. In subsequent discussions, it is important to note that the locking frequency of the driver is lower than the free-running frequency of the oscillator, both in the experiment and the simulation. The predicted locking criterion is  $P_{drive} \geq 58$  W for the experiment, and  $i_1 / Q_{ext} \geq 0.002$  for the simulation.

The following phase-locking characteristics have been observed both in the injection-locking experiment (Figures 3.9 and 3.10), and in the simulation (Figures 3.4 and 3.5) based upon the presented theoretical model:

- 1) When  $P_{drive}$  and  $i_1 / Q_{ext}$  are substantially below the locking criterion (Figures 3.4 and 3.9): (a) the dominant peaks on all of the frequency spectra are emitted near the free-running oscillator frequency. No locking occurs and the oscillator mainly oscillates at its free-running frequency. In all cases, the strength of the dominant peaks is also lower than the strength of the free-running peaks in Figures 3.3 and 3.8. (b) Sidebands are observed above and below the dominant frequency peak. These sidebands are emitted at the

frequencies which differ from the frequency of the dominant peak roughly by multiple integers of the frequency difference between the free-running oscillator and the driver frequencies. Consequently, the first sideband below the main peak is emitted exactly at the driver frequency. The strength of the sidebands substantially reduces further away from the dominant peak. The reduction appears to be more prominent on the sidebands below the driver frequency, which is hardly surprising considering the free-running spectra in Figures 3.3 and 3.8.

- 2) As  $P_{drive}$  and  $i_1/Q_{ext}$  are closer to Adler's locking criterion (Figures 3.4 and 3.9): (a) the dominant peak and all sidebands above the driver frequency move toward the driver frequency, while the sidebands below the driver frequency stay at the same values. (b) The strength of the dominant frequency peak continuously subsides while the sidebands become stronger.
- 3) When  $P_{drive}$  and  $i_1/Q_{ext}$  are very close to the locking criterion (Figures 3.5 and 3.10), the sideband emitted at the driver frequency becomes the dominant peak. The oscillator frequency is partially locked to the driver frequency. The frequencies of the previous dominant peak and the other sidebands shift accordingly and cluster around the new dominant peak.
- 4) Full phase-locking is confirmed in both experiment and simulation when  $P_{drive}$  and  $i_1/Q_{ext}$  are above the Adler's criterion (Figures 3.5 and 3.10). All sidebands disappear leaving only the dominant peak emitted at the driver frequency. The strength of the peaks is comparable to that of the free-running oscillator peaks in Figures 3.3 and 3.8.

Another characteristic in which the injection locking experiment manifests, but has not been captured in the theoretical model, is the spectral plateaus around the phase-locked signal shown in Figure 3.10 when  $P_{drive} = 100$  W. It has been confirmed that the spectral plateaus continue to exist even at higher drive power.

On the other hand, the numerical simulation based on the theoretical model suggests that phase-locking can occur even when the Adler's locking criterion is not met. For a given drive power, this translates to some additional locking bandwidth.

It should be mentioned that although the discrepancies in the quantitative behaviors between the experimental and the simulation results may be attributed to the oversimplification of the model employed, some of them could be explained by the limitations of the spectrum analyzer used in the experiment [Nec05b, Pen05]. Such limitations include the finite sweep time and the limited frequency resolution, which could possibly explain the difference between the “bump” on the spectrum in Figure 3.10 when  $P_{drive} = 55$  W and the finite peaks on the spectrum in Figure 3.5 when  $i_1 / Q_{ext} = 0.0019$ .

### 3.7 LOCKING TIME

Injection locking does not occur instantly. The time-domain solutions obtained by numerical integration of the phase and the amplitude equations (3.6a) and (3.6b) allow estimation of the locking time required when Adler's criterion is satisfied. Such solutions are shown in Figures 3.11(a) and 3.11(b) for various  $i_1 / Q_{ext}$  and  $Q_0$ . Here, the injected signal is applied after the free-running oscillator signal fully oscillates. The amplitude of

the output signal initially jumps, as the injected signal is applied, before it settles into a saturation value (when Adler's condition is marginally satisfied, that value is unity). Similarly, there is a transition period, or the locking time, before the phase difference  $\theta$  saturates.

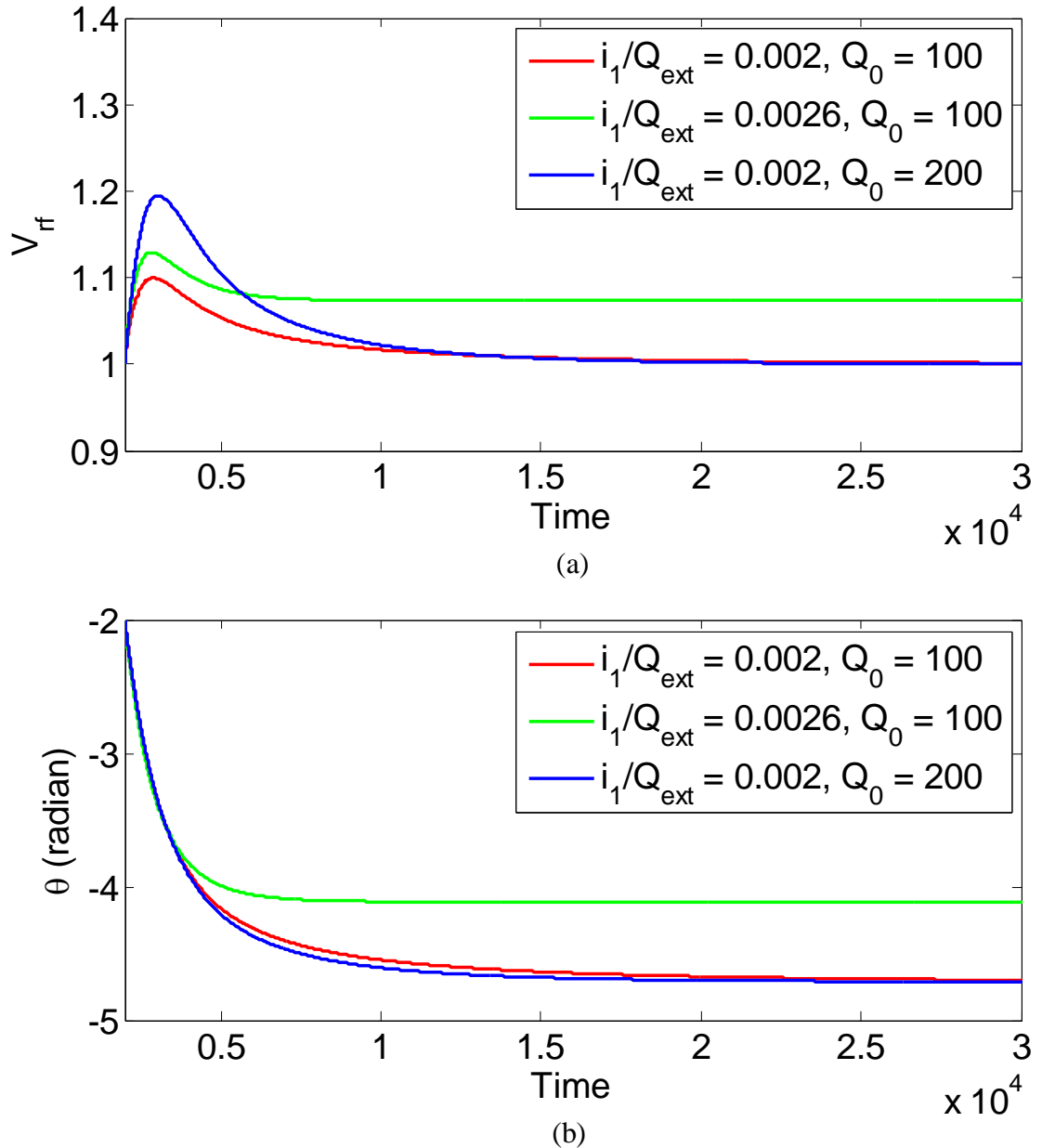


**Figure 3.11** (a) Amplitude and (b) phase solutions of the output signal in time domain. The frequency difference between the injected signal and the oscillator signal is 0.001 so that Adler's condition is satisfied when  $i_1/Q_{\text{ext}} \geq 0.002$ .

For a similar injected signal  $i_1/Q_{ext}$ , the locking time varies as a function of  $Q_0$ . In Figure 3.11(b), the phase difference  $\theta$  at saturation between the injected and the oscillating signals when  $i_1/Q_{ext} = 0.002$  is  $-(\pi + \pi/2)$  or  $-4.7123$  rad. Figure 3.12 shows the locking time for  $\theta$  to reach 99% of its saturation value as a function of  $Q_0$ . This locking time is very important to locking at high power as such operation commonly utilizes short pulse magnetron instead of continuous-wave magnetron.

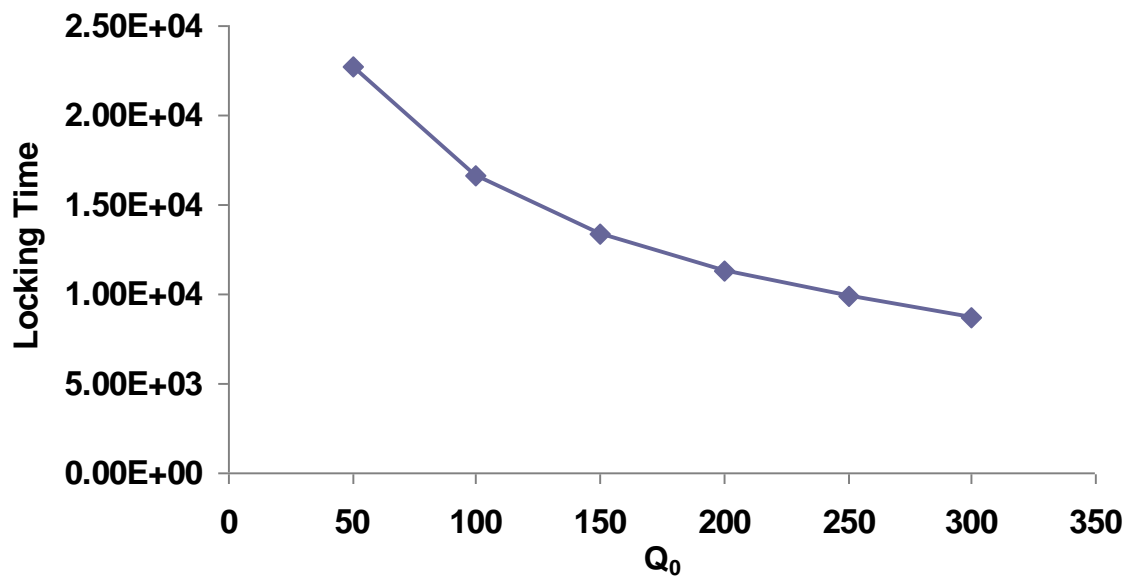


**Figure 3.12** The amount of time that the phase difference between the injected and the oscillator signal takes to reach 99% of its saturation value after the injected signal is applied, i.e., locking time.

In summary, although there exists no analytical theory that is capable of accurately predicting magnetron behavior, the circuit model introduced here is shown to be able to qualitatively recover the injection-locking characteristics observed in the experiment performed with the CW oven magnetron reflection amplifier. Locking time has also been considered. This circuit model was originally developed for relativistic magnetron.

# **CHAPTER 4**

## **EFFECTS OF FREQUENCY CHIRPING ON MAGNETRON INJECTION LOCKING**

### **4.1 INTRODUCTION**

The injection locking model and the numerical simulations given in Chapter 3 assume that the frequencies of both the free-running and the injected signals are constant. In general, however, both frequencies can vary in time, resulting in additional time-varying components in the amplitude and the phase equations, i.e., Equations (3.6a) and (3.6b). These time-varying components may have magnitudes which are comparable to the existing terms in the equations, causing alteration in the injection locking behavior of the system. Such time-varying terms in the free-running oscillator may come from the droops in voltage pulse in the cases of relativistic magnetron and high-power conventional magnetron subjected to frequency pulling. Also of interest is when the injection frequency can be swept in time. The latter could be utilized for frequency search when the oscillator frequency is not known. In this chapter, effects of time-varying frequencies on the injection locking behavior are explored.

## 4.2 INJECTION LOCKING FORMULATIONS IN THE PRESENCE OF FREQUENCY CHIRP

We shall first consider the case that the frequency of the injected signal,  $\omega_1$ , is allowed to vary in time while the frequency of the free-running signal,  $\omega_0$ , remains fixed at  $\omega_0 = 1$  [Equation (3.6a)]. For simplicity, we shall also consider a linear frequency chirp case in which the injected frequency  $\omega_1$  can be written as

$$\omega_1(t) = \omega_{10} + (t - t_s) \frac{d\omega_1}{dt}, \quad (4.1)$$

where  $t_s$  is the time that the frequency starts to chirp, and  $d\omega_1/dt$  is the chirping rate, which is zero when  $t < t_s$  and is assumed to be constant when  $t \geq t_s$ . In addition, this chirping rate is assumed to be slow in comparison with  $\omega_{10}$ . Figure 4.1 shows an example of the injected frequency profile, using the same normalization as in Chapter 3.

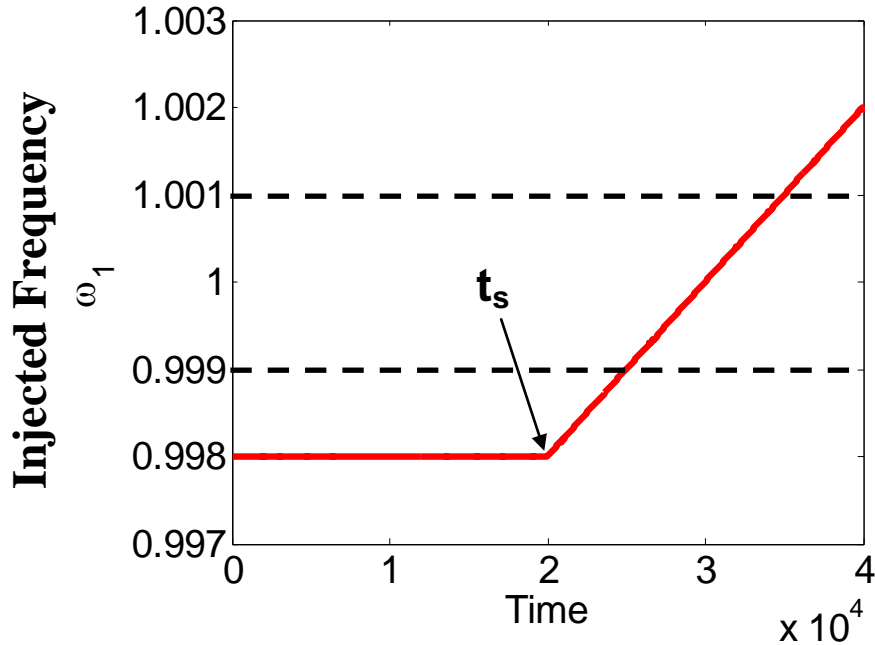


**Figure 4.1** Example of the injected frequency profile. Here,  $d\omega_1/dt = 2 \times 10^{-7}$ . The dotted lines show the boundaries of the locking range according to Adler's condition.

The output signal  $\tilde{V}_{rf}$  can be modified to take into account the time-varying injected frequency as followed:  $\tilde{V}_{rf} = V_{rf}(t)\cos\left(\int_0^t \omega_1(t)dt - \theta(t)\right)$ . Upon solving (3.5)

using the modified  $\tilde{V}_{rf}$ , the phase and the amplitude equations read, respectively,

$$\frac{d\theta}{dt} + 1 - \omega_{10} - (t - t_s) \frac{d\omega_1}{dt} = \frac{\rho}{2Q_{ext}} \sin \theta \quad (4.2a)$$

$$\frac{1}{V_{rf}} \frac{dV_{rf}}{dt} + \frac{1}{2\omega_{10}} \frac{d\omega_1}{dt} + \frac{1}{Q_0} \left(1 - \frac{1}{V_{rf}}\right) = -\frac{\rho}{2Q_{ext}} \cos \theta. \quad (4.2b)$$

Equation (4.2a) suggests that complete locking cannot occur because  $d\theta/dt$  cannot be zero, i.e.,  $\theta = \text{constant}$  is no longer a solution to (4.2a) if  $d\omega_1/dt \neq 0$ . When  $d\omega_1/dt$  is non-zero,  $\theta$  continuously varies in time. Nevertheless, when the Adler's condition,

$$2Q_{ext}|1 - \omega_1(t)| \leq \rho, \quad (4.3)$$

is satisfied,  $\theta$  is roughly a constant,  $d\theta/dt$  is small, and the output frequency tracks the injected frequency

$$\omega(t) = \omega_1(t) - \frac{d\theta(t)}{dt}. \quad (4.4)$$

The bounds of (4.3) are shown in Figure 4.1 by the dotted lines, i.e., between  $t = 2.5 \times 10^4$  and  $t = 3.5 \times 10^4$ , for  $\rho/2Q_{ext} = 0.001$ .

The value of  $d\theta/dt$  when (4.3) is satisfied can be estimated by recognizing that, to the lowest order, (4.2a) gives [see also Equation (3.7)]

$$\cos^2(\theta) = 1 - \sin^2(\theta) = 1 - \left[ \frac{1 - \omega_1(t)}{\rho/2Q_{ext}} \right]^2, \quad (4.5)$$

upon ignoring the  $d\theta/dt$  term in the LHS of (4.2a). Then, differentiation of (4.5) yield the approximate drift rate in the relative phase

$$\frac{d\theta(t)}{dt} = \frac{\frac{d\omega_1(t)}{dt}}{\sqrt{\left(\frac{\rho}{2Q_{ext}}\right)^2 - (1 - \omega_1(t))^2}}, \quad (4.6)$$

which is given in terms of the chirping rate and the Adler's condition that is exhibited in the denominator in the RHS of (4.6). We shall compare (4.6) with a direct integration of (4.2a) and (4.2b) [Figure 4.4 below].

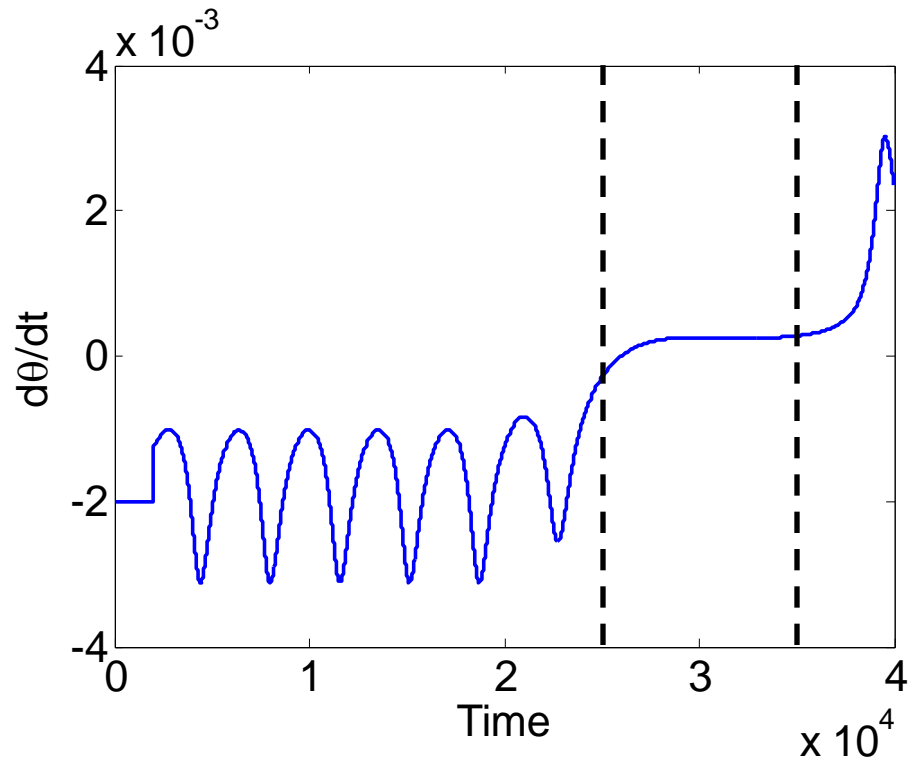


**Figure 4.2** Differential phase shift of the output signal. The injected signal is not applied until  $t = 2000$ . The dotted lines show the boundaries of the locking range according to Adler's condition.

Equations (4.2a) and (4.2b) can be integrated numerically for the injected frequency profile of Figure 4.1. Recall from Chapter 3 that for  $i_1 / Q_{ext} = 0.002$ , injection

locking occur when the injected frequency is between 0.999 and 1.001 [Figure 4.1]. Within this frequency range, Equation (4.3) is satisfied and one can expect the output frequency to track the injected frequency. Figures 4.2 and 4.3 respectively show the numerical results of the differential phase  $d\theta/dt$  and the output frequency in comparison to the injected frequency. The injected signal is not applied until  $t = 2000$  [Figure 4.2]. Since the injected frequency is initially outside the locking range, locking does not occur for  $t < 2.5 \times 10^4$ . Both  $d\theta/dt$  and the output frequency oscillate at a period which shows the beating between the free-running and the injected frequencies [Figure 4.3]. This is also reflected in Figure 3.4 outside of the locking range. For the amplitude solution, refer to Equations (3.10) to (3.11d) and the discussion on various regions of interest in Chapter 3.

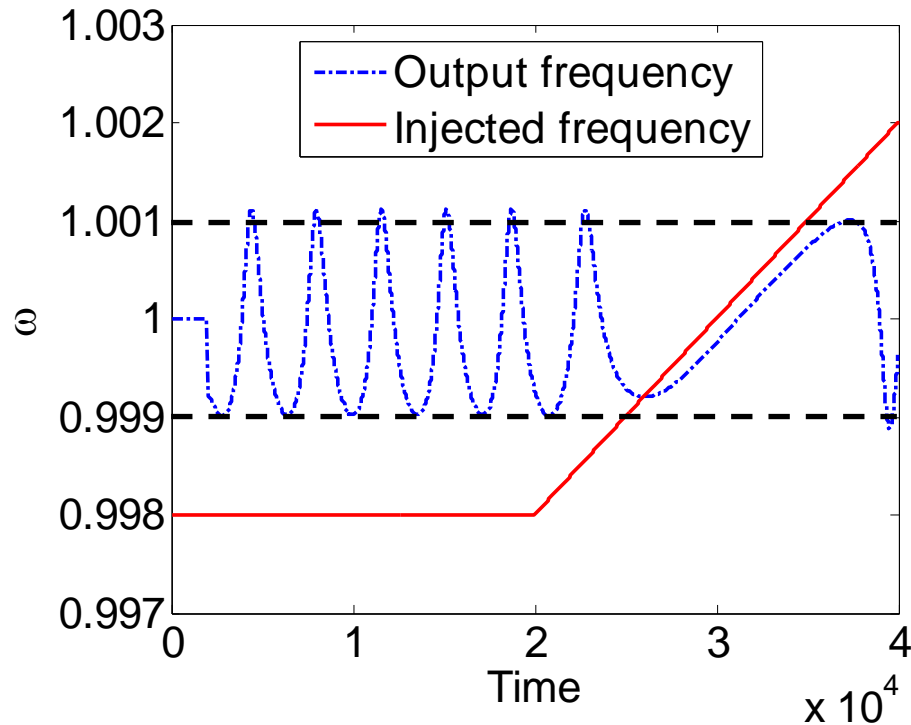


**Figure 4.3** Output frequency (dotted) in comparison to the injected frequency (solid). The dotted lines show the boundaries of the locking range according to Adler's condition.

Once the injected frequency starts to increase between 0.999 and 1.001,  $d\theta/dt$  becomes “relatively” constant and close to zero [Figure 4.4]. The output frequency starts to track the injected frequency until the injected frequency becomes greater than 1.001 [Figure 4.3]. Figure 4.4 shows the comparison between the calculated value of  $d\theta/dt$  and the value estimated by (4.6) for  $2.5 \times 10^4 < t < 3.5 \times 10^4$ , during which the instantaneous Adler’s condition (4.3) is satisfied. This figure shows that the slight drift in the phase ( $d\theta/dt \approx 0$ ) is given quite accurately by the approximate equation (4.6) when the Adler’s condition is roughly satisfied.

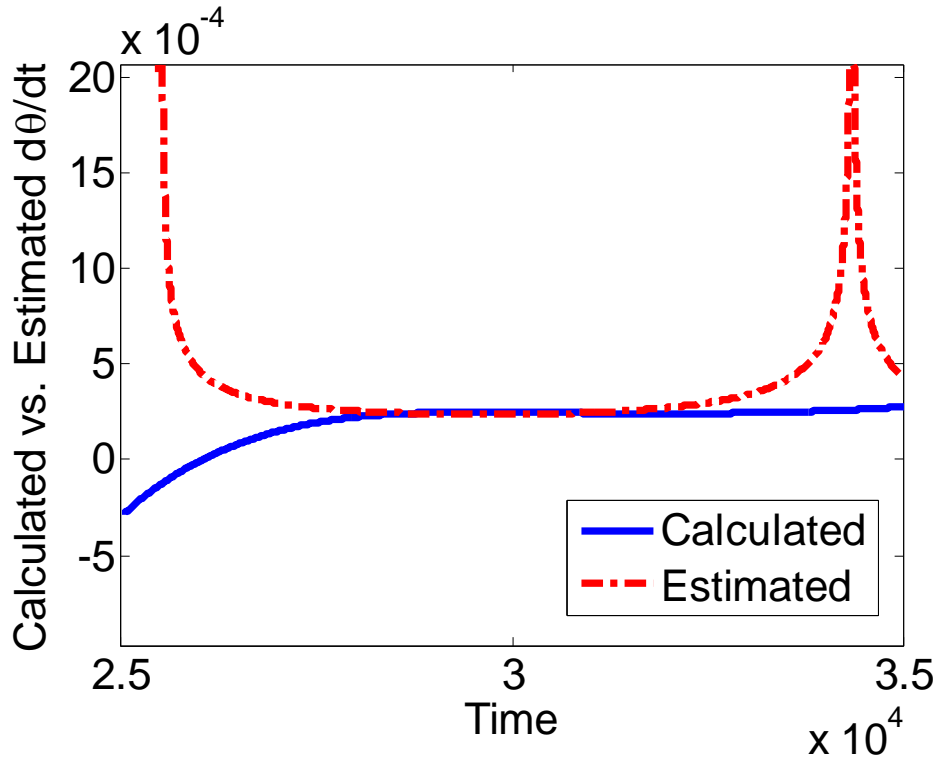


**Figure 4.4** Calculated (solid) vs. estimated (dotted)  $d\theta/dt$ , during the time interval in which the chirp frequency satisfies the Adler’s condition.

We next consider the case where the drive frequency  $\omega_1$  is fixed whereas the free-running oscillator frequency  $\omega_0$  is allowed to chirp. The symmetric feature of the phase equation (3.6a) between the free-running oscillator frequency  $\omega_0$  and the drive frequency

$\omega_1$  suggests that (4.1) to (4.6) can be modified for the reverse case in which the free-running frequency  $\omega_0$  is varied and the injected frequency  $\omega_1$  is fixed. In order to allow the free-running frequency  $\omega_0$  to vary in time, different normalization should be used, i.e. we normalize the time and the frequency with respect to the locking frequency  $\omega_1$ , which is now fixed at unity. This, however, should not change behavior of the locking process. In this case,  $d\theta/dt$  also varies as a function of time, suggesting that complete locking also cannot occur at this level of investigation.

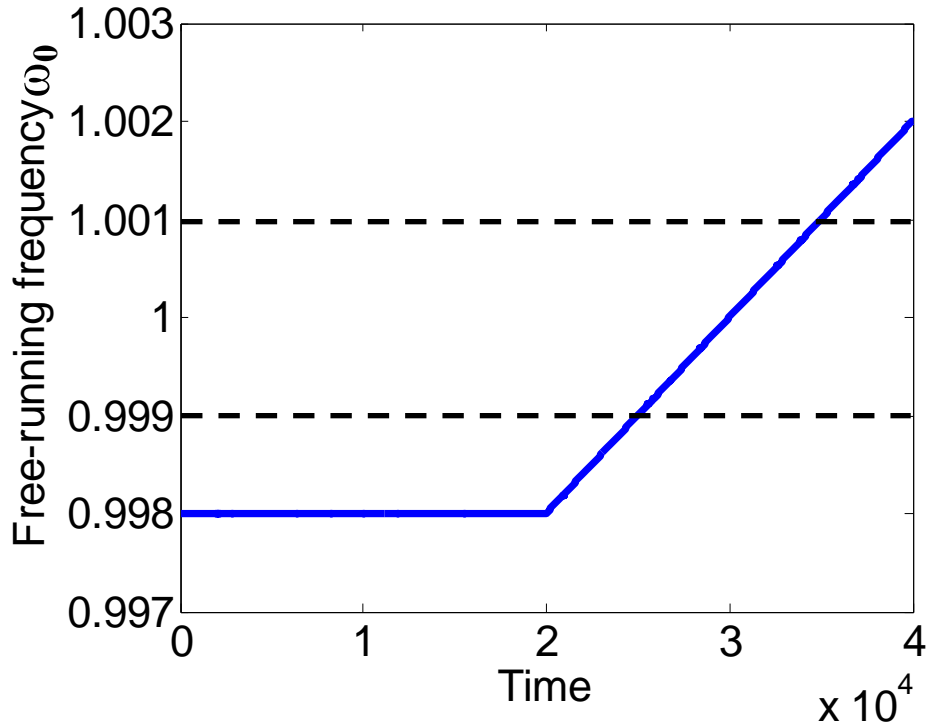


**Figure 4.5** Free-running oscillator frequency profile. Here,  $d\omega_0/dt = 2 \times 10^{-7}$ . The dotted lines show the boundaries of the locking range according to Adler's condition.

The injected frequency  $\omega_1$  is now kept constant, and is normalized to unity. The injected signal is applied after  $t = 2000$ . Figure 4.5 shows an example of the free-running oscillator frequency ( $\omega_0$ ) profile. For simplicity, the linear chirping profile for the free running oscillation is also adopted in our calculation. According to the Adler's condition,

the frequency range that the output frequency is expected to track the injected frequency is between 0.999 and 1.001 as shown in Figure 4.6. The time corresponding to this range is between  $t = 2.5 \times 10^4$  and  $t = 3.5 \times 10^4$ . Figure 4.7 shows that within this range, the differential phase shift  $d\theta/dt$  approaches zero. The calculated and the estimated value of  $d\theta/dt$  are shown in Figure 4.8.

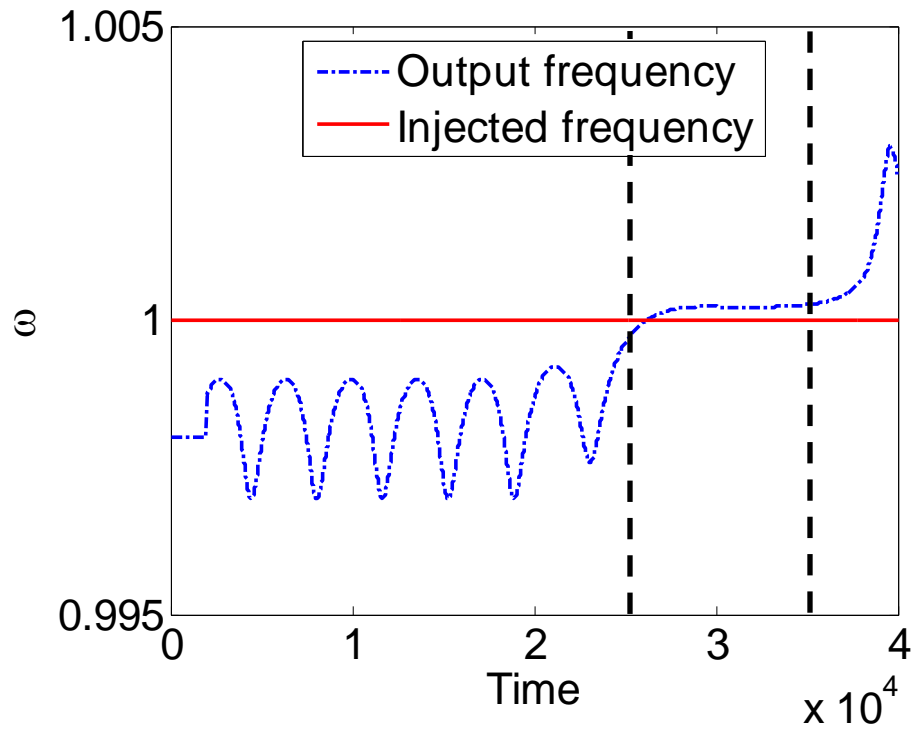


**Figure 4.6** Output (dotted) vs. injected (solid) frequency. The dotted lines show the boundaries of the locking range according to Adler's condition.

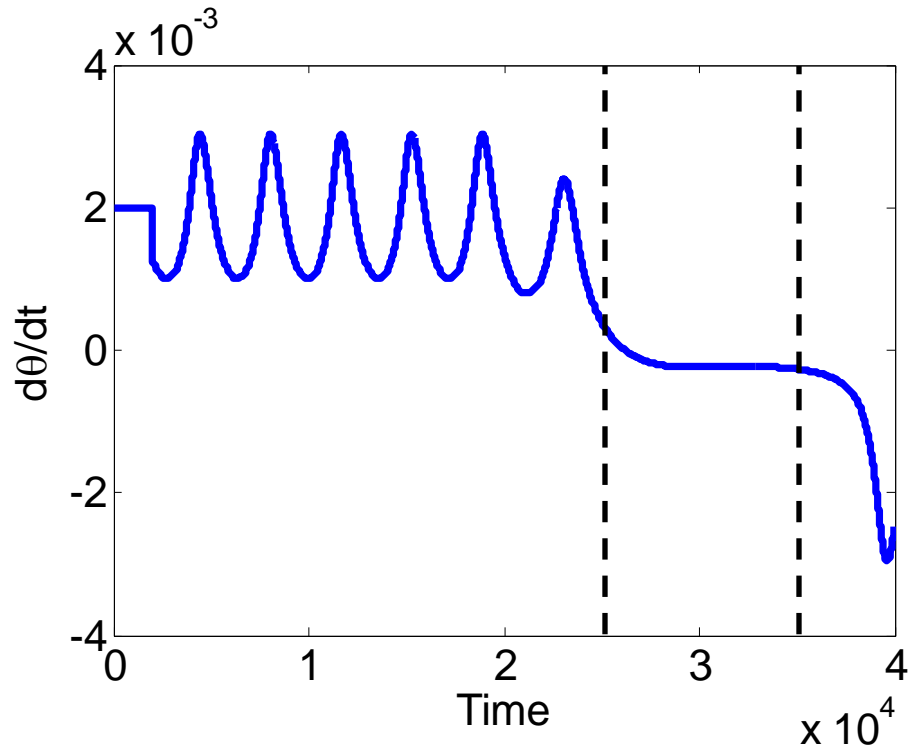


**Figure 4.7** Differential phase shift of the output signal. The injected signal is applied after  $t = 2000$ . The dotted lines show the locking range according to Adler's condition.

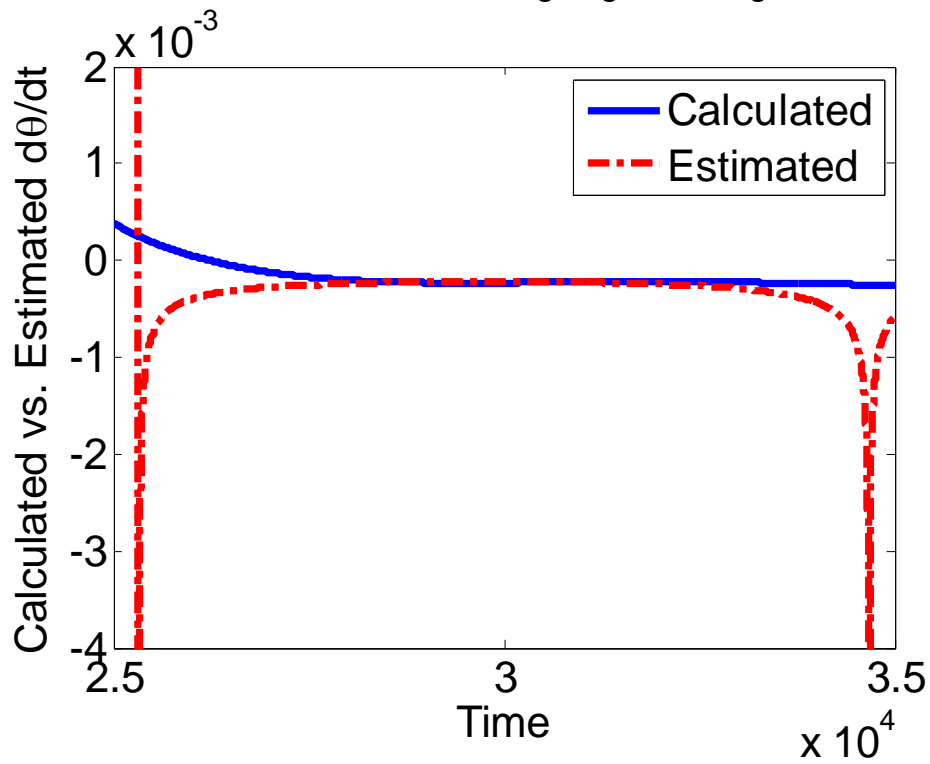


**Figure 4.8** Calculated (solid) vs. estimated (solid)  $d\theta/dt$ .

### 4.3 EFFECTS OF SMALL RANDOM FLUCTUATION IN FREQUENCY ON INJECTION LOCKING

In the presence of a small random fluctuation  $\delta\omega_0(t)$  in the free-running oscillator frequency instead of a linear chirp, there will be a random fluctuation in the relative phase. The spectrum of this phase fluctuation is next calculated. We assume that the fluctuation in the free-running oscillator is regarded as a small perturbation, and the injected frequency  $\omega_1$  is fixed at unity, once more. Consequently, the spectral density of the phase can be related to the spectral density of fluctuation in the free-running frequency. Let the free-running frequency be  $\omega_0 + \delta\omega_0(t)$ , which is varied in time, then (4.2a) can be rewritten as, with  $\theta = \theta_0 + \delta\theta_0(t)$ ,

$$\frac{d\delta\theta}{dt} + 1 - \omega_0 - \delta\omega_0 = \frac{\rho}{2Q_{ext}} \sin(\theta_0 + \delta\theta) \quad (4.7)$$

where  $\theta_0$  and  $\omega_0$  are respectively the unperturbed phase and frequency in the absence of frequency fluctuation determined from  $1 - \omega_0 = (\rho/2Q_{ext})\sin\theta_0$ .  $\delta\theta$  is the fluctuation in phase due to the fluctuation in the free running frequency  $\delta\omega_0$ . Both  $\delta\theta$  and  $\delta\omega_0$  are assumed to be small in comparison to their unperturbed values. Equation (4.7) can be linearized, which gives

$$\frac{d\delta\theta}{dt} - \delta\omega_0 = \frac{\rho}{2Q_{ext}} \delta\theta \cos\theta_0. \quad (4.8)$$

Fourier transform of (4.8) yields

$$\delta\tilde{\theta}(\omega) = \frac{\delta\tilde{\omega}_0(\omega)}{i\omega - \sqrt{\left(\frac{\rho}{2Q_{ext}}\right)^2 - (1-\omega_0)^2}} \quad (4.9)$$

where  $\delta\tilde{\theta}(\omega)$  and  $\delta\tilde{\omega}_0(\omega)$  are respectively the Fourier transforms of  $\delta\theta$  and  $\delta\omega_0$ . The spectral density of the phase noise can then be related to the spectral density of the frequency fluctuations,

$$\left|\delta\tilde{\theta}(\omega)\right|^2 = \frac{\left|\delta\tilde{\omega}_0(\omega)\right|^2}{\omega^2 + \left(\frac{\rho}{2Q_{ext}}\right)^2 - (1-\omega_0)^2}. \quad (4.10)$$

This equation shows the bounds of fluctuations until the Adler's condition is violated. Alternatively, when Adler's criterion is satisfied or nearly satisfied, the term  $(\rho/2Q_{ext})^2 - (1-\omega_0)^2$  in (4.10) is much smaller than  $\omega^2$ . Equation (4.10) gives

$$\left|\delta\tilde{\theta}(\omega)\right| \cong \delta\tilde{\omega}_0(\omega)/\omega. \quad (4.11)$$

If we approximate  $\delta\tilde{\omega}_0(\omega)/\omega$  as  $1/Q_{hot}$ , for a magnetron with a hot  $Q$  of order 100,

$\left|\delta\tilde{\theta}(\omega)\right|$  is then of order 0.01 rad or  $0.57^\circ$ .

## CHAPTER 5

# EFFECT OF RANDOM CIRCUIT FABRICATION ERRORS ON SMALL SIGNAL GAIN AND PHASE IN TRAVELING WAVE AMPLIFIERS

### 5.1 INTRODUCTION

Helix traveling wave tubes (TWTs) are widely used as amplifiers in broadband radar, communications, and electronic warfare systems [Bar05, Boo05, Gew65, Gil94, Pie50]. These devices generally consist of three major sub-components, *viz.*, an electron gun to produce and focus the beam, a helix slow wave circuit with which the beam interacts to produce amplification of an injected signal, and an electron collector that recovers energy from the spent beam. Each of these sub-components must be manufactured and integrated with the others with great precision, in order to ensure proper operation and long operating life [Dag02, Dia97, Kor98, Luh05, Sch05, Wil07]. Systematic or random errors in the manufacturing process affect TWT performance and therefore manufacturing yield, which in turn affects the cost of manufacture [Luh05, Sch05]. As TWTs are developed to meet ever more demanding requirements, especially for operation at mm-wave frequencies, the practical issue of manufacturing tolerances and yield will become increasingly important to consider [Dag02, Kor98, Wil07]. In the present chapter, we study the effects of small, random manufacturing errors in the helix and its support structure on small signal gain and on the phase of the output signal.

D'Agostino and Paoloni [Dag02] have previously considered the effects of random errors in the helix pitch on the small signal gain of a multi-section TWT. These authors assume that each section has a uniform, fixed pitch, the value of which fluctuates from tube to tube about some nominal design value; they do not consider the case that the helix pitch may vary randomly within a section as we do here. When the pitch is uniform, the classical small signal dispersion relation of Pierce [Pie50] may be directly applied to compute the small signal gain. In the present work in which we consider the effects of localized errors in the pitch and other helix parameters, however, many small errors can occur within one pitch length. For this study, therefore, Pierce's dispersion relation cannot be directly applied, and we must return to the fundamental governing differential equations in order to conduct the analysis. Our analysis, furthermore, is not limited to errors in the pitch, but also includes effects of other errors, including errors in helix radius, interaction impedance, and attenuation. As shown below, these various errors may be expressed in terms of random variations in the dimensionless Pierce parameters  $b$ ,  $C$ , and  $d$ , as functions of propagation distance  $z$ . Generally we would expect to find (and do find) that errors in the velocity parameter  $b$  are most important, since variations in  $b$  are measures of the degree of synchronism between the beam and the circuit wave, to which the gain and phase are very sensitive. Variations in  $b$  are produced by variations in helix radius and in the shape, size, and dielectric properties of the support rods, in addition to the helix pitch. The results of this work can be generalized to other types of traveling wave tube, such as coupled cavity tubes, simply by following the conventions that lead to the dimensionless Pierce parameters for the class

of TWT in question. For instance, Pierce parameters for folded waveguide TWT can be calculated following the methods described in [Ha98].

This chapter is organized as follows. Section 5.2 follows with a description of the method we have used to evaluate small signal gain in the presence of random errors. The general governing third order differential equation with randomly varying coefficients and the appropriate boundary conditions are derived. Section 5.3 presents results from the numerical integration of this equation when there are random errors presenting in the three Pierce parameters, where each case is considered separately. Section 5.4 contains some concluding remarks, including a numerical example.

## **5.2 LINEAR THEORY OF A BEAM INTERACTING WITH A SLOW WAVE CIRCUIT WITH RANDOM ERRORS**

We follow Pierce’s small signal theory of TWT, but relax the assumption of axial uniformity in the circuit parameters. This axial nonuniformity requires formulation in terms of differential equations in the axial coordinates,  $z$ . For a signal at frequency  $\omega$ , the displacement of a cold electron fluid element from its unperturbed position,  $s$ , is governed by the linearized force law, written as [Gew65, Pie50]

$$\left( \frac{\partial}{\partial z} + j\beta_e \right)^2 s = a, \tag{5.1}$$

where  $\beta_e = \omega/v_0$ , with  $v_0$  being the streaming velocity of the electron beam which is assumed to be a constant, and  $a$  is proportional to the AC electric field acting on this fluid element. We have ignored the “AC space charge effects”, i.e., Pierce’s 4QC term [Gew65, Gil94, Pie50], in writing (5.1). For THz, since the space charge effects scale as

$\omega_{pe}^2 / \omega^2$ , our assumption is justified as the electron beam plasma frequency  $\omega_{pe} / 2\pi$  is substantially lower than THz. Accompanying this AC electron displacement is an AC current that excites an RF wave in the slow wave circuit. The excitation of the circuit wave of amplitude  $a$  is governed by

$$\left( \frac{\partial}{\partial z} + j\beta_p + \beta_p Cd \right) a = -j(\beta_e C)^3 s, \quad (5.2)$$

where the right hand side represents the AC current associated with the electronic displacement,  $s$ . In (5.2),  $\beta_p = \omega/v_p$ ,  $v_p$  is the phase velocity of the slow wave in the absence of the beam,  $C$  is the dimensionless gain parameter of Pierce, given by  $\left( \frac{KI}{4V} \right)^{1/3}$ , where  $K$  is the interaction impedance,  $I$  is the beam current,  $V$  is the beam voltage, and  $d$  is the normalized cold tube circuit loss rate. Random manufacturing errors in the construction of the helix and its support structure will enter as random variations in  $z$  in the gain parameter  $C$ , in the phase velocity mismatch parameter  $b$ , and in the cold tube loss rate  $d$ . When  $C$ ,  $b$ , and  $d$  are constants, Equations (5.1) and (5.2) yield the familiar dispersion relation of Pierce [Gew65, Gil94, Pie50],

$$\delta^2(j\delta - b + jd) = 1, \quad (5.3)$$

for a wave with  $e^{j\omega t - j\beta z}$  dependence, where  $\delta = -j(\beta_p - \beta_e)/C\beta_e$ ,  $b = (\beta_p/\beta_e - 1)/C$ .

Including axial variations of  $C$ ,  $b$ , and  $d$ , we operate (5.1) by  $(\partial/\partial z + j\beta_p + \beta_p Cd)$ , use (5.2) for the right hand side to obtain a third order ordinary differential equation. Making the substitution

$$s = e^{-j\beta_e z} f = e^{-jx} f(x), \quad (5.4)$$

with  $x = \beta_e z$ , this ordinary differential equation then reads

$$\frac{d^3 f(x)}{dx^3} + jC(b - jd)\frac{d^2 f(x)}{dx^2} + jC^3 f(x) = 0. \quad (5.5)$$

Equation (5.5) gives the axial evolution of the TWT signal. We assume that the input of the TWT is located at  $x = 0$ . To integrate (5.5), we need three initial conditions on  $f$  at  $x = 0$ . They are:

$$f(0) = 0, \quad (5.6a)$$

$$f'(0) = 0, \quad (5.6b)$$

$$f''(0) = 1. \quad (5.6c)$$

Equation (5.6a) states that there is no current modulation at the input, as the current modulation is given by the RHS of (5.2), which is proportional to the electronic displacement  $f$ . Equation (5.6b) states that there is no perturbation velocity of the electron fluid element at  $x = 0$ , that is, the convective derivative of  $s$  equals zero. Note that this convective derivative, or the perturbation velocity, is related to  $f'(x)$  by (5.4) and (5.1). Thus,  $f''(x)$  is the acceleration, which is proportional to the AC electric field represented by the RHS of (5.1). The electric field variation along the  $x$ -axis then can be simply described by  $f''(x)$ , where  $f''(0)$  specifies the input electric field and is proportional to the square root of the input power at  $x = 0$ . For the present linear theory, the magnitude and phase of this input electric field is immaterial. The power gain and the phase shift are given by

$$\text{Power Gain} = \left| \frac{f''(x)}{f''(0)} \right|^2 = |f''(x)|^2, \quad (5.7a)$$

$$\text{Phase Shift} = -x + \text{angle}[f''(x)] - \text{angle}[f''(0)] = -x + \text{angle}[f''(x)], \quad (5.7b)$$

where we have used the normalization given by (5.6c).

Note that for a perfect helix of constant pitch, the coefficients in (5.5) are constants, and the solution to (5.5) subjected to initial conditions in (5.6) consists of a linear combination of three exponential solutions,  $e^{C\delta x}$ , where the  $\delta$ 's are the three roots of the algebraic equation (5.3). The three initial conditions in (5.6) determine the initial amplitudes of the three modes.

In the following section, we present results from a study of the effects of random perturbations in  $b$ ,  $C$ , and  $d$  *individually* on the solution to (5.5). Note, however, that a particular fabrication error – say an error in helix radius – will in general produce errors in all three Pierce parameters simultaneously. Nonetheless, we proceed to examine the consequences of errors on the individual Pierce parameters, one at a time, in order to understand the different effects. We anticipate and assume that the spatial scale of these random perturbations will be small compared to the slow wave wavelength.

### **5.3 EFFECTS OF RANDOM PERTURBATIONS OF THE PIERCE PARAMETERS ON SMALL SIGNAL GAIN AND PHASE**

#### ***A. Random Perturbations in the Velocity Mismatch Parameter, $b$***

Construction errors in either the helix radius or pitch, or random variations in the permittivity or geometry of the dielectric support rods, will lead to errors in the circuit wave phase velocity. A distribution of random manufacturing errors in the phase velocity may be introduced by defining a quantity  $q(x) \equiv (v_p(x) - v_{p0})/v_{p0}$  where  $v_{p0}$  is the unperturbed circuit phase velocity, which we take to be independent of  $x$ . The quantity  $q(x)$  is taken to be a piecewise continuous Gaussian random function along  $x$  centered around zero, as shown in Figure 5.1. The example in Figure 5.1 shows a profile of  $q(x)$

whose half width at half maximum (HWHM) is  $\Delta q = 0.3$ . Large values of HWHM will be used to explore the scaling from the numerical data. The generation of the random function,  $q(x)$ , is given in the Appendix B. While Gaussian distribution is used throughout the work to be reported in this Chapter, uniform distribution has also been studied and found to produce results which are qualitatively similar to the results presented here.

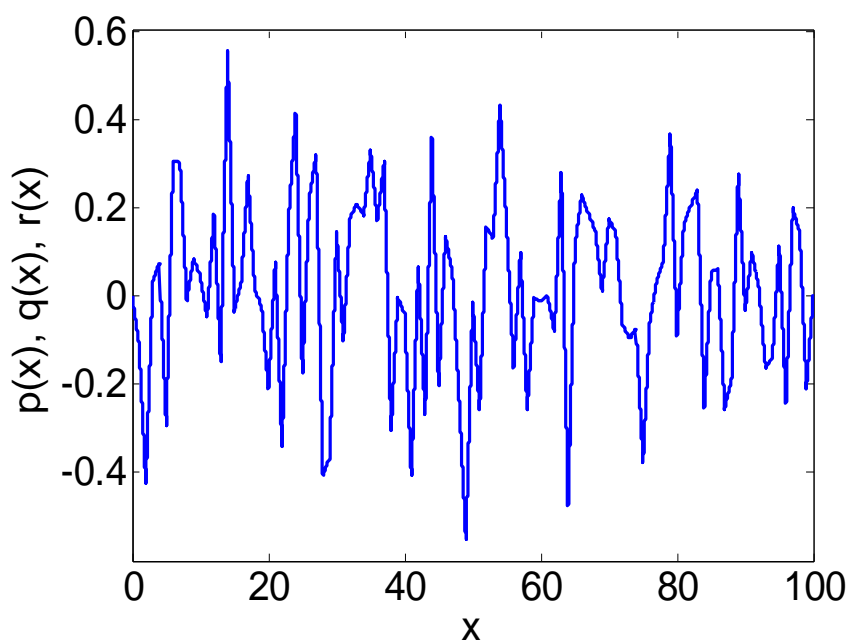


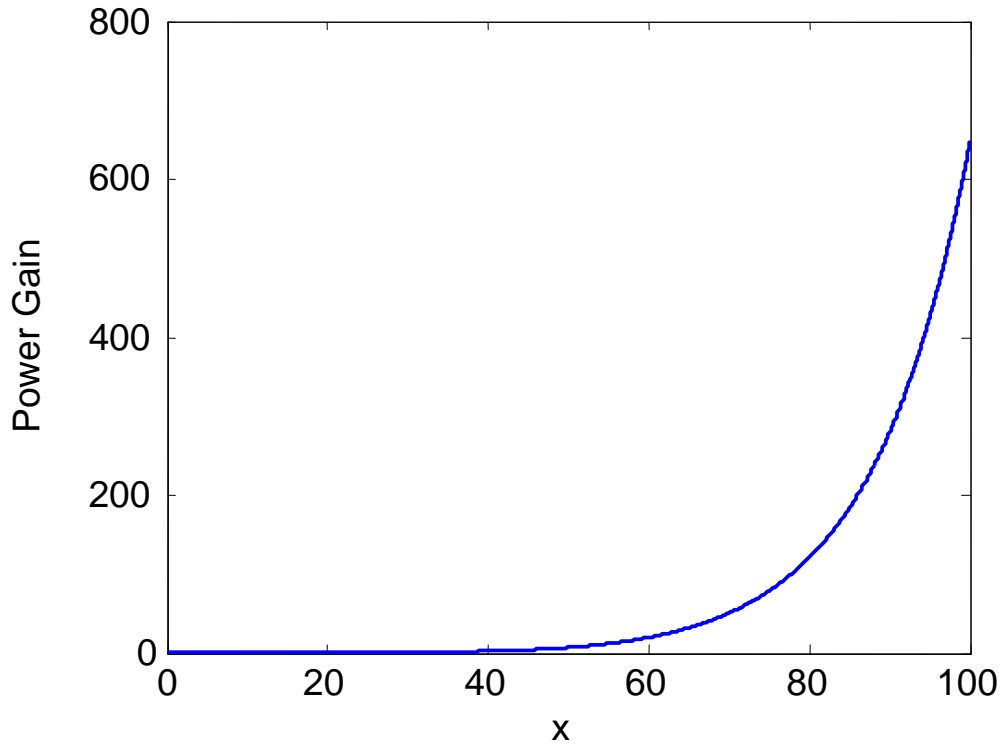
**Figure 5.1** Piecewise continuous Gaussian random function  $p(x)$ ,  $q(x)$  and  $r(x)$ , with HWHM  $\Delta p$ ,  $\Delta q$ , and  $\Delta r$ , respectively. Here,  $\Delta p = \Delta q = \Delta r = 0.3$ .

For a lossless circuit ( $d = 0$ ), Equation (5.5) becomes

$$\frac{d^3 f(x)}{dx^3} + j \left[ \frac{Cb_0 - q(x)}{1 + q(x)} \right] \frac{d^2 f(x)}{dx^2} + jC^3 f(x) = 0 \quad (5.8)$$

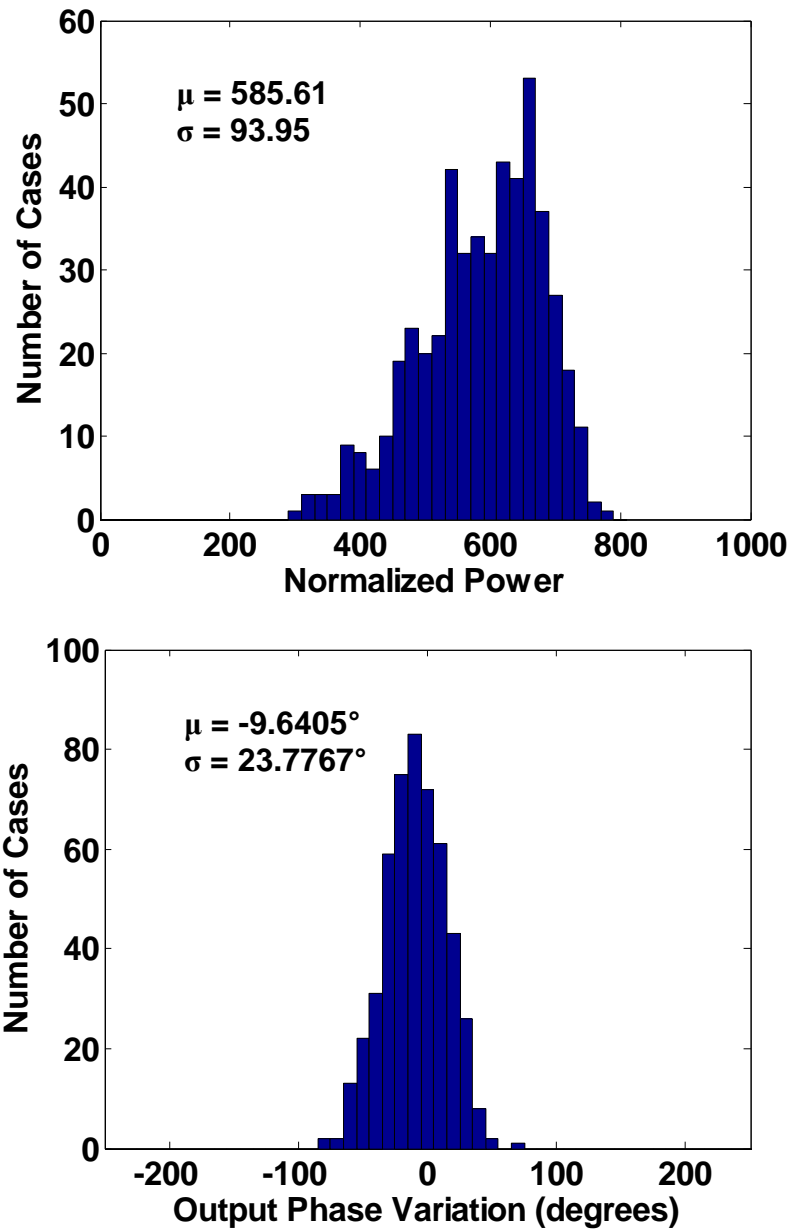
where  $b_0$  is the unperturbed beam-circuit synchronization parameter as defined after (5.3). Without the perturbation ( $q(x) = 0$ ) and assuming perfect beam-circuit synchronization ( $b_0 = 0$ ), power gain along  $x$  can be calculated using (5.7). The result is

shown in Figure 5.2 for  $C = C_0 = 0.05$ . For a circuit of length  $x = 100$ , the small signal power gain is 647.19, or 28.1 dB.



**Figure 5.2** Power gain along  $x$  assuming lossless circuit, perfect beam-circuit synchronization, and no perturbation.  $C = 0.05$ . The maximum power gain at  $x = 100$  is 647.19, or 28.11 dB.

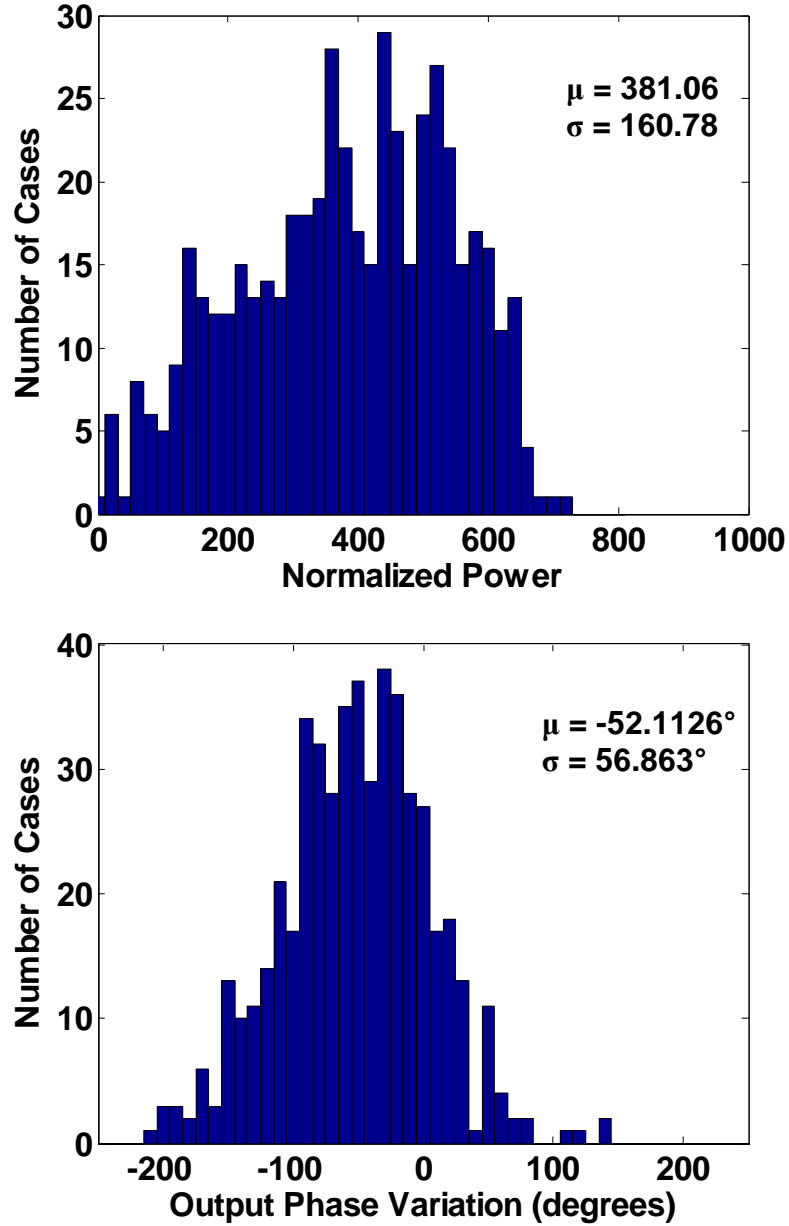
Figures 5.3 and 5.4 show the statistical distributions of power gain and output phase variation (with respect to the unperturbed case) at  $x = 100$  for 10% and 20% circuit phase velocity perturbation, i.e.,  $\Delta q = 0.1$  and  $0.2$ . The mean value  $\mu$  and the standard deviation  $\sigma$  are given in each case. With 10% perturbation, power gain drops by 10% while the output phase variation is about  $10^\circ$  change from the unperturbed case. With 20% perturbation, power gain drops by 40%, and the output phase variation can be as high as  $52^\circ$ .



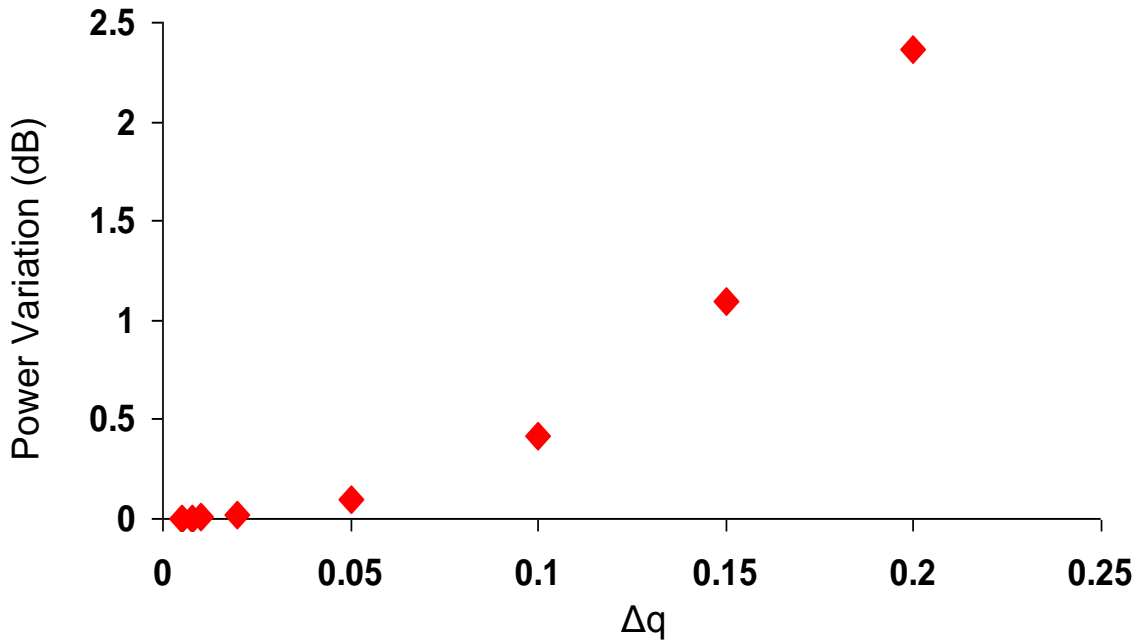
**Figure 5.3** Power gain and output phase variation at  $x = 100$  when the circuit phase velocity is perturbed.  $b_0 = 0$ ,  $C = 0.05$ , and  $\Delta q = 0.1$  (HWHM of 10% in circuit phase velocity). Without perturbation, power gain and output phase variation at  $x = 100$  are respectively 647.19 and 0.

Figure 5.5 shows the amount of power variation at  $x = 100$  for other values of  $\Delta q$ . In order to achieve 0.5dB power variation which is a typical performance specification for L- and S-band tubes,  $\Delta q$  must be less than 10%. This can easily be satisfied in

conventional TWT operating in the microwave bands. However, for a millimeter or sub-mm wave device (W-band and above), this level of manufacturing precision may be much more difficult to achieve.



**Figure 5.4** Power gain and output phase variation at  $x = 100$  when the circuit phase velocity is perturbed.  $b_0 = 0$ ,  $C = 0.05$ , and  $\Delta q = 0.2$  (HWHM of 20% in circuit phase velocity). Without perturbation, power gain and output phase variation at  $x = 100$  are respectively 647.19 and 0.



**Figure 5.5** Mean value of power variation at  $x = 100$  for different value of  $\Delta q$ .  $C = 0.05$ ,  $b_0 = 0$ .

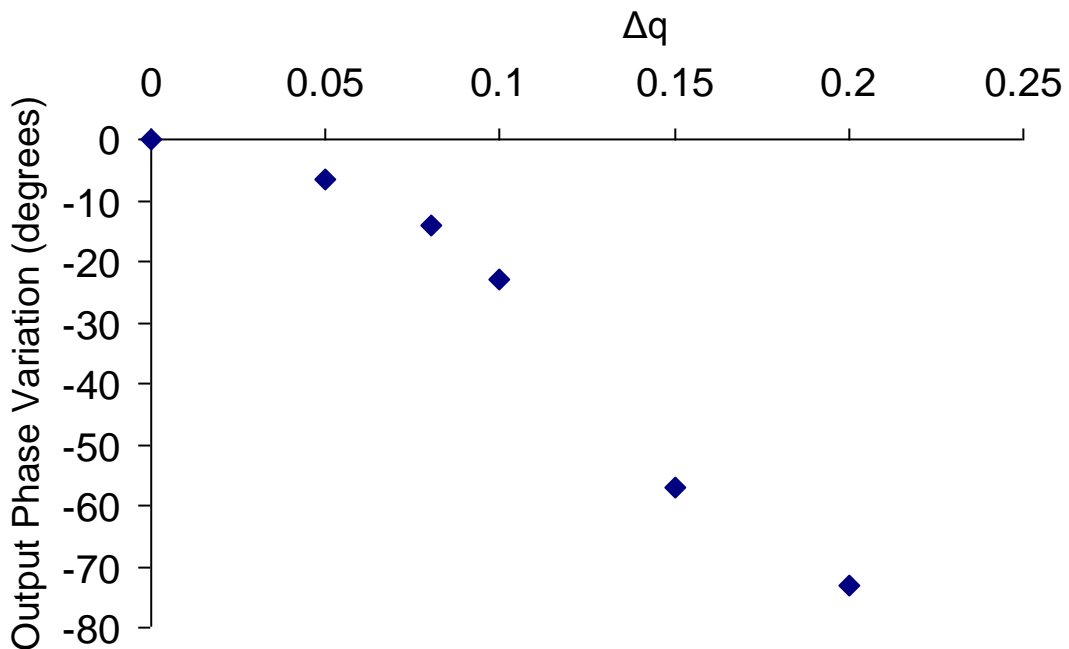


**Figure 5.6** Mean value of the phase variation for different degrees of perturbations. Each data point represents 500 samples. The output phase is calculated at  $x = 190$ , and  $C = 0.021$  so the output power gain is 20dB when there is no perturbation.  $b_0 = 0$ .

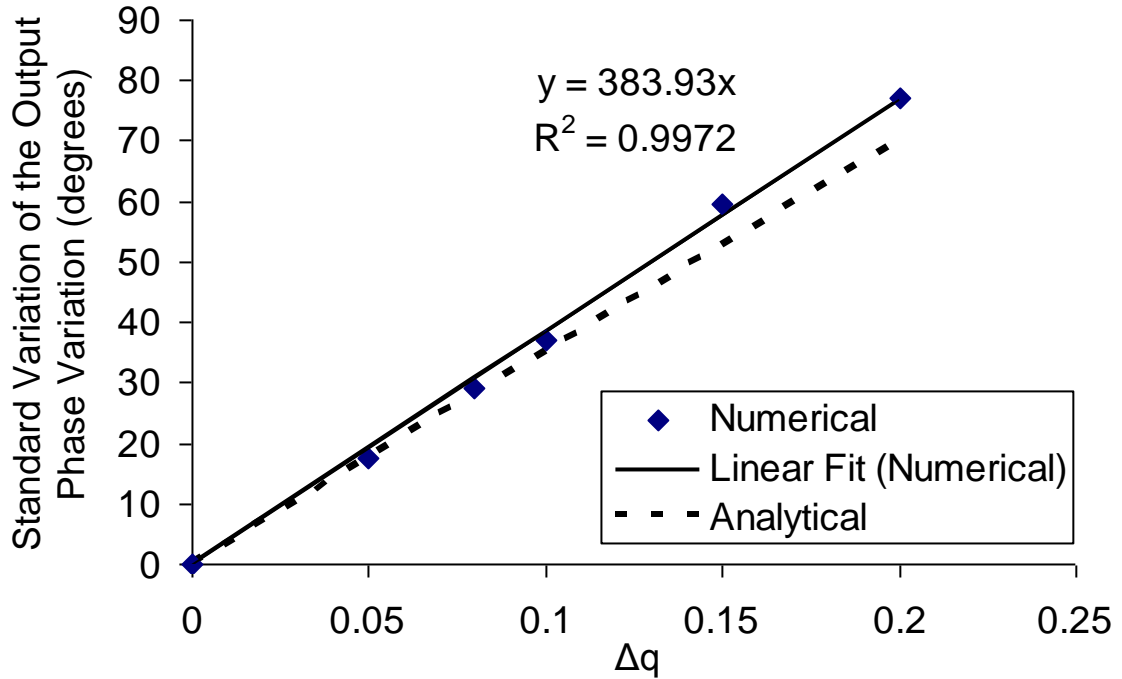


**Figure 5.7** Standard deviation of the output phase variation for different degrees of perturbations in  $v_p$ .

Further analysis of the output signal after passing through an arbitrary distance with perturbations  $q(x)$  shows the linear correlation between the standard deviation of the output phase variation (in comparison to the unperturbed case) and the size of the perturbations. Figures 5.6 and 5.7 show respectively the mean and the standard deviation of the output phase variation as a function of  $\Delta q$ . The linear relationship displayed in Figure 5.7 is useful for calculating the tolerance limit for manufacturing error for a small perturbation. It is confirmed by the recent analytic theory proposed by Chernin and Lau [Che07] as shown by the dotted line in Figure 5.7. The example shown in Figures 5.6 and 5.7 has Pierce parameter values similar to those of a 400 GHz folded waveguide TWT designed by Booske et al. [Boo02].

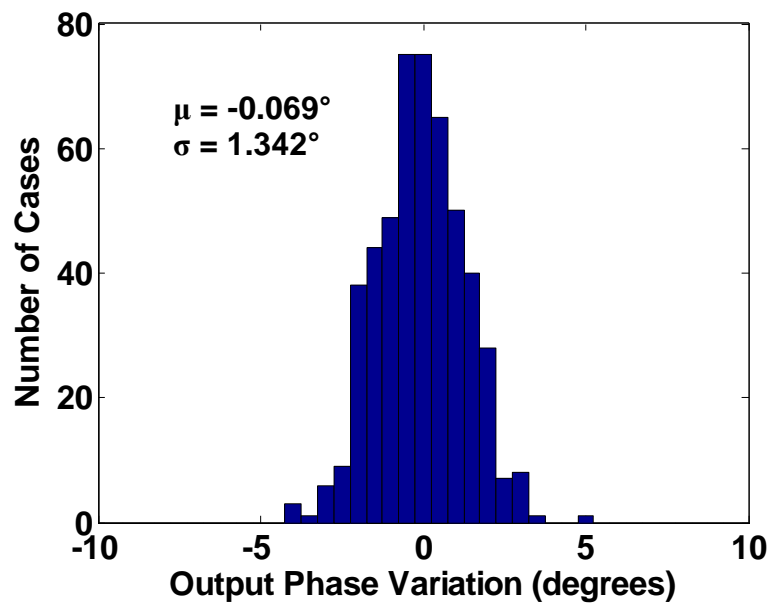
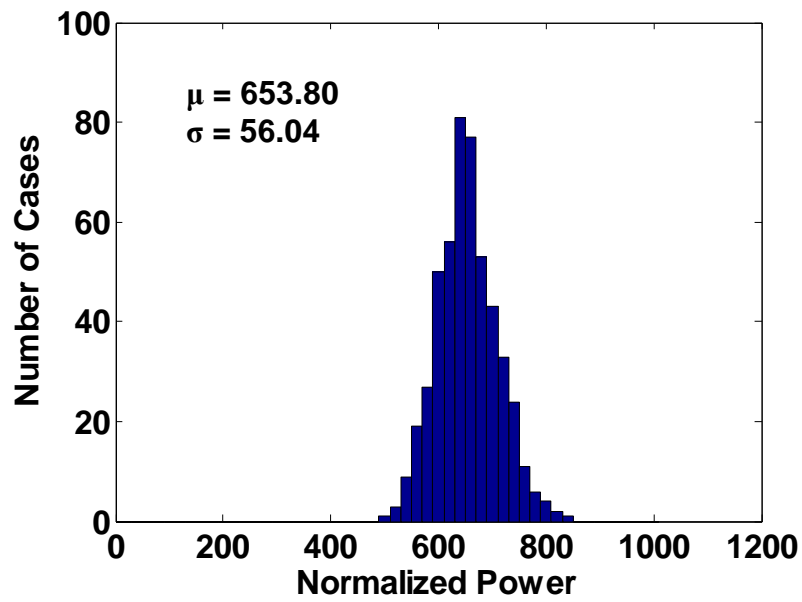
### ***B. Random Perturbations in the Coupling Parameter, $C$***

Construction errors in the helix radius will also produce errors in the interaction impedance, which in turn produce corresponding random errors in the Pierce gain parameter  $C$ . The coupling parameter can be written to include a small perturbation as  $C^3 = C_0^3[1 + p(x)]$ , where  $C_0$  is the unperturbed coupling parameter, and  $p(x)$  is the perturbation quantity whose definition is analogous to that of  $q(x)$  as shown in Figure 5.1. For  $b = d = 0$ , Equation (5.5) becomes

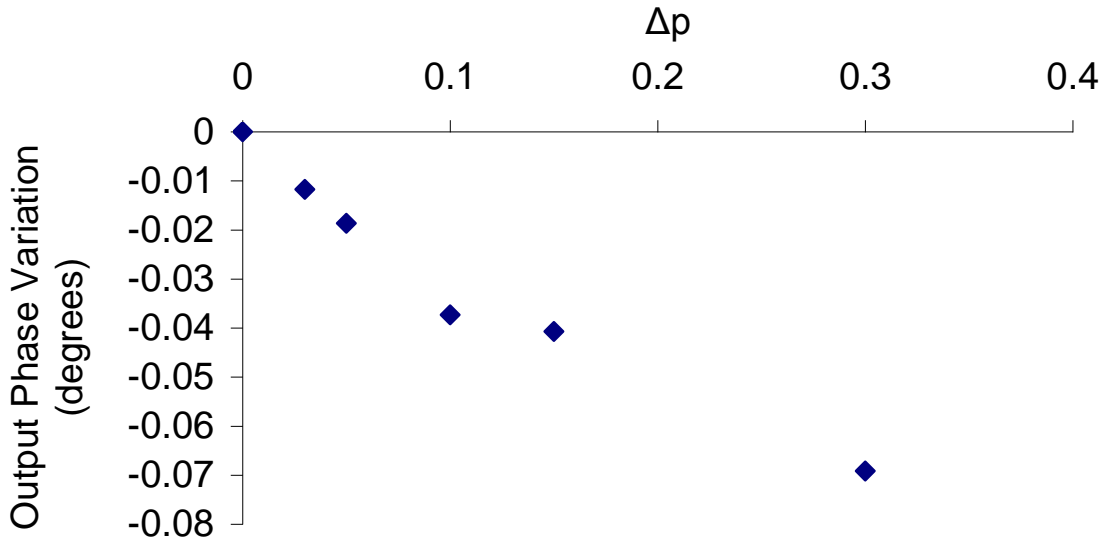
$$\frac{d^3 f(x)}{dx^3} + jC_0^3[1 + p(x)]f(x) = 0. \quad (5.9)$$

Figure 5.8 shows the statistical distribution of the power gain and the output phase variation at  $x = 100$  when the HWHM of  $p(x)$  is 0.3 ( $\Delta p = 0.3$ ), which is equivalent to HWHM of about 10% in  $C_0$ . The variations, in particular in the output phase, are much smaller in comparison to the effects of random errors in the circuit phase velocity  $v_p$ , as illustrated in Figures 5.3 and 5.4. Nevertheless the spread in the distribution shows that in certain cases, power gain can vary between 27.0 and 29.3 dB, which is still noticeable in comparison to the unperturbed case at 28.1 dB.

Output phase variation is not greatly affected by the perturbation in  $C$ . This is demonstrated more sharply in Figures 5.9 and 5.10, which show the mean and the standard deviation of the output phase variations for various degrees of perturbation of  $C$ . The linear relationship between the standard deviation of the output phase variation and the size of perturbations ( $\Delta p$ ) still exists as shown in Figure 5.10. The data shown in Figure 5.10 are in excellent agreement with the recently developed analytic theory [Che07], as shown by the dotted line in Figure 5.10.



**Figure 5.8** Power gain and output phase variation at  $x = 100$  when the coupling parameter  $C$  is perturbed.  $C_0 = 0.05$ , and  $\Delta p = 0.3$  (HWHM of 10% in  $C$ ). Without perturbation, power gain and output phase variation at  $x = 100$  are respectively 647.19 and 0.



**Figure 5.9** Mean value of the phase variation for different degrees of perturbations in  $C$ . Each data point represents 500 samples. The output phase is calculated at  $x = 100$ ,  $C_0 = 0.05$ , and  $b_0 = 0$ .

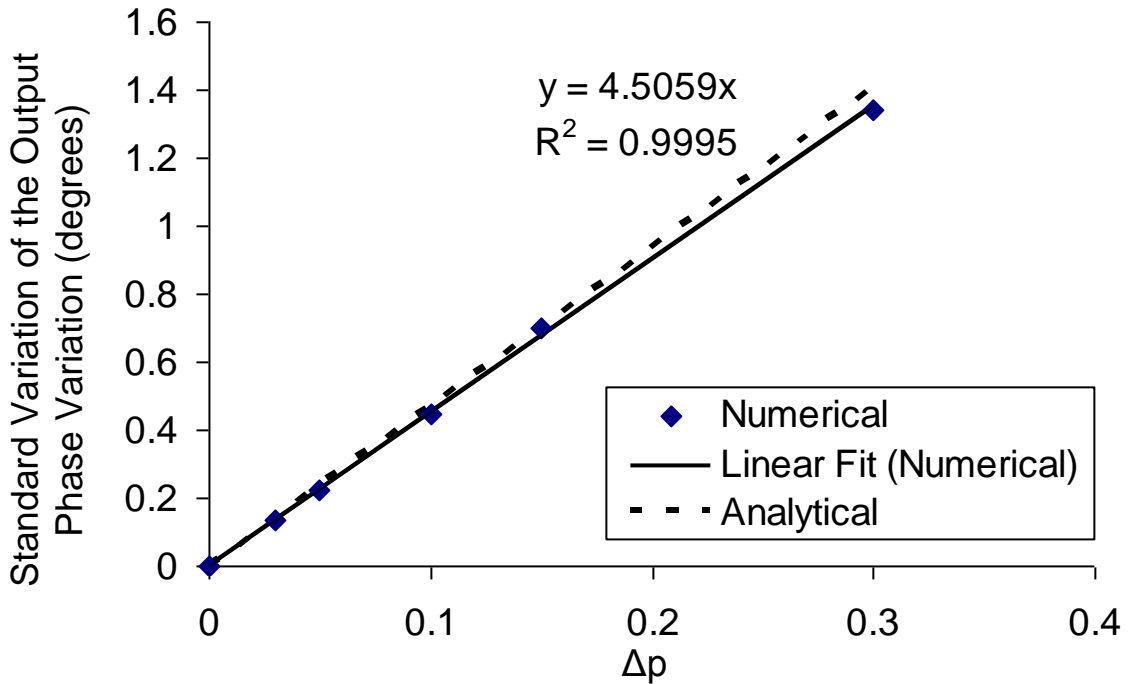


**Figure 5.10** Standard deviation of the output phase variation for different degrees of perturbations in  $C$ .

### ***C. Random Perturbations in the Circuit Loss, $d$***

Random variations in circuit loss can be produced by imperfections in either the helix or supporting dielectric structure. We can study the effect of these variations by setting  $b = 0$  in (5.5):

$$\frac{d^3 f(x)}{dx^3} - jC[jd_0 + jr(x)]\frac{d^2 f(x)}{dx^2} + jC^3 f(x) = 0 \quad (5.10)$$

where  $d_0$  is the unperturbed circuit loss, and  $r(x)$  is its perturbation similar to  $p(x)$  and  $q(x)$  as shown in Figure 5.1. Figure 5.11 shows the statistical distribution of power gain and output phase variation at  $x = 100$  for  $b = 0$ ,  $C = 0.05$ ,  $d_0 = 1$ , and the HWHM of  $r(x)$  is  $\Delta r = 0.4$ . It is found that the effect of perturbation in  $d$  is small in comparison to the perturbation in  $v_p$  even with 40% variation in circuit loss. Figures 5.12 and 5.13 respectively show the mean and the standard deviation of the output phase variations for various degrees of perturbations in  $d$ . A linear relation between the HWHM of the error distribution and the standard deviation of the output phase distribution is again obtained and illustrated in Figure 5.13. Once more, the data shown in Figure 5.13 are in excellent agreement with the analytic theory developed by Chernin and Lau [Che07], as shown by the dotted line in Figure 5.13.

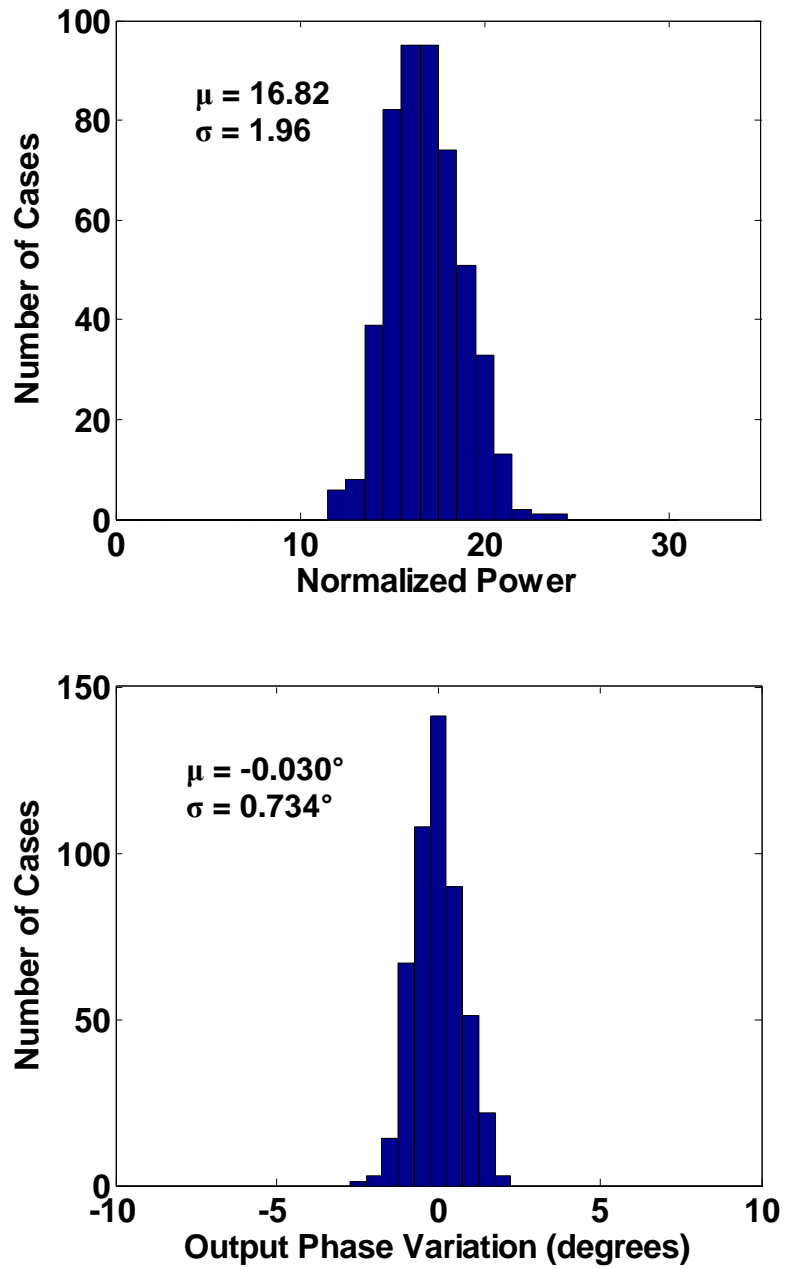


**Figure 5.11** Power gain and output phase variation at  $x = 100$  when the circuit loss  $d$  is perturbed.  $C_0 = 0.05$ , and  $\Delta r = 0.4$  (HWHM of 40% in  $d$ ). Without perturbation, power gain and output phase variation at  $x = 100$  are respectively 16.87 and 0.

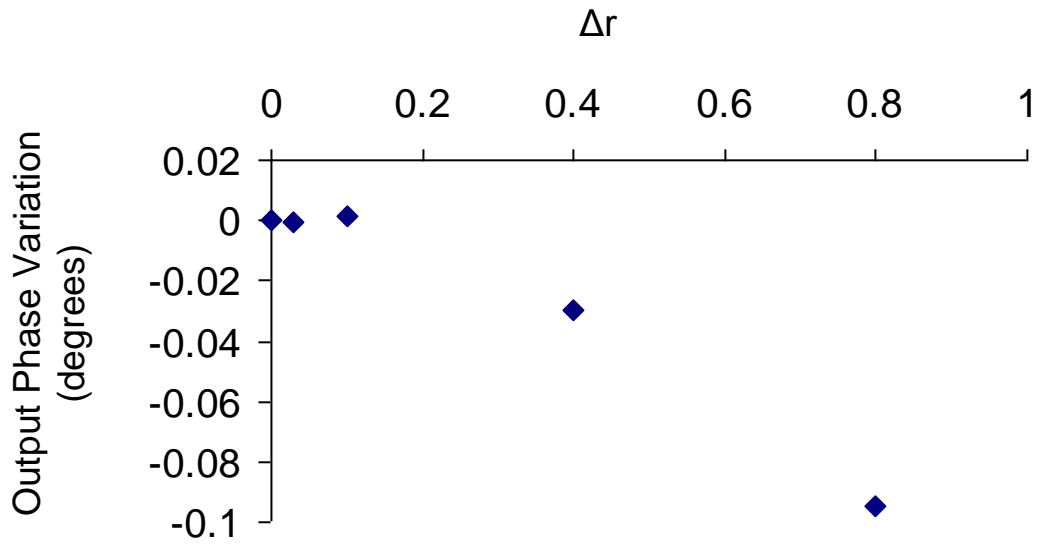


**Figure 5.12** Mean value of the phase variation for different degrees of perturbations in  $d$ . Each data point represents 500 samples. The output phase is calculated at  $x = 100$ ,  $C_0 = 0.05$ ,  $b_0 = 0$ , and  $d_0 = 1$ .

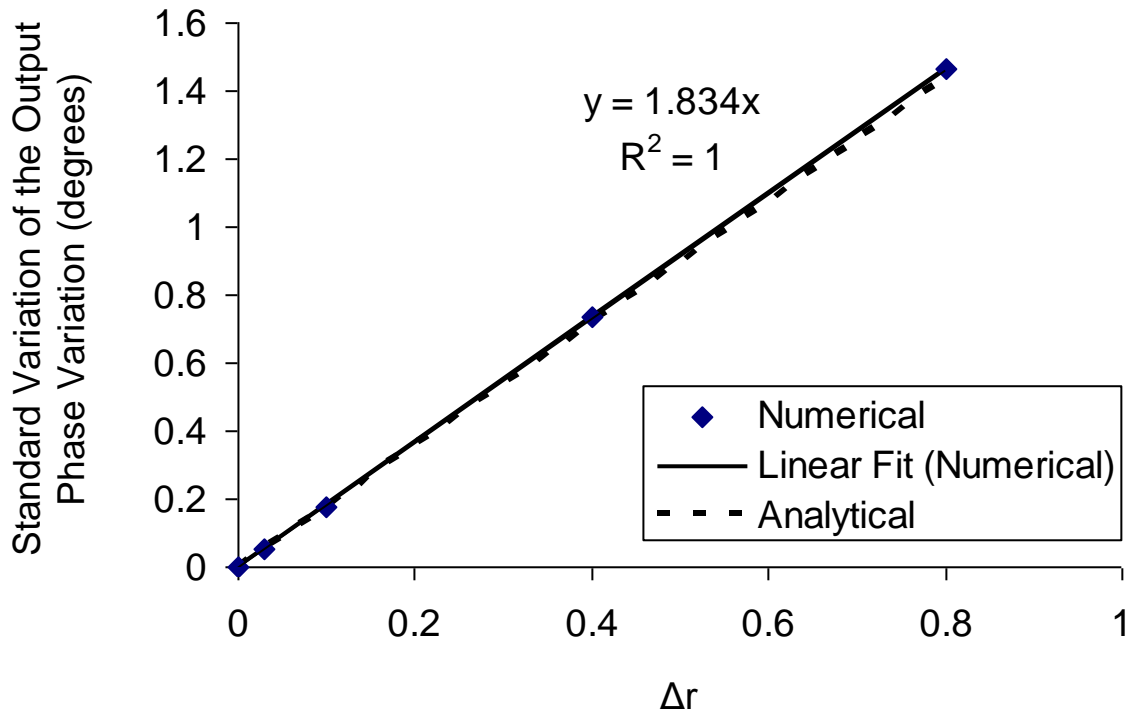


**Figure 5.13** Standard deviation of the output phase variation for different degrees of perturbations in  $d$ .

## 5.4 REMARKS

In this chapter, we study the effects on the phase and small signal gain of a TWT due to variations in  $C$ ,  $b$  and  $d$  that are randomly distributed along the axis. These random variations are used to model manufacturing errors, which might be significant in the mm-wave and THz regimes. This effort was deemed especially important for such very high frequency tubes, as the errors could become appreciable fractions of small electromagnetic feature size. Furthermore, one path to high power at high frequency would be power combining of multiple tubes. It is clear that variation in the phase and the gain of individual tubes is important to quantify for this application. Our work is complementary to previous research [Dag02, Kor98], in that it isolates the various manufacturing errors in physically meaningful variables, and shows the independent effect of a given error on tube performance, albeit in the linear regime, and a piecewise continuous model is used. We have purposely extended the range of variation to include unusually large random errors, and in doing so, we have established the linear relation between the standard variations in the output phase variation and the individual perturbations in  $b$ ,  $C$ , and  $d$ , as shown in Figures 5.7, 5.10, and 5.13. Once such a linear relationship is established, evaluation of a particular tube (with a specific set of design parameters) and the tolerance allowed in the output phase may then be assessed by obtaining just *one* data point, such as those displayed in Figure 5.7, for that particular tube. This assessment is confirmed by the recently developed analytic theory [Che07]. It is plausible that comparatively large manufacturing errors may mimic reality, as small TWT structures are developed to push into the THz frequency regime. Recent inquiries, for example, suggest that errors as large as  $5\mu\text{m}$  on  $50\mu\text{m}$  features for devices operating

at 100's of GHz are possible (worst case) using the x-ray Lithography, Galvanoformung, und Abformung (LIGA) manufacturing [Sch05]. In general, random variations in the circuit phase velocity would produce the most pronounced variations in the small signal gain and in the output phase.

We may use a simple helix to estimate the variations in  $b$ ,  $C$ , and  $d$  in terms of the variations in the radius  $a$  and in the periodicity  $L$  of this helix. In the simplest model,  $C^3 = K/4R_0$  where  $R_0$  is the beam impedance, which is assumed fixed, and  $K$  is the circuit impedance which is proportional to  $1/a$  to the lowest order [Gew65]. Thus,  $\Delta p = \Delta C^3/C^3 = \Delta a/a$ . The circuit phase velocity,  $v_p$ , is  $cL/(2\pi a)$  where  $c$  is the speed of light. Since  $q(x) = v_p(x)/v_{p0} - 1$ , we then have  $\Delta q = \Delta v_p/v_p = [(\Delta L/L)^2 + (\Delta a/a)^2]^{1/2}$ , where we have assumed that the random errors  $\Delta L$  and  $\Delta a$  are uncorrelated. Finally, the normalized attenuation rate is  $d = \alpha/(\beta_e C)$  where  $\alpha$  is the cold tube attenuation rate (per meter) in the circuit electric field amplitude, and therefore  $\Delta r = \Delta d = \Delta \alpha/(\beta_e C)$  to the lowest order. From these estimates of the HWHM's  $\Delta q$ ,  $\Delta p$ , and  $\Delta r$  for, respectively, the circuit phase velocity,  $C^3$ , and cold tube loss rate, we see that manufacturing errors in the circuit dimensions will produce the largest HWHM  $\Delta q$ . Our analysis also shows that it is this variation in the circuit phase velocity, which produces the greatest variations in the output phase and in the small signal gain. Using the LIGA example [Sch05], variations in  $a$  and  $L$  may approach 10%, in which case  $\Delta q = 14.14\%$ , and Figure 5.7 shows that the standard deviation in the output phase may be as high as 50 degrees in a tube with  $b_0 = 0$ ,  $C = 0.05$ , and a small signal gain of 28.1 dB.

The governing equation (5.5) has mostly constant coefficients. These coefficients contain small amplitude, random functions of  $x$ . In fact, under such a condition, it is not

clear if the continuum description according to (5.5) can be justified, even though one may argue that it is plausible. Despite such limitations, the present chapter gives an assessment on the effects of manufacturing errors that are distributed randomly along the axis of a TWT, in the small signal regime. An analytical theory is developed recently which corroborated with the numerical computations given in this Chapter. The effects on large signal behavior await further study and computational analysis, while building on the current small signal results.

Lastly, while solid-state amplifiers have been considered a newer technology, and have received many interests in terahertz research, their problems manifest in the low operating temperature requirement, and the ability to recover the un-spent beam energy. These problems are responsible for the low efficiency of solid-state devices in comparison to the efficiency of microwave vacuum electronic devices such as TWT [Sch05].

## CHAPTER 6

### SUMMARY AND CONCLUSIONS

In this thesis, several contemporary issues of magnetron and traveling wave tube (TWT) have been examined. These issues are motivated by ongoing experiments, and by future experiments being planned on high power microwave generation and THz radiation sources.

#### 6.1 ON THE DISCOVERY OF PARAMETRIC INSTABILITY IN A MAGNETICALLY PRIMED MAGNETRON

In Chapter 2, a single electron orbit model has been constructed in order to analyze the mechanisms behind the rapid startup and the low noise behaviors of a magnetically primed magnetron. These behaviors have been observed in previous magnetic priming experiments [Nec03a, Nec04, Nec05a, Nec05b] and particle simulations [Jon04a, Lug04] on kilowatt CW magnetrons. The model shows evidences of fast electron prebunching on the order of the Larmor period and five-fold symmetry in electron dynamics when five magnetic field perturbation periods are axially imposed (magnetic priming for a 10-cavity magnetron). At least 50% expansion in electron maximum excursion has been achieved for all values of the magnetic priming strength  $\alpha$  considered. These fast prebunching and five-fold spoke formation can potentially reduce

the startup time of a magnetron, especially during the initial phase before the space charge effects and the electron interactions with RF take place.

A parametric instability in the electron orbits due to the magnetic field perturbation has been discovered. For certain bands of values of magnetic priming strength  $\alpha$ , the electron maximum excursion increases dramatically, which is a key signature of a parametric instability. The location of these bands can be predicted from the three characteristic frequencies of the model: the two electron cyclotron frequencies corresponding to the maximum and the minimum magnetic fields, and the frequency associated with the spatial periodicity in the periodic magnetic field. This orbital parametric instability is one of the reasons believed to have contributed to the rapid startup in the oven magnetron. Extension of magnetic priming on a relativistic magnetron is currently under investigation [Hof07].

Interesting areas for future work include the effects of space charge on the orbital parametric instability. The excitation of RF mode by magnetic priming requires further study than the single orbit theory considered in this thesis.

## **6.2 ON THE INJECTION LOCKING OF MAGNETRONS**

Phase-locking is utilized today in many important applications either to achieve good phase control or to combine power of multiple sources. In Chapter 3, an analysis of a magnetron-specific circuit model for injection locking process has been performed. The model agrees with the Adler's condition on phase locking. In frequency domain, the model is able to produce output spectra, for different phase locking regimes, which are in qualitative agreement with the results from previous injection locking experiments

between two kilowatt CW magnetrons. [Nec05b] The following phase-locking characteristics have been observed both in the experiments and in the numerical simulation based upon the model. When the locking criterion predicted by the Adler's condition is not satisfied, phase locking does not occur, and the output mainly oscillates at its natural frequency. However, interference from the low-level injected signal causes the output to also oscillate at sidebands corresponding to integer multiples of the beat frequencies of the two magnetrons. When the locking criterion is satisfied, the output signal oscillates at the same frequency as the injected signal, and the output phase becomes locked to the phase of the injected signal.

In time domain, the model recovers both amplitude and phase characteristic during the injection locking process. This analysis is extended in Chapter 4, where the frequency of one of the two magnetrons is allowed to vary linearly in time. Numerical simulation suggests that complete locking between the two magnetrons can no longer occur. That is, the phase difference between the two magnetrons cannot be constant. The variation of the phase difference is small, however, during the time interval in which Adler's locking criterion is satisfied. In such case, the output frequency tracks the injected frequency in time. When the free-running frequency fluctuates in time, the fluctuation in output phase at a fixed drive frequency has been assessed.

The injection locking study presented in Chapter 2 is limited to master-to-slave configuration. That is, one magnetron acts as a master and is unaffected by the signal from the other magnetron, which acts as a slave. This type of configuration is applicable for injection locking of multiple magnetrons which utilizes one master to control multiple slaves. A different configuration known as peer-to-peer may be similarly formulated. In

the latter configuration, each magnetron may play both the roles of master and slave for the remaining magnetrons. This type of configuration is interesting because of its practicality in power combining. For instance, since signal is allowed to travel in both directions between two magnetrons connected by peer-to-peer configuration, the three circulators in Figure 3.6 would not be needed.

The lockability of multiple magnetrons in a peer-to-peer configuration is a rich area for future study.

### **6.3 ON THE EFFECTS OF RANDOM MANUFACTURING ERRORS ON TWT PERFORMANCE**

As TWTs are developed to meet ever more demanding requirements, especially for operation at mm and submillimeter wave frequencies, the practical issue of manufacturing tolerances and yield will become increasingly important to consider [Dag02, Kor98, Wil07]. In Chapter 5, random manufacturing errors have been translated to random variations in Pierce's gain parameter  $C$ , in the phase velocity mismatch parameter  $b$ , and in the cold tube loss rate  $d$ . Effects of the random variations in these individual parameters on the TWT gain and phase stability have been evaluated using small signal theory in a continuum model.

Construction errors in either the helix radius or pitch, or random variations in the permittivity or geometry of the dielectric support rods, will lead to errors in the circuit wave phase velocity. Construction errors in the helix radius will also produce errors in the interaction impedance, which in turn produce corresponding random errors in the

Pierce gain parameter  $C$ . Random variations in circuit loss can be produced by imperfections in either the helix or supporting dielectric structure.

It is found that errors in the velocity parameter  $b$  are most important, which should not be too surprising since variations in  $b$  are measures of the degree of synchronism between the beam and the circuit wave, to which the gain and phase are very sensitive. Further analysis of the output signal after passing through an arbitrary distance with perturbations shows a linear correlation between the standard deviation of the output phase variation (in comparison to the unperturbed case) and the size of the perturbations. The linear relationship is useful for calculating the tolerance limit for manufacturing error for a small perturbation. All of these findings have been confirmed by an analytic theory recently developed. The results of this work can be generalized to other types of traveling wave tube, such as coupled cavity tubes, simply by following the conventions that lead to the dimensionless Pierce parameters for the class of TWT in question.

Even if the development of THz TWT is still in its infancy, an evaluation of the composite effects on the Pierce parameters  $b$ ,  $C$ , and  $d$  by fabrication errors, for instance in a folded waveguide structure, is an area worthy of future study.

## **APPENDICES**

## A. ELECTRON ORBITS IN SINUSOIDAL AND SMOOTH-BOUNDARY MAGNETIC FIELD PROFILES

In addition to square magnetic field profile shown in Figure 2.1, sinusoidal and smooth-boundary magnetic field profiles shown below in Figures A.1 and A.2 have been considered. The normalized maximum magnetic field in these cases is 1 and the normalized minimum magnetic field is 0.733 so that the magnetic priming strength  $\alpha$  remains 0.267 as in the square magnetic field case. The period of the magnetic field perturbation is 90 units in  $y$ -direction, the same as in Figure 2.1

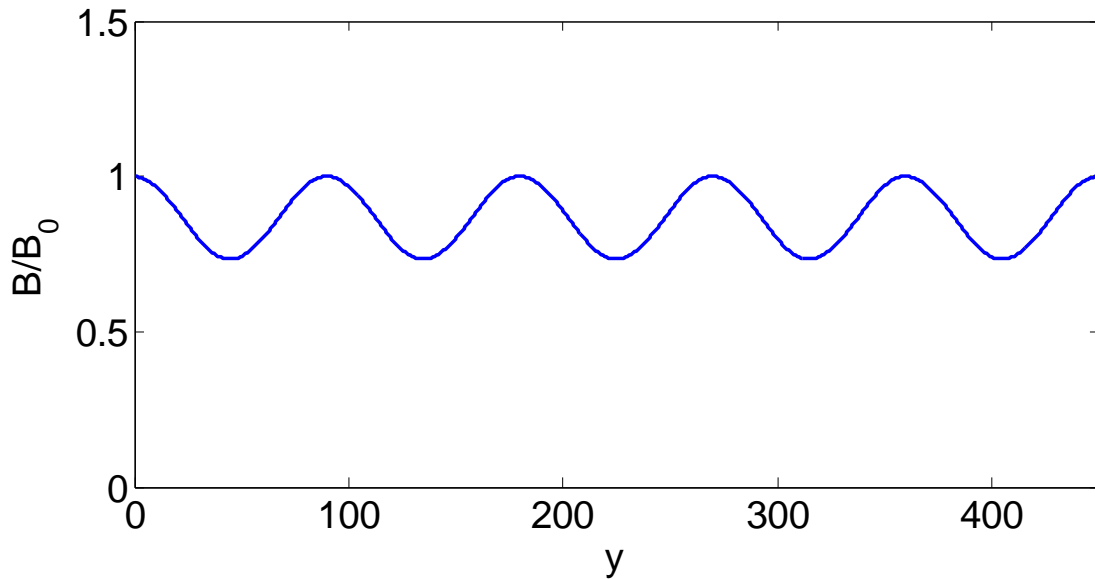


**Figure A.1** Sinusoidal magnetic field profile

The maximum excursion in  $x$  as a function of  $y_0$  for the sinusoidal magnetic field profile in Figure A.1 is shown in Figure A.3. The overall maximum excursion is considerably reduced although it is still larger than in the unperturbed case. Figure A.3 retains the shape of sinusoidal which is to be expected because of the smooth profile.

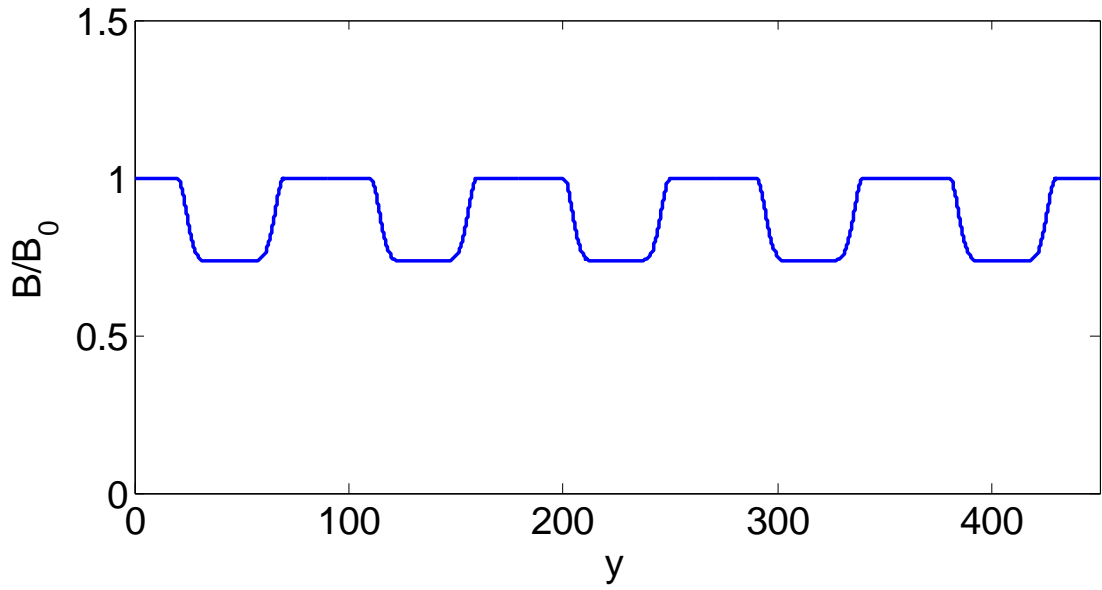


**Figure A.2** Smooth-boundary magnetic field profile

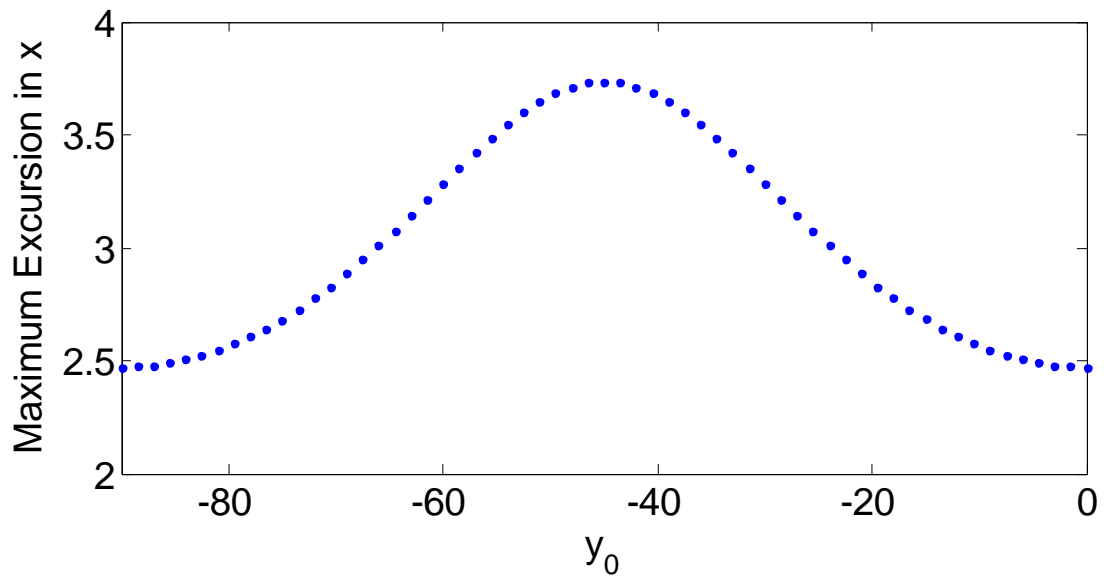


**Figure A.3** Maximum excursion in  $x$  as a function of the initial position  $y_0$  for sinusoidal magnetic field profile.

The maximum excursion in  $x$  as a function of  $y_0$  for the trapezoidal-like magnetic field profile in Figure A.2 is shown in Figure A.4. The overall maximum excursion in  $x$  increases from the sinusoidal case, but is still smaller than in the square magnetic field

profile case in Figure 2.3. As the sharpness of the transition between the maximum and the minimum magnetic field increase, the overall maximum excursion in  $x$  increases and eventually becomes the same as the square magnetic field profile case shown in Figure 2.3.

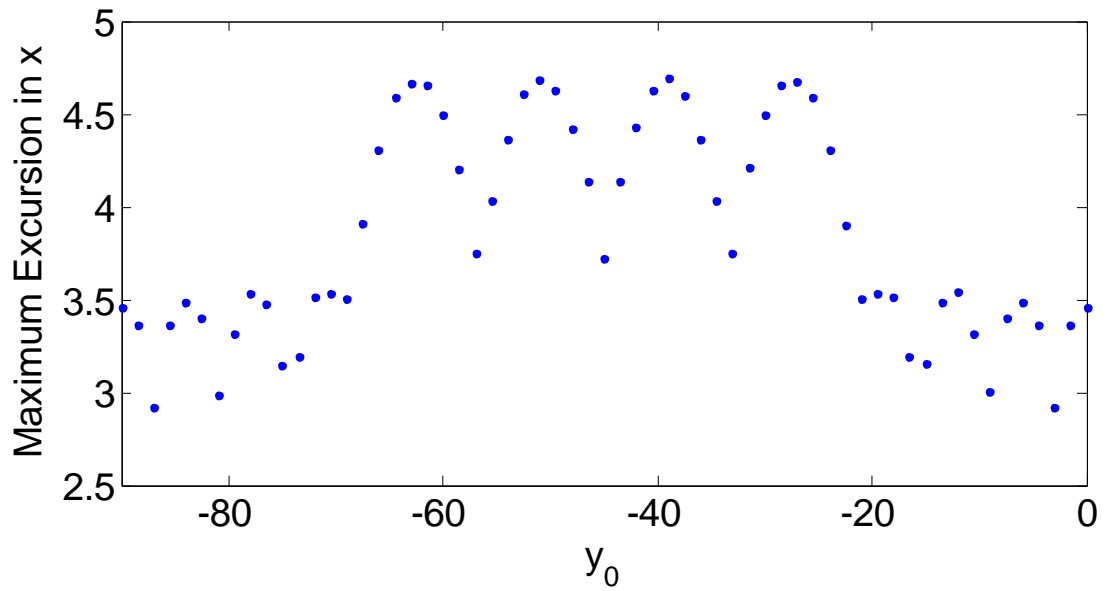
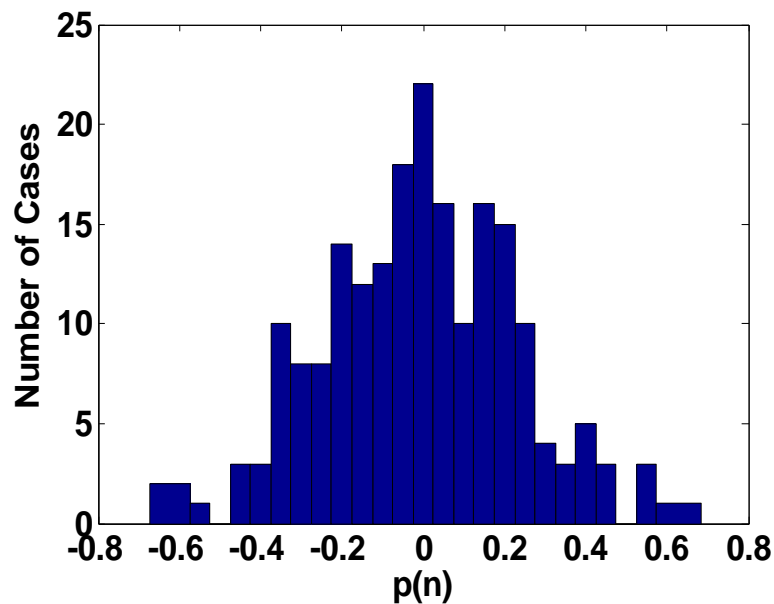


**Figure A.4** Maximum excursion in  $x$  as a function of the initial position  $y_0$  for smooth-boundary magnetic field profile.

## B. GENERATION OF THE RANDOM FUNCTIONS AS AN INPUT TO MANUFACTURING ERROR STUDY

The random profile for the perturbation quantities  $p(x)$ ,  $q(x)$ , and  $r(x)$  given as an example in Figure 5.1 is generated before each calculation. The method for generating  $p(x)$ , as well as  $q(x)$  and  $r(x)$ , is as follows.

For a calculation boundary between  $x = 0$  and  $x = x_{max}$ ,  $(x_{max}-1)$  random numbers corresponding to  $p(1)$ ,  $p(2)$ , ...,  $p(x_{max}-1)$  are initially generated. The generated  $p(n)$  for  $n = 1, 2, \dots, (x_{max}-1)$  are statistically Gaussian with a mean value of 0, and a FWHM that depends on the size of the perturbation. For instance,  $\Delta p = 0.3$  results in  $\text{FWHM} = 0.3 \times 2 = 0.6$ . The figure below shows the distribution of  $p(n)$  for  $x_{max} = 200$  and  $\Delta p = 0.3$ .  $p(0)$  and  $p(x_{max})$  are set to 0. For  $n < x < (n+1)$ ,  $p(x)$  is interpolated between  $p(n)$  and  $p(n+1)$ . Note that the value of  $x_{max}$  used in this case is twice the value used in Chapter 5 in order to emphasize the statistics for larger sample.



## **BIBLIOGRAPHY**

- [Ace07] J. A. Acebrón and R. Spigler, "The remote control and beyond: the legacy of Robert Adler," *Society for Industrial and Applied Mathematics News*, vol. 40, no. 5, Jun. 2007.
- [Adl73] R. Adler, "A study of locking phenomena in oscillators," *Proc. IEEE*, vol. 61, no. 10, pp. 1380-1385, Oct. 1973.
- [Bar01] R. J. Barker and E. Shamiloglu, *High-Power Microwave Sources and Technologies*, New York: IEEE Press/John Wiley & Sons, 2001
- [Bar05] R. J. Barker, J. H. Booske, N. C. Luhmann, and G. S. Nusinovich, *Modern Microwave and Millimeter Wave Power Electronics*, New Jersey: IEEE Press, 2005.
- [Bek76] G. Bekefi and T. Orzechowski, "Giant microwave bursts emitted from a field-emission, relativistic-electron-beam magnetron," *Phys. Rev. Lett.*, vol. 37, p. 379, 1976.
- [Ben87] J. Benford, "Relativistic magnetrons," *High-Power Microwave Sources*, ed. Granatstein V. L. and Alexeff I., Boston: Artech House, 1987, p. 351.
- [Ben89] J. Benford, H. Sze, W. Woo, R. R. Smith, and B. Harteneck, "Phase locking of relativistic magnetrons," *Phys. Rev. Lett.*, vol. 62, no. 8, pp. 969-971, Feb. 1989.
- [Ben92] J. Benford and J. A. Swegle, *High Power Microwave*, Boston: Artech House, 1992
- [Ben07] J. Benford, J. A. Swegle, and E. Schamiloglu, *High Power Microwaves*, 2<sup>nd</sup> Edition, New York: Taylor and Francis, 2007.
- [Bog89] P. Bogacki and L. F. Shampine, "A 3(2) pair of Runge-Kutta formulas," *Appl. Math. Lett.*, vol. 2, no. 4, pp. 321-325, 1989.
- [Boo76] H. A. H. Boot and J. T. Randall, "Historical notes on the cavity magnetron," *IEEE Trans. Electron Devices*, vol. 23, no. 7, p. 724, 1976.
- [Boo02] J. H. Booske, W. J. Lee, S. Gallagher, D. van der Weide, S. Limbach, K. Jain, and C. L. Kory, "Microfabricated TWTs as high power, wideband sources of THz radiation," retrived in 2006 from [http://www.engr.wisc.edu/ece/faculty/booske\\_john/THzmVEDTWTpaper.pdf](http://www.engr.wisc.edu/ece/faculty/booske_john/THzmVEDTWTpaper.pdf)
- [Boo05] J. H. Booske, D. R. Whaley, W. L. Menninger, R. S. Hollister, and C. M. Armstrong, "Traveling-wave tubes," in Ch. 4 of [Bar05], p. 171.
- [Boo07] J. H. Booske, "Plasma physics challenges of mm-to-THz and high power microwave generation," *Plenary Review Paper, American Physical Society, Plasma Physics Division Annual Meeting* (Orlando, FL; November 14, 2007).

- [Bro88] W. C. Brown, *A Reporting of Personal Observations of Noise in Magnetrons and CFAs*, MA: Raytheon, 1988.
- [Bro95a] W. C. Brown, "The history of the reentrant beam crossed field amplifier with emphasis on noise comparison with the magnetron," in *Proc. 1st Int. Workshop Crossed-Field Devices*, D. Chernin and Y. Y. Lau, Eds., Ann Arbor, MI, p. 9, 1995.
- [Bro95b] W. C. Brown, "The high signal to noise ratio of the microwave oven magnetron and evidence of a negative feedback loop to control it," in *Proc. 1st Int. Workshop Crossed-Field Devices*, D. Chernin and Y. Y. Lau, Eds., Ann Arbor, MI, p. 178, 1995.
- [Che84] F. F. Chen, *Introduction to plasma physics and controlled fusion*, 2nd edition, New York, NY: Plenum Press, 1984.
- [Che90a] S. C. Chen, "Growth and frequency pushing effects in relativistic magnetron phase-locking," *IEEE Trans. Plas. Sci.*, vol. 18, no. 3, pp. 570-576, Jun. 1990.
- [Che90b] S. C. Chen, G. Bekefi, and R. Temkin, "Operation of a long-pulse relativistic magnetron in a phase-locking system," *Proc. SPIE*, vol. 1226, pp. 36-43 (1990).
- [Che91] C. Chen, H. W. Chan, and R. C. Davidson, "Parametric simulation studies and injection phase locking of relativistic magnetrons," *Proc. SPIE*, vol. 1407, pp. 105-112, 1991.
- [Che96] D. P. Chernin, "Computer simulation of low noise states in a high-power crossed-field amplifier," *IEEE Trans. Electron Devices*, vol. 43, no. 11, p. 2004, Nov. 1996.
- [Che07] D. P. Chernin and Y. Y. Lau, unpublished (2007). This is a newly developed analytical theory which, together with Chapter 5 of this thesis, is to be published in the *IEEE Trans. Electron Devices*. P. Pengvanich, D. P. Chernin, Y. Y. Lau, J. W. Luginsland, and R. M. Gilgenbach, "Effect of random circuit fabrication errors on small signal gain and phase in traveling wave tubes".
- [Chr96] P. J. Christenson, D. Chernin, A. Garner, and Y. Y. Lau, "Resistive destabilization of cycloidal electron flow and universality of (near-) Brillouin flow in a crossed-field gap," *Phys. Plasmas*, vol. 3, p. 4455, 1996.
- [Col48] G.B. Collins, *Microwave Magnetron*, New York: McGraw Hill, 1948.
- [Dag02] S. D'Agostino and C. Paoloni, "A Study on Helix Pitch Tolerance Impact on TWT Small-Signal Gain," *IEEE Electron Device Lett.*, vol. 23, pp. 746-748, 2002.

- [Dia97] D. Dialetis and D. Chernin, "Effect of random manufacturing errors on slow wave circuit performance," *IEEE Conference Record - 1997 IEEE International Conference on Plasma Science*, 1997.
- [Dom95] G. E. Dombrowski, "Recent advances in simulation of magnetrons and crossed-field amplifiers," in *Proc. 1st Int. Workshop Crossed-Field Devices*, D. Chernin and Y. Y. Lau, Eds., Ann Arbor, MI, p. 236, 1995.
- [Dor80] J. R. Dormand and P. J. Prince, "A family of embedded Runge-Kutta formulae," *J. Comp. Appl. Math.*, vol. 6, no. 1, pp. 19-26, Mar. 1980.
- [Fle06] J. T. Fleming, P. Mardahl, and L. Bowers, "Three dimensional PIC simulations on the transparent and eggbeater cathodes in the University of Michigan relativistic magnetron," *IEEE Conference Record - 2006 IEEE International Conference on Plasma Science*, 2006.
- [Fuk05] M. Fuks and E. Schamiloglu, "Rapid start of oscillations in a magnetron with a "transparent" cathode," *Phys. Rev. Lett.*, vol. 95, no. 20, p. 205101, 2005.
- [Gew65] J. W. Gewartowski and H. A. Watson, *Principles of Electron Tubes*, New Jersey: D. Van Nostrand Company, Inc., p. 362, 1965.
- [Gil86] A. S. Gilmore, Jr., *Microwave Tubes*, Norwood, MA: Artech House, 1986
- [Gil05] R. M. Gilgenbach, Y. Y. Lau, H. McDowell, K. L. Cartwright, and T. A. Spencer, in *Modern Microwave and Millimeter Wave Power Electronics*, R. J. Barker, J. H. Booske, N. C. Luhmann, and G. S. Nusinovich, Eds., Ch. 6, p. 289, Piscataway, NJ: IEEE Press, 2005.
- [Gil94] A. S. Gilmour, Jr., *Principles of Traveling Wave Tubes*, Boston: Artech House, 1994.
- [Gra87] V. L. Granatstein and I. Alexeff, *High-Power Microwave Sources*. Norwood, MA: Artech House, 1987.
- [Ha98] H.-J. Ha, S.-S. Jung, and G.-S. Park, "Theoretical study for folded waveguide traveling wave tube," *International Journal of Infrared and Millimeter Waves*, vol. 19, no. 9, p. 1229, 1998.
- [Hil95] S. Hillenberg, D. Thelen, and A. MacMullen, "Low noise CFA measurements, analysis and simulation," in *Proc. 1st Int. Workshop Crossed-Field Devices*, D. Chernin and Y. Y. Lau, Eds., Ann Arbor, MI, p. 51, 1995.

- [Hof07] B. W. Hoff, R. M. Gilgenbach, Y. Y. Lau, N. M. Jordan, W. White, J. C. Zier, M. R. Gomez, E. J. Cruz, K. L. Cartwright, P. J. Mardahl, T. P. Fleming, M. D. Haworth, T. A. Spencer, and D. Price, "Magnetic priming of a relativistic magnetron utilizing ferromagnetic wires in the cathode and anode," *IEEE Conference Record - 2007 IEEE Pulsed Power and Plasma Science Conference, 2007*; also, *IEEE Trans. Plasma Sci.* (to be published, 2008).
- [Joh90] G. L. Johnston, S. C. Chen, G. Bekefi, and R. C. Davidson, "Models of driven relativistic magnetrons with nonlinear frequency-shift and growth-saturation effects," *Proc. SPIE*, vol. 1226, pp. 108-116, 1990.
- [Jon04a] M. C. Jones, V. B. Naculaes, W. White, Y. Y. Lau, and R. M. Gilgenbach, "Simulation of rapid startup in microwave magnetrons with azimuthally-varying axial magnetic fields," *Appl. Phys. Lett.*, vol. 84, 1016, 2004.
- [Jon04b] M. C. Jones, V. B. Naculaes, R. M. Gilgenbach, W. White, M. Lopez, Y. Y. Lau, T. A. Spencer, and D. Price, "Projection ablation lithography cathode for high power relativistic magnetron," *Rev. Sci. Instrum.*, vol. 75, pp. 2976-2980, 2004.
- [Jon04c] M. C. Jones, V. B. Naculaes, Y. Y. Lau, R. M. Gilgenbach, and W. White, "Cathode priming of relativistic magnetron," *Appl. Phys. Lett.*, vol. 85, pp. 6332-6334, 2004.
- [Jon05a] M. C. Jones, V. B. Naculaes, W. White, Y. Y. Lau, R. M. Gilgenbach, J. W. Luginsland, P. Pengvanich, N. M. Jordan, Y. Hidaka, and H. Bosman, "Simulation of magnetic priming in a relativistic magnetron," *IEEE Trans. Electron Devices*, vol. 52, p. 858, 2005.
- [Jon05b] M. C. Jones, V. B. Naculaes, Y. Y. Lau, R. M. Gilgenbach, W. M. White, B. W. Hoff, and N. M. Jordan, "Magnetron priming by multiple cathodes," *Appl. Phys. Lett.*, vol. 87, p. 081501, 2005.
- [Jon05c] M. C. Jones, "Cathode priming of a relativistic magnetron using multi-emission zones on projection lithography cathodes," Ph.D. Dissertation, Department of Nuclear Engineering and Radiological Sciences, University of Michigan, Ann Arbor, MI, 2005.
- [Kim05] J. I. Kim, J. H. Won, and G. S. Park, "Electron prebunching in microwave magnetron by electric priming using anode shape modification," *Appl. Phys. Lett.*, vol. 86, p. 171501, 2005.
- [Kim06] J. I. Kim, J. H. Won, G. S. Park, H. J. Ha, and J. C. Shon, "Reduction of noise in strapped magnetron by electric priming using anode shape modification," *Appl. Phys. Lett.*, vol. 88, p. 221501, 2006.
- [Kom47] R. Kompfner, "The traveling wave tube as an amplifier at microwaves," *Proc. IRE*, vol. 35, pp. 124-127, February 1947.

- [Kor98] C.L. Kory and J.A. Dayton, Jr., "Effect of helical slow-wave circuit variations on TWT cold-test characteristics," *IEEE Trans. Electron Devices*, vol. 45, pp. 972-976, 1998.
- [Lau87] Y. Y. Lau, "Theory of crossed-field devices and a comparative study of other radiation sources," in *High-Power Microwave Sources*, V. L. Granatstein and I. Alexeff, Eds., Norwood, MA: Artech House, Inc., Ch. 9, p. 309, 1987.
- [Lau95] Y. Y. Lau, "Crossed-field research in universities," in *Proc. 1st Int. Workshop Crossed-Field Devices*, D. Chernin and Y. Y. Lau, Eds., Ann Arbor, MI, p. 337, 1995.
- [Lau03] Y. Y. Lau (unpublished), 2003.
- [Lem99] R. W. Lemke, T. C. Genoni, and T. A. Spenser, "Three-dimensional particle-in-cell simulation study of a relativistic magnetron," *Phys. Plasmas*, vol. 6, p. 603, 1999.
- [Lem00] R. W. Lemke, T. C. Genoni, and T. A. Spenser, "Effects that limit efficiency in relativistic magnetrons," *IEEE Trans. Plasma Sci.*, vol. 28, no. 3, pp. 887-897, Jun. 2000.
- [Lev90] J. S. Levine, J. Benford, B. Harteneck, and S. Montalvo, "Initial operation of a compact phase-locked module of relativistic magnetrons," *Proc. SPIE*, vol. 1226, pp. 44-49, 1990.
- [Lev91] J. S. Levine, N. Aiello, J. Benford, and B. Harteneck, "Design and operation of a module of phase-locked relativistic magnetrons," *J. Appl. Phys.*, vol. 70, no. 5, pp. 2838-2848, 1991.
- [Lop02] M. R. Lopez, R. M. Gilgenbach, D. W. Jordan, S. Anderson, M. D. Johnston, M. W. Keyser, H. Miyake, C. W. Peters, M. C. Jones, V. B. Neculaes, Y. Y. Lau, T. A. Spenser, J. W. Luginsland, M. Haworth, R. W. Lemke, and D. Price, "Cathode effects on a relativistic magnetron driven by a microsecond e-beam accelerator," *IEEE Trans. Plasma Sci.*, vol. 30, no. 3, pp. 947-955, Jun. 2002.
- [Lug04] J. W. Luginsland, Y. Y. Lau, V. B. Neculaes, R. M. Gilgenbach, M. C. Jones, M. H. Frese, and J. J. Watrous, "Three-dimensional particle-in-cell simulations of rapid start-up in strapped oven magnetrons due to variations in insulating magnetic field," *Appl. Phys. Lett.*, vol. 84, p. 5425, 2004.
- [Luh05] N. C. Luhmann, Jr., G. Caryotakis, G. S. Park, R. M. Philips, and G. P. Scheitrum, "Affordable manufacturing," in Ch. 14 of [Bar05], p. 731.

- [Mac94] R. MacGregor, C. Chan, J. Ye, and T. Ruden, "A circular crossed-field amplifier for in situ measurements, study of reentrant beam effects, and comparison with numerical simulation," *IEEE Trans. Electron Devices*, vol. 41, no. 8, pp. 1456-1464, Aug. 1994.
- [Mat94] MATLAB<sup>®</sup>, ©1994-2007, The MathWorks, Inc.
- [Mcd04] H. L. McDowell, "Magnetron simulations using a multiple wavelength computer code," *IEEE Trans. Plasma Sci.*, vol. 30, no. 3, p. 1160, Jun. 2004.
- [Nec03a] V. B. Neculaes, R. M. Gilgenbach, and Y. Y. Lau, "Low-noise microwave magnetrons by azimuthally varying axial magnetic field," *Appl. Phys. Lett.*, vol. 83, p. 1938, 2003.
- [Nec03b] V. B. Neculaes (unpublished), 2003.
- [Nec03c] V. B. Neculaes, R. M. Gilgenbach, M. Lopez, Y. Y. Lau, M. Jones, W. White, P. Pengvanich, M. D. Johnston, T. Strickler, T. A. Spencer, J. Luginsland, M. Haworth, K. Cartwright, P. Mardahl, T. Murphy, D. Price, "Mode competition in relativistic magnetron and injection locking in KW magnetrons," in *AIP Conf. Proc.*, vol. 691, p. 301, 2003.
- [Nec04] V. B. Neculaes, R. M. Gilgenbach, Y. Y. Lau, M. C. Jones, and W. White, "Low-noise microwave oven magnetrons with fast start-oscillation by azimuthally varying axial magnetic fields," *IEEE Trans. Plasma Sci.*, vol. 32, no. 3, pp. 1152-1159, Jun. 2004.
- [Nec05a] V. B. Neculaes, M. C. Jones, R. M. Gilgenbach, Y. Y. Lau, J. W. Luginsland, B. W. Hoff, W. M. White, N. M. Jordan, P. Pengvanich, Y. Hidaka, and H. L. Bosman, "Magnetic perturbation effects on noise and startup in DC-operating oven magnetrons," *IEEE Trans. Electron Devices*, vol. 52, no. 5, pp. 864-871, 2005.
- [Nec05b] V. B. Neculaes, "Magnetron magnetic priming for rapid startup and noise reduction," Ph.D. Dissertation, Department of Nuclear Engineering and Radiological Sciences, University of Michigan, Ann Arbor, MI, 2005.
- [Nec05c] V. B. Neculaes, P. Pengvanich, Y. Hidaka, Y. Y. Lau, R. M. Gilgenbach, W. M. White, M. C. Jones, H. L. Bosman, and J. W. Luginsland, "Rapid kinematic bunching and parametric instability in a crossed-field gap with a periodic magnetic field," *IEEE Trans. Plasma Sci.*, vol. 33, no. 2, pp. 654-660, Apr. 2005.
- [Nec05d] V. B. Neculaes, R. M. Gilgenbach, Y. Y. Lau, "Low-noise crossed-field devices such as a microwave magnetron, microwave oven utilizing same and method of converting a noisy magnetron to a low-noise magnetron," U.S. Patent # 6,872,929, March 29, 2005; and U. S. Patent # 6,921,890, July 26, 2005.

- [Ose95a] J. M. Osepchuk, "The cooker magnetron as a standard in crossed-field device research," in *Proc. 1st Int. Workshop Crossed-Field Devices*, D. Chernin and Y. Y. Lau, Eds., Ann Arbor, MI, p. 159, 1995.
- [Ose95b] J. M. Osepchuk, "Recommendations and predictions on the future of crossed-field devices," in *Proc. 1st Int. Workshop Crossed-Field Devices*, D. Chernin and Y. Y. Lau, Eds., Ann Arbor, MI, p. 339, 1995.
- [Ose02] J. M. Osepchuk, "Microwave power applications," *IEEE Trans. Microwave Theory Tech.*, vol. 50, no. 3, pp. 975-985, Mar. 2002.
- [Pal79] A. Palevsky and G. Bekefi, "Microwave emission from pulsed, relativistic e-beam diodes. II. The multiresonator magnetron," *Phys. Fluids*, vol. 22, no. 5, p. 986, 1979.
- [Pal80] A. Palevsky, "Generation of intense microwave radiation by the relativistic e-beam magnetron (experiment and numerical simulation)," Ph.D. dissertation, Department of Physics, Massachusetts Institute of Technology, Cambridge, MA, 1980.
- [Pen05] P. Pengvanich, V. B. Neculaes, Y. Y. Lau, R. M. Gilgenbach, M. C. Jones, W. M. White, and R. D. Kowalczyk, "Modeling and experimental studies of magnetron injection locking," *J. Appl. Phys.*, vol. 98, p. 114903, 2005.
- [Pie47] J. R. Pierce and L. M. Field, "Traveling wave tubes," *Proc. IRE*, vol. 52, pp. 108-111, February 1947.
- [Pie50] J. R. Pierce, *Traveling Wave Tubes*, New Jersey: D. Van Nostrand Company, Inc., 1950.
- [Pie04] E. Pierce, "Illustration of a traveling wave amplifier," retrieved in June 2007 from [http://en.wikipedia.org/wiki/Traveling\\_wave\\_tube](http://en.wikipedia.org/wiki/Traveling_wave_tube).
- [Pik01] A. Pikovsky, M. Rosenblum, and J. Kurths, *Synchronization*, Cambridge: Cambridge University Press, p. 71, 2001.
- [Pol34] Van der Pol, "The nonlinear theory of electric oscillations," *Proc. IRE*, vol. 22, pp. 1051-1086, Sep. 1934.
- [Sal95] J. A. Saloom, "Past, present, and future crossed-field devices: A personal view," in *Proc. 1st Int. Workshop Crossed-Field Devices*, D. Chernin and Y. Y. Lau, Eds., Ann Arbor, MI, p. 1, 1995.
- [Sch05] G. P. Scheitrum, "Microfabricated MVEDs," in Ch. 7 of [Bar05], p. 343.
- [Sla51] J. C. Slater, *Microwave Electronics*, NY: D. Van Nostrand Company, p. 190, 1951.

- [Sze92] H. Sze, R. R. Smith, J. N. Benford, and B. D. Harteneck, "Phase-locking of strongly coupled relativistic magnetrons," *IEEE Trans. Electromagn. Compat.*, vol. 34, no. 3, pp. 235-241, Aug. 1992.
- [Ums05] R. J. Umstattd, C. G. Carr, C. L. Frenzen, J. W. Luginsland, and Y. Y. Lau, "A simple physical derivation of Child-Langmuir space-charge-limited emission using vacuum capacitance," *Am. J. Phys.*, vol. 73, pp. 160-163, 2005.
- [Vau73] J. R. M. Vaughan, "A model for calculation of magnetron performance," *IEEE Trans. Electron Devices*, vol. 20, p. 818, 1973.
- [Wel53] H. W. Welch, "Prediction of traveling wave magnetron frequency characteristics," *Proc. IRE*, vol. 41, no. 11, Nov. 1953.
- [Wal89] J. E. Walsh, G. L. Johnston, R. C. Davidson, and D. J. Sullivan, "Theory of phase-locked regenerative oscillators with nonlinear frequency-shift effects," *Proc. SPIE*, vol. 1061, pp. 161-169, 1989.
- [Whi05] W. M. White, "RF priming of a long pulse relativistic magnetron," Ph.D. Dissertation, Department of Nuclear Engineering and Radiological Sciences, University of Michigan, Ann Arbor, MI, 2005.
- [Whi06] W. M. White, R. M. Gilgenbach, M. C. Jones, V. B. Neculaes, Y. Y. Lau, P. Pengvanich, N. M. Jordan, B. W. Hoff, R. Edgar, T. A. Spencer, and D. Price, "Radio frequency priming of a long-pulse relativistic magnetron," *IEEE Trans. Plasma Sci.*, vol. 34, no. 3, pp. 627-634, 2006.
- [Wil07] J. D. Wilson and C. T. Chevalier, "Robust optimization of high-frequency traveling-wave tube slow-wave circuit," *IEEE Trans. Electron Devices*, vol. 54, no. 5, p. 1232, May 2007.
- [Woo89] W. Woo, J. Benford, D. Fittinghoff, B. Harteneck, D. Price, R. Smith, and H. Sze, "Phase locking of high-power microwave oscillators," *J. Appl. Phys.*, vol. 65, no. 2, pp. 861-866, 1989.
- [Yam87] K. Yamamoto, H. Kuronuma, T. Koinuma and N. Tashiro, "A study of magnetron noise," *IEEE Trans. Electron Device*, vol. ED-34, p. 1223, 1987.
- [Yor98] R. A. York and T. Itoh, "Injection- and phase-locking techniques for beam control [antenna arrays]," *IEEE Trans. Microwave Theory Tech.*, vol. 46, no. 11, pp. 1920-1929, 1998.